BEWARE OF WARPED SURFACES: NEAR-UNSTABLE CAVITIES FOR FUTURE GRAVITATIONAL WAVE DETECTORS

HAOYU WANG

A thesis submitted to the
University of Birmingham
for the degree of
Doctor of Philosophy

Astrophysics and Space Research Group
School of Physics and Astronomy
College of Engineering and Physical Sciences
University of Birmingham
September 2017

Abstract

The detection of gravitational waves emitted by inspiralling black holes has initiated a new era of astronomy, as the first detection achieved in 2015 marked the start of a new way of observing the universe. The first detection was performed by the Laser Interferometer Gravitational-wave Observatory (LIGO) soon after its first major upgrade. The upgrade applied a variety of advanced techniques such as improved optical systems, vibration isolation systems, monolithic suspensions and higher power lasers to enhance the sensitivity of the interferometer. A couple of similar advanced detectors will soon become operational, forming a network of observatories around the world.

Optical cavities are at the heart of ground-based laser interferometric gravitational wave detectors. These devices are primarily used to enhance the interaction between the laser light and the gravitational waves. A typical advanced detector scheme employs at least six cavities, and the performance of each of them directly impacts on the detector sensitivity. The present thesis focuses on the behaviour of a particular type of Near-Unstable Cavities (NUCs), and their application to the sensitivity enhancement of current and future gravitational wave detectors.

Advanced detectors use high power laser beams. A small fraction of the light energy is absorbed by the cavity mirrors or scattered by the mirror surfaces. The fraction of energy that is absorbed by the mirrors is converted into heat creating thermal effects on the mirror masses and their surroundings. These thermal effects induce thermal lensing and deformations of the mirror structure. Cavities with stable geometrical configurations may be driven into near-unstable, or even unstable regions

due to these thermal perturbations. The operation of near-unstable cavities requires high-precision thermal control of the cavity mirrors, and thus a thermal model of the cavity mirror and its surroundings was built and is presented in this thesis. The model aids the development of mitigation strategies of thermal effects on detector sensitivity. The vibrational mode frequencies of the mirror are used as accurate probes of the overall temperature of the mass. Our simulation results are compared against frequencies that are measured at LIGO. An estimate of the coating absorption coefficient of the mirror is derived from the initial thermal transient. Scattered light is also observed and introduced into the model to accurately account for the thermal status of the mirror surroundings. This model helps to explain the long term thermal behaviour of the cavity mirrors and their surroundings, on the scale of tens of hours after 'lock' is acquired.

Near-unstable cavities have been proposed as an enabling technology for future gravitational wave detectors, as their compact structure and large beam spot can reduce the thermal noise floor of the interferometer. These cavities operate close to the edge of geometrical stability, and may be driven into instability via small cavity length perturbations or mirror surface distortions. They are at risk of suffering from problems such as high optical loss and Gaussian mode degeneracy. The well-defined Gaussian beams can also be distorted through their interaction with the small imperfections of the mirror surfaces. These issues have an adverse impact on the detector sensitivity and controllability. Throughout my Ph.D., I designed and built an experiment to investigate the technical hurdles associated with near-unstable cavities. A near-unstable table-top cavity was built and accurate control achieved through length and alignment control systems. This experiment provides a detailed account of the behaviour of the near-unstable cavity and of the difficulties that need to be overcome in order to achieve optimal operation. Additionally, the experiment provides an insight into how far cavity parameters can be pushed towards geometrical instability. The work I carried out will aid the design of future ground-based gravitational wave detectors.

Acknowledgements

I feel very grateful that everyone I met during my Ph.D. is very nice. There are too many people that helped me. I'm afraid I can't express all my gratitudes here with limited and poor words.

My deepest gratitude goes to my supervisor Prof. Andreas Freise, who introduced me into the gravitational wave community. This thesis would not have been possible without his continuous support. I am grateful for his strong encouragement and directions on how to lead a project and become an expert. I would like to thank him for sending me to several conferences as well as to the LIGO Livingston Observatory for a three-month project.

I would also like to show my sincere gratitude to my second supervisor Dr Conor Mow-Lowry, who joined in Birmingham in early 2015. He gave me important help on the experimental work I carried out through out my Ph.D. and teach me how to be an experimentalist. I would like to thank him for a lot of times working with me in the lab and making the experimental work fun.

I am greatly thankful to Chris Collins and Miguel Dovale Álvarez who worked with me and gave me suggestions for my experimental work. They especially gave me a favour on correcting my thesis, including language problems and the writing style. I am indebted to many of my colleagues in Birmingham to support me. It is a wonderful time working, discussing research problems and having friendship with them: Mengyao Wang, Charlotte Bond, Daniel Brown, Anna Green, Daniel Toyra, Sam Cooper, Aaron Jones and Haixing Miao. I am also grateful to our technical

engineers David Hoyland and John Bryant who helped me build electronics and software.

I would like to give a special mention to Brian O'Reilly, my mentor when I was in the LIGO Livingston Observatory, for his nice and patient guide. I'd also like to thank Carl Blair, the person worked together with me and gave me a lot of help there. Many other thanks go to the LIGO Livingston Observatory staff for their additional support.

At last, my sincere thanks go to my Mum and Dad, who are always there to help and support me. A special thanks to my wife for her encouragement and persist trust.

Statement of Originality

This thesis reports the work I carried out during my Ph.D. in the University of Birmingham between September 2013 and September 2017.

The work introduced in Chapter 2 of the thermal modelling of test masses was carried out by myself and Carl Blair. It has been published in *H Wang, C Blair, M Dovale Álvarez, A Brooks, M F Kasprzack, J Ramette, P M Meyers, S Kaufer, B O'Reilly, C M Mow-Lowry and A Freise. Thermal modelling of Advanced LIGO test masses. Classical and Quantum Gravity, 34(11):115001, 2017* [1].

The tabletop experiment presented in Chapter 4 was designed and set up by myself. Results of the behaviour of near-unstable cavities shown in Chapter 5 have been summarised into a paper and will be submitted for publication.

Contents

Abstract i

Acknowledgements iii

Statement of Originality v

Table of Contents x

1 Introduction 1

1.1 Gravitational waves . . . 2

1.2 Laser interferometric gravitational wave detectors . . . 3

1.3 Principle of interferometric detectors . . . 4

1.4 Noise sources for Advanced detectors . . . 7

1.5 Reducing Coating thermal noise . . . 10

1.6 Stability of Fabry-Perot cavities . . . 13

1.7 Thermal issues and influences on stability . . . 15

1.8 Problems of near-unstable cavities . . . 17

1.9 Thesis overview . . . 18

2 Thermal modelling of test masses 21

2.1 Brief introduction . . . 21

2.2 Using acoustic modes as temperature probes . . . 24

2.3 Heat transfer model of Advanced LIGO test masses . . . 26

2.3.1 Thermal couplings . . . 26

2.3.2 Ambient temperature effect . . . 27
2.4 Finite element model . . . 28
2.4.1 2D-axisymmetric model . . . 29
2.4.2 A simple model . . . 31
2.4.3 The improved model . . . 34
2.5 Creating an accurate long time-scale model . . . 35
2.5.1 Coating absorption measurement . . . 35
2.5.2 Scattered Light . . . 37
2.5.3 Long-term simulation . . . 37
2.6 Testing the model . . . 39
2.7 Conclusion . . . 41

3 Near-unstable cavities 43
3.1 Application for gravitational wave detectors . . . 44
3.2 Configurations . . . 45
3.2.1 Recycling cavity in Advanced Virgo . . . 45
3.2.2 Arm cavity for future detectors . . . 47
3.3 Mode behaviours . . . 50
3.3.1 Gaussian modes . . . 50
3.3.2 Gouy phase . . . 51
3.3.3 Modes bunching . . . 53
3.3.4 Mode separation factor . . . 57
3.4 Angular instabilities . . . 59
3.5 Conclusion . . . 59

4 Setup and characterisation of the near-unstable cavity 61
4.1 Optical design of the setup . . . 62
4.1.1 Configuration: a plane-concave cavity . . . 62
4.1.2 The cavity design . . . 67
4.1.3 Layout of the setup . . . 68
4.1.4 Mode matching of the cavity . . . 69

4.2 Length stabilisation of the cavity . . . 73
4.2.1 Optical components for the setup . . . 74
4.2.2 Electronic devices . . . 81
4.2.3 The Control loop . . . 86
4.2.4 Noise performance . . . 101
4.3 Frequency stabilisation of the probe laser . . . 107
4.3.1 Split feedback loop . . . 108
4.3.2 Offset phase lock of the two lasers . . . 110
4.4 Alignment control . . . 113
4.4.1 Misalignments of a hemispherical cavity . . . 114
4.4.2 Influence of misalignments to transverse modes . . . 114
4.4.3 Creating error signal for the alignment system . . . 118
4.4.4 QPD telescope design . . . 121
4.4.5 Closed the loop: automatic alignment system . . . 123
4.5 Conclusion . . . 125

5 Exploring near-instability **127**
5.1 Measuring mode separation frequency . . . 128
5.2 Higher-order mode splitting . . . 132
5.3 Quantifying the stability . . . 134
5.4 Conclusion . . . 145

6 Summary and future work **147**
6.1 Summary and conclusions . . . 147
6.2 Future work . . . 149

A The AEI 10 m Prototype **151**

B Parameters used in thermal modelling **153**
B.1 Ambient temperature calibration . . . 153
B.2 Geometric parameters of the model . . . 155
B.3 Start time and duration of each lock . . . 155

B.4 Arm power of each lock 156
B.5 Uncertainties of ring heater emissivity 157

C Pound-Drever-Hall stabilisation technique **159**

Bibliography **177**

List of Figures

1.1 A picture depicting the distortion effect by gravitational waves in space-time. 2
1.2 Configurations of Michelson gravitational wave interferometers. 5
1.3 Configuration of a dual recycling Michelson interferometer. 7
1.4 Noise budget for broadband, high power laser beam mode of Advanced LIGO. 9
1.5 The stability diagram of a Fabry-Perot cavity. 14

2.1 Frequency shift and ambient temperature fluctuations during a 36 hour lock in LIGO Livingston detectors. 25
2.2 A heat transfer model between an end test mass, a reaction mass, a ring heater, the ambient isotherm, and an extra term. 26
2.3 Inputs, outputs, and free parameters of the finite-element model. . . . 28
2.4 Surface distortions of the 15539 Hz mechanical mode and 15234 Hz mode. 29
2.5 The frequency behaviour of different modes using 3D or 2D-axisymmetric models with different mesh size. 30
2.6 3D view of the geometry of the ETM, ring heater, reaction mass, and extra term as modelled in COMSOL. 31
2.7 The thermal transient of the ETM with different surrounding included during 30 hours' lock with 1ppm coating absorption. 34
2.8 Mode frequency shift data from the first 3 hours after lock. 36
2.9 Ring heater temperature data from the first 3 hours after lock. 37

2.10 Long-term comparison of the April data with both models. 38
2.11 Testing the tuned model with the December lock data. 40

3.1 The configuration of the concave-convex power recycling cavity for Advanced Virgo. 46
3.2 Two possible choices of NUCs to provide a large beam size with a compact design. 47
3.3 The change of parameters of a certain Guassian beam mode matched to the cavity when g_c varies from 0 to 1 by increasing cavity length. . 50
3.4 One-way Gouy phase difference in NUCs. 52
3.5 The intensity of light transmitted from the cavity when tuning the microscopic position of one cavity mirror. 54
3.6 A figure depicting changed in resonance separations of Gaussian modes in a cavity as the cavity stability is varied. 56
3.7 The separation factor as a function of total g-factor with different cavity finesse values in current interferometers. 58

4.1 Comparison of a plane-concave cavity and a symmetric near-concentric cavity. 63
4.2 The Gaussian beam in a stable cavity. 64
4.3 Simulated differences in free spectral range and modes bunching between the near-concentric cavity and the plane-concave cavity. 66
4.4 The schematic layout of the Birmingham 1 m NUC experiment setup. 69
4.5 Lens group positions for $g_c = 0.001$. 71
4.6 Lens group positions for $g_c = 0.00004$. 71
4.7 A schematic showing how waist size mismatch couples the fundamental mode to the second order mode. 72
4.8 The frequency noise of the Mephisto laser. 76
4.9 A schematic picture online showing the principle of a Faraday Isolator. 78
4.10 A schematic plot of the Model 4004 phase modulator from the Newport Corporation. 80

4.11 The schematic of the photodetector for the Pound-Drever-Hall stabilisation. . . . 82
4.12 Measured transfer functions of our servos. . . . 85
4.13 The two signals sent to the servo for lock acquisition. . . . 88
4.14 A Pound-Drever-Hall loop including all relevant optical and electrical components. . . . 90
4.15 Transfer function of the high-voltage amplifier and the laser PZT. . . . 93
4.16 Electronic devices in a Pound-Drever-Hall loop. . . . 93
4.17 An external low-pass filter is introduced into the loop to bring down the pole frequency to 10 Hz. . . . 94
4.18 The measured transfer functions of components in the Pound-Drever-Hall loop. . . . 95
4.19 A method to measure the open loop transfer function in a closed loop. 96
4.20 Oscillations that cause the loop to become unstable. . . . 98
4.21 A loop used for calibration of the laser PZT. . . . 99
4.22 The measured and fitted error signals of the mode cleaner. . . . 100
4.23 The measured gain of the laser PZT. . . . 101
4.24 The measured transfer function of the 1 m cavity. . . . 102
4.25 The measured electronic noise of each device used in the Pound-Drever-Hall loop. . . . 103
4.26 A part of the electrical loop of the Pound-Drever-Hall setup. . . . 104
4.27 Configuration of an amplifier with a tunable gain. . . . 105
4.28 The residual noise and the free running noise of the system. . . . 106
4.29 The split feedback loop used to stabilise the frequency of the probe laser. . . . 109
4.30 The residue noise between the probe laser and the cavity. . . . 110
4.31 The schematic of the offset phase locking system. . . . 111
4.32 Schematic of the principle by which the fundamental mode is coupled to the first order mode by translation of the cavity axis. . . . 116

4.33 Principle by which the fundamental mode couples to the first order mode due to cavity axis tilt. 117
4.34 The telescope for QPD1. 122
4.35 The telescope for QPD2. 123
4.36 Schematic of the auto-alignment system. 124
4.37 Transfer functions measured for actuators and QPDs. 124

5.1 Photo of the tabletop setup. 128
5.2 Photo of the end mirror and components at the transmission port. . . 129
5.3 Resonant frequencies of the first order mode and the second order mode in a near-stable plane-concave cavity. 131
5.4 A plot showing the g-factor or $1 - L$ (supposing $R_c = 1\,\mathrm{m}$) as a function of $\mathrm{MSF}^{02}_{\mathrm{PCC}}$. 132
5.5 A cavity scan measurement showing resonant frequencies of HOMs. . 133
5.6 Resonances measured by scanning the frequency of the probe laser when pushing the cavity to near-unstable region. 136
5.7 Fitting results of measured resonant frequencies for the HG00, HG02 and HG20 modes. 139
5.8 Frequency difference between the HG02 mode and the HG20 mode as a function of cavity g-factor. 140
5.9 Observed resonant mode shapes of the transmitted beam in each cavity length. 141
5.10 The overlap between the fundamental mode (HG00) and the HG02 mode. 142
5.11 Measured error signals when pushing the cavity to the near-unstable region. 144
5.12 The mode separation factor as a function of g-factor of our 1 m plane-concave cavity. 145

A.1 A schematic drawing of the AEI prototype which is based on Michelson interferometer with arm Fabry-Perot cavities. 151

B.1 A picture showing more data for the ambient temperature calibration. 154
B.2 Geometric parameters of the model. 155
B.3 The optical power inside the Y-arm cavity. 156
B.4 The simulation of ring heater temperature with different surface emissivity values in the simple model. 157

C.1 The frequency response of an optical cavity for the reflected beam. . . 160
C.2 A schematic plot of the Pound-Drever-Hall locking technique. 161
C.3 The error signal of the Pound-Drever-Hall locking technique. 164

List of Tables

2.1 Comparison of mode frequencies using different models and mesh sizes. 30

2.2 Material properties. 33

3.1 Cavity g-factors and mode separation factors of current ground based gravitational wave detectors. 58

4.1 Parameters of the plane-concave cavity setup. 68

4.2 Manufacturer specified specifications of the Mephisto lasers. 74

4.3 Specifications of the Model 4004 phase modulator 81

4.4 Specifications of the digital servo used for the Pound-Drever-Hall stabilisation. 84

4.5 Specifications of the SVR 500 high-voltage amplifier. 86

4.6 Tilts of plane-concave cavity mirrors coupled to cavity axis misalignments. 114

4.7 Mode coupling coefficient from the fundamental mode to the first order mode due to cavity axis misalignments. 118

B.1 Start time and duration of each lock of the detector in LIGO, Livingston. 156

Chapter 1

Introduction

Gravitational waves (GW) were first predicted in 1916 by Albert Einstein. In his theory of General Relativity, he indicated that fluctuating gravitational fields would transport energy as gravitational radiation, known as gravitational waves. The effect introduced by gravitational waves is very weak and, as such, detectable gravitational waves only come from very energetic systems such as binary neutron stars and black holes.

A global network of gravitational wave detectors has formed. The first gravitational wave signal ever detected, GW150914 [2], was during the first observation run (O1) of the Advanced Laser Interferometer Gravitational Wave Observatory (LIGO) [3] in which a binary black hole coalescence signal was identified. The second detection, GW151226 [4], was recorded in the same run, followed by a third detection, GW170104 [5], during the second observation run (O2) about one year later.

The detection of gravitational waves is direct confirmation of Einstein's theory of general relativity. In addition, gravitational waves encode information about their sources, which is very useful for astronomy studies. The direct detection of gravitational waves has opened a new window in astrophysical observations.

1.1 Gravitational waves

According to General Relativity, gravitational waves are described as ripples of space-time and propagate at the speed of light. The amplitude of gravitational wave is usually characterised by its strain, derived from Einstein's field equations, given by [6, 7]:

$$h = \frac{2G}{rc^4}\frac{\partial^2 I}{\partial t^2}, \tag{1.1}$$

where G is Newton's gravitational constant, c is the speed of light, r is the distance to the source, I is the mass quadrupole moment of the source and t is the time. A gravitational wave with a strain h will cause space-time distortions, characterised by:

$$h = \frac{\Delta L}{L}, \tag{1.2}$$

where ΔL is the change caused by the gravitational wave in the distance L between two free test masses in space-time. The effect of the gravitational wave to the space-time is usually described by a 'stretch and squash' picture. Figure 1.1 depicts this effect on a ring of masses. Distances between these masses stretch and squash according to the phase of the gravitational wave.

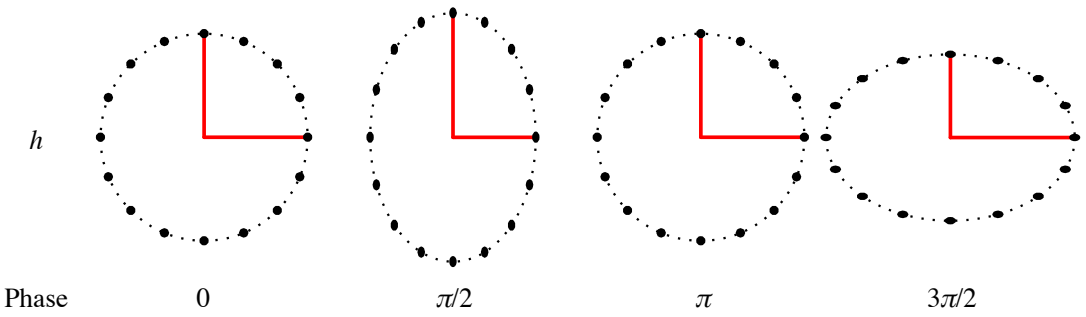

Figure 1.1: A picture depicting the distortion effect by gravitational waves in space-time. Distances between a ring of masses stretch and squash according to the phase of the passing by gravitational wave.

For current gravitational wave detection, a typical wave with the preferable polarisation will cause the distance between two masses along one direction stretches while distance along the orthogonal direction squashes at the same time and vice versa. For gravitational wave detection, the problem is that the estimated strain of

the gravitational wave caused by even the strongest cosmic event is in the scale of $h \sim 10^{-21}$ [7]. Thus, in a 4 km space interval, the associated change is of the order of 10^{-18} m.

1.2 Laser interferometric gravitational wave detectors

At the time of writing, all confirmed observations of gravitational waves have been detected with ground-based laser interferometers, which employ a differential length measurement between free test masses to detect gravitational waves. Previously, resonant bar detectors [8] have been used. For ground-based detectors, the main advantages of interferometers compared to resonant bars is that the separation of test masses is very large and the detection bandwidth is wider.

Several ground-based interferometers have been built over last 30 years with a detection bandwidth from about 10 Hz to 10 kHz. These were the first generation gravitational wave detectors including initial LIGO [9], initial VIRGO [10], GEO600 [11] and TAMA300 [12]. These detectors had similar designs using a Michelson interferometer configuration. Among them, the initial LIGO detectors located in the US with the maximum arm length (the separation distance of test masses) of about 4 km were the most sensitive ones which could reach a maximum sensitivity close to $10^{-23}/\sqrt{\text{Hz}}$. The French-Italian detector VIRGO has a slightly shorter arm length of 3 km. The German-British detector GEO600 is a smaller interferometer with an arm length of 600 m which pioneered many advanced detector techniques. TAMA300 is a Japanese detector with an arm length of 300 m. Whilst all of these detectors reached their design sensitivities, a credible detection could not be determined from the noise.

Now the LIGO detectors have been upgraded to Advanced LIGO [3], a second generation gravitational wave detector. The design sensitivity for Advanced LIGO is a factor of 10 better than initial LIGO. However it hasn't achieved the design

sensitivity yet due to technique problems. Advanced VIRGO [13] has also been upgraded and joined observation in August 2017. GEO600 has demonstrated second generation technology such as monolithic suspensions and signal recycling, and is now testing technologies for enhancing the second generation instruments with a similar sensitivity with Advanced LIGO at frequencies above 1 kHz [14]. TAMA300 has been shut down but a new detector KAGRA (previously called LCGT) [15, 16] is being built in Japan which would pioneer cryogenic techniques to reduce thermal noise. Another LIGO detector will be built in India [17].

The second generation detectors (or the so called *Advanced detectors*) are expected to detect an increasing rate of GW sources in the next few years. At the same time, conceptual designs of third generation detectors have been proposed to provide sufficient sensitivities for further studies of gravitational waves. The Einstein Telescope (ET) project in Europe is especially focused on the observational aspects rather than on the detection capabilities [18, 19, 20]. Also, the Advanced LIGO detectors will hopefully be upgraded to LIGO Voyager [21], further increasing the sensitivity by a factor of about 3.

1.3 Principle of interferometric detectors

The current generation of laser interferometric gravitational wave detectors are based on the Michelson interferometer configuration with two perpendicular arms (see the left image in Figure 1.2). A central beam splitter (BS) divides the beam from the laser into two equal parts. The two beams propagate along the arms and are reflected back towards the beam splitter by mirrors at the ends of the arms. The two reflected beams are recombined at the BS and the resulting interference signal is detected by a photodetector (PD). The two mirrors act as free test masses (TMs) because gravitational waves induce fluctuations in the distances between the BS and the TMs.

Michelson gravitational wave detectors are operated at the *dark fringe*, i.e., the two

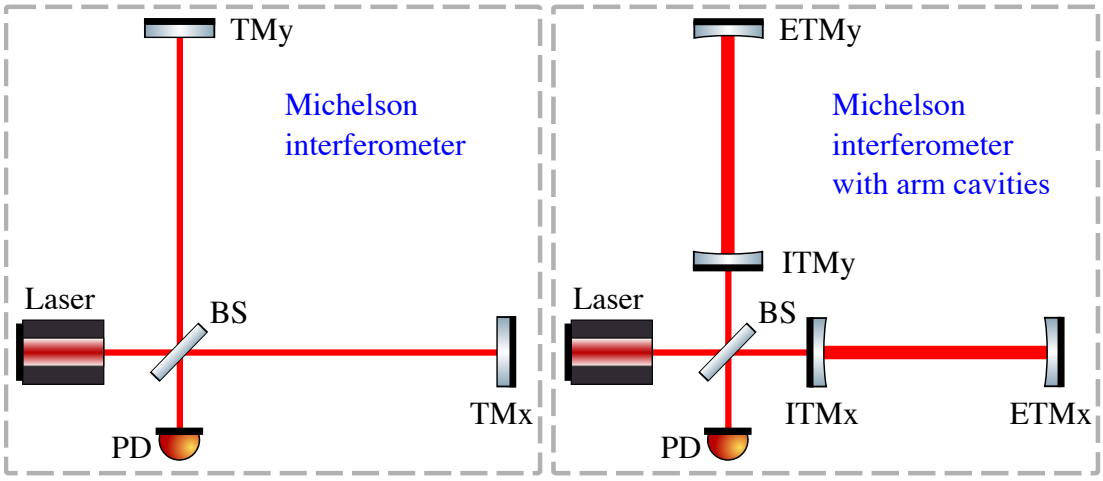

Figure 1.2: Configurations of Michelson gravitational wave interferometers. Left: a simple Michelson interferometer with a test mass at the end of each arm. Right: the Michelson interferometer with Fabry-Perot cavities in its arms, which increase the amount of time each photon spends in an arm and the power in the arms.

beams interfere destructively at the BS, and no light reaches the photo diode unless the relative length of the arms change.

Gravitational waves with optimal polarisation would change the lengths of the two arms by the same magnitude ΔL, but with different signs. Thus, at a certain time, one arm is stretched by ΔL while the other is squashed by ΔL, making up to a $2\Delta L$ difference between two arm lengths. This difference in length induces a relative phase shift between the two beams:

$$\Delta\phi = \frac{2\pi}{\lambda} 2\Delta L. \tag{1.3}$$

This phase shift creates a power change at the photodetector.

Arm cavities

The Michelson configuration introduced above is called a *simple Michelson interferometer*. With a simple Michelson interferometer, the arm lengths should ideally be in the order of $c/(2\pi f_{\mathrm{GW}})$ [22], where f_{GW} is the frequency of the gravitational wave to detect. This means for a frequency of 100 Hz, the required arm length is close

to 500 km, which is impractical for ground-based detectors. Most current ground-based interferometers (except GEO 600) employ Fabry-Perot cavities in their arms, where light is reflected back and forth many times before leaving the cavities. In this configuration (see the right picture in Figure 1.2), each interferometer arm has two mirrors that form a long optical cavity. For Advanced LIGO, the distance between two cavity mirrors is 4 km and for Advanced Virgo it is 3 km. The cavity mirror closer to the beam splitter is usually referred to the input test mass (ITM) and the second cavity mirror is called the end test mass (ETM). The Fabry-Perot cavities increase the light power in the arms by a factor of ~ 300 for Advanced LIGO, which improves the quantum noise (mainly shot noise) limited sensitivity.

Recycling cavities

When the interferometer operates at the dark fringe, nearly all the optical power is reflected back to the laser port. Thus, the Michelson interferometer can be seen as a compound mirror whose reflectivity is close to 1. To further increase the light power in the arms another mirror, called power recycling mirror (PRM), is placed between the laser and the interferometer. The PRM and the ITMs form a cavity called the power recycling cavity (PRC). The PRC is designed and tuned such that almost no light is reflected back towards the laser. In Advanced LIGO, the PRC increases the power incident at the BS by a factor of ~ 40. Figure 1.3 shows the schematic configuration of Advanced LIGO, where the PRM can be seen. Other advanced gravitational wave detectors, such as Advanced Virgo, have similar configurations but slightly different PRC parameters. The light power in the two arm cavities of Advanced LIGO is designed to be ~ 750 kW.

The signal recycling cavity (SRC) is similar to the PRC. A signal recycling mirror (SRM) is placed between the photodetector and the interferometer. The main beam cannot reach the detection port due to the destructive interference at the BS. However, signal sidebands created by gravitational waves can be transmitted from the interferometer to the photodetector. The SRM can be tuned to a mode where the

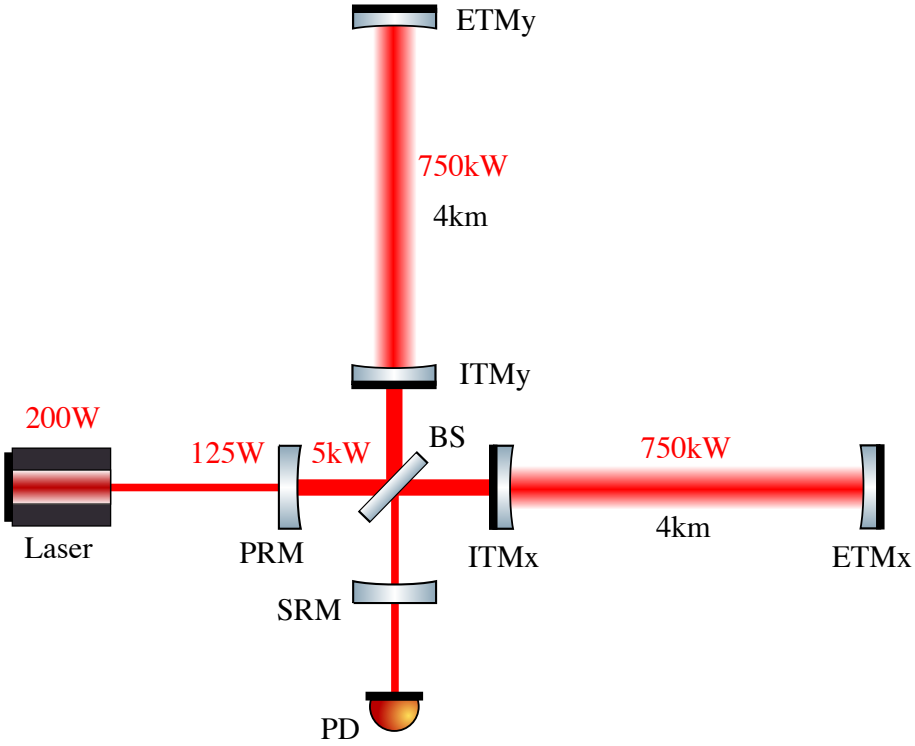

Figure 1.3: Configuration of a dual recycling Michelson interferometer. The powers displayed here are Advanced LIGO design levels.

signal sideband with a particular frequency is resonantly enhanced by the SRC so that the detector is especially sensitive to gravitational waves with this particular frequency. Alternatively, the SRC can be set up to a mode where all signal sidebands are anti-resonant, which widens the detectable frequency band. In the latter case, the detector sacrifices the peak sensitivity to acquire a broader detection bandwidth, a regime called resonant sideband extraction.

1.4 Noise sources for Advanced detectors

There are many noise sources that can induce a phase shift in the interferometer arms that are indistinguishable from gravitational wave signals. For current advanced (second generation) detectors, the main sources of noise are seismic, gravity gradient, quantum and thermal noise.

Noises of the detector are usually described by their amplitude spectral densities.

In order to compare them with the effect of the gravitational wave, they are all calibrated to the unit of the amplitude density of the gravitational wave which is $1/\sqrt{\text{Hz}}$. The amplitude density of the gravitational wave $\bar{h}$ is just the square root of the power spectral density $S_h(f)$:

$$\bar{h} = \sqrt{S_h(f)} \quad [1/\sqrt{\text{Hz}}], \tag{1.4}$$

where $S_h(f)$ gives the mean-square value of h at the frequency f within a bandwidth of 1 Hz [23]. If $\bar{h}$ is constant in a bandwidth of Δf, we have:

$$\bar{h}\sqrt{\Delta f} = h. \tag{1.5}$$

Figure 1.4 gives a noise budget for Advanced LIGO detectors in a bandwidth roughly from 5 Hz to 5 kHz. Seismic, gravity gradients and suspension thermal noise are limiting noises in low frequencies while quantum noise limits the sensitivity across the majority of the detection bandwidth.

Seismic noise and Newtonian noise Seismic noise arises from ground vibrations caused by tectonic motion, human activity, the wind and tides. This causes a differential motion between the two test masses in ground based interferometers. At the same time, changes in the ground mass distribution caused mainly by motion in the ground, changes the Newtonian gravity balance of the suspended test masses, inducing position shifts in the test masses. This coupled noise is called Newtonian noise. As seismic noise is expected to be further reduced in the second generation detectors, Newtonian noise will become more evident. The third generation detectors (such as ET) would be built in an underground location where seismic motion and Newtonian noise are reduced further.

Quantum noise Quantum noise includes two kind of effects: the shot noise and radiation pressure noise, with the former dominant at high frequencies and the

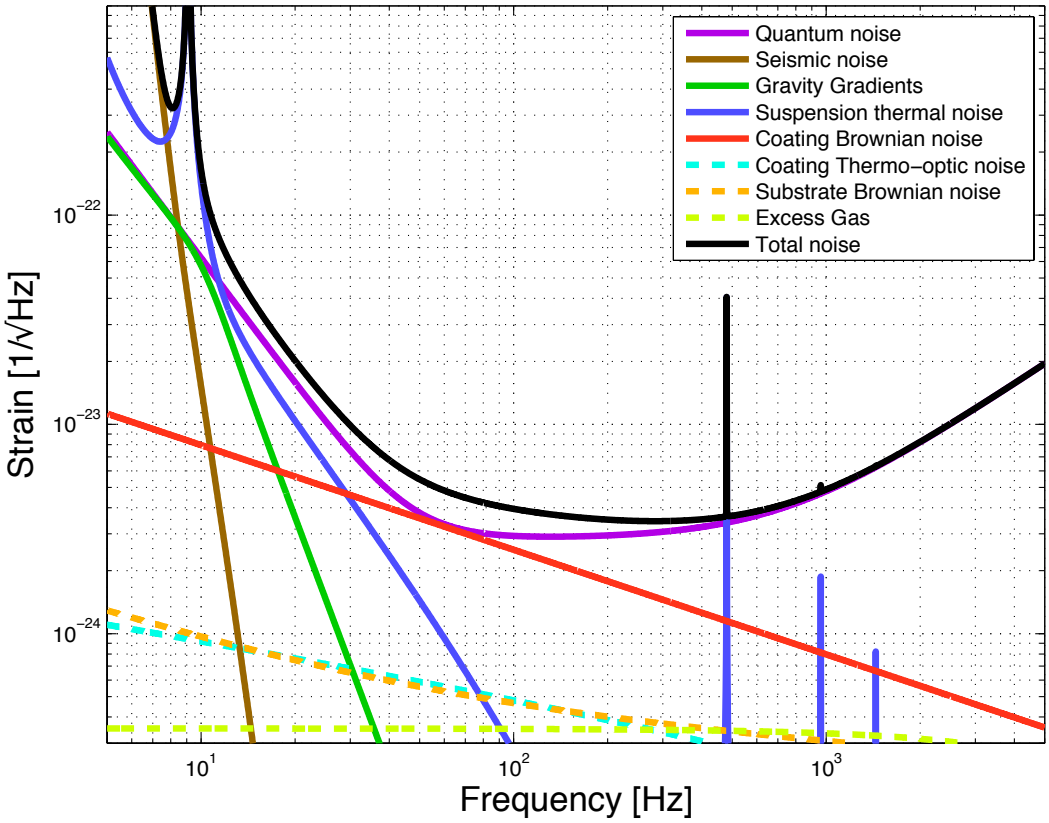

Figure 1.4: Noise budget for broadband, high power laser beam mode of Advanced LIGO. All the noise sources are calculated by GWINC (the Gravitational Wave Interferometer Noise Calculator) which is a collection of Matlab functions that calculates interferometer noise sources and the sensitivity of a design to different astrophysical sources, developed in 1997 by L. S. Finn of the GWAstro Group and originally named Bench [24].

latter at low frequencies respectively. Shot noise is also known as photon counting noise. This randomness corresponds to random fluctuations of the light intensity detected by PDs, thus creating noise in the output signal. Increasing the signal-to-noise ratio requires high light power. On the other hand, large numbers of photons carry momentum that exert random forces on the suspended test masses, causing test mass position changes. Noise induced by this effect is called radiation pressure noise, which is mitigated by reducing light power or increasing mirror mass.

Thermal noise In advanced gravitational wave detectors, thermally excited vibrational modes in suspension wires and the high-reflective coatings of test masses contribute *suspension thermal noise* and *coating thermal noise*, respectively. These effects both change effective arm lengths of the detectors. As quantum noise is expected to be further reduced in the third generation detectors, thermal noise will likely become one of limiting noise sources. The suspension thermal noise is significant at low frequencies between 5 Hz and 50 Hz. The coating thermal noise limits the mid-band sensitivity of the interferometer from 30 Hz to 300 Hz. To reduce thermal noise, high quality materials with low mechanical loss and low operating temperature will be used.

1.5 Reducing Coating thermal noise

Coating thermal noise, or coating Brownian noise, is expected to be the limiting noise source of the next generation detector in the frequency range of roughly 30 Hz to 300 Hz. This corresponds to the most sensitive band of the interferometer. A reduction in coating Brownian noise will increase the interferometer's peak sensitivity.

The thermal noise due to dielectric optical coatings has been studied in [25, 26]. For a very simple case of $Y = Y_c = Y_s$ and $\sigma = \sigma_c = \sigma_s = 0$ where Y and σ are the Young's modulus and the Poisson's ratio respectively (the subscript c and s stand for the coating and the substrate respectively), the coating thermal noise can be estimated using the following formula [25]:

$$S_x(f)_{\text{coating}} = \frac{8k_BT}{3\pi^2 f}\frac{d}{w^2 Y}\left(2\phi_B + \phi_S\right), \tag{1.6}$$

where S_x is the power spectral density of the coating thermal fluctuations seen by the interferometer, k_B is the Boltzmann constant, T is the temperature of the test masses in Kelvin, f is the frequency of the fluctuations, d is the thickness of the coating, w is the laser beam spot radius, ϕ_B and ϕ_S refer to the mechanical loss of the coating material of its bulk and shear modulus respectively.

According to Equation 1.6, we can see the power spectral density for coating Brownian noise is proportional to the temperature of the coating T, the thickness of the coating d and the mechanical loss ϕ, and is inversely proportional to the square of the beam spot size on the coating w. If we could optimise these parameters, the noise level would be reduced. The four intuitive ways of reducing coating Brownian noise are: lowering the temperature of the coating, making the coating layers thinner, reducing mechanical losses of the coating and increasing the laser beam spot size on the coating surface.

Using cryogenic techniques Cooling down the optics to cryogenic temperature is the most direct way of reducing thermal noise. Cryogenics are a crucial component and probably will be used in third generation gravitational wave detectors [18]. The drawbacks of cryogenic optics stem mainly from the fact that it is very difficult to extract heat from the well-isolated test masses, and the mirror suspension systems usually have high thermal resistance. The materials used for mirror substrates and coatings would need to be replaced, as the materials used in current detectors like Advanced LIGO, Advanced Virgo and GEO 600, have high mechanical loss at cryogenic temperatures [27]. The Japanese detector KAGRA is pioneering the use of cryogenic technologies for ground-based interferometers. Technical noises introduced by the cooling system also require careful study and must be reduced to a very low level. There is still a lot of ground to cover before cryogenic systems can be fully integrated in future gravitational wave detectors.

Optimisation of coating thickness For Advanced LIGO, the high-reflective coating of each end test mass (ETM) in the arm cavity is made up of 19 pairs of high and low index alternating layers, allowing only 5 ppm (parts per million) transmission in total [28]. For these extremely high-reflectivity optics, the number of coating layers is a prescribed requirement, making it very difficult to reduce the coating thickness in order to achieve a reduction of coating thermal noise. Some methods provide ways of optimising the coating thickness, but the consequent re-

duction of thermal noise is not significant [29]. Alternative ways of reducing coating thickness have also been proposed, like using wave-guide mirrors [30, 31, 32] and Khalili cavities [33, 34]. Using these techniques turns out to be very challenging and requires further development.

Improve coating properties Some particular treatments such as doping [35, 36] and high-temperature annealing for the coating layers are a powerful means of reducing coating mechanical loss. Mixed material coatings [37, 38] and alternative materials (like amorphous and crystalline) for gravitational wave detectors are being investigated within the international collaboration. An overview of this topic can be found in [21].

Increasing the beam spot size on cavity mirrors

The coating thermal noise can be reduced by increasing the beam spot size, thus spreading the heat over a larger area of the mirror surface.

There has been investigation into increasing the area of the intensity distribution of the beam by using alternative beam shapes. Possible candidates are conical beams [39], mesa beams [40, 41] and the Laguerre-Gauss (LG) 33 beam [42]. As conical and mesa beams require more complex mirror profiles, the LG33 beam produced by standard spherical mirrors is a more promising alternative. Analytical studies show that the coating Brownian noise could be reduced by a factor of 2.65 by using LG33 mode [43, 44]. The problems of LG33 mode mainly comes from its degeneracy [45] because the cavity is also resonant simultaneously for other modes that have the same order. Better manufacturing and characterising techniques for mirror surfaces are required before the LG33 mode can be implemented in future gravitational wave detectors.

In this thesis a great deal of the research effort went into investigating the implications and technical hurdles associated with increasing the geometric beam spot

size on the mirrors in order to reduce the thermal noise floor of future gravitational wave detectors by changing the configuration of the arm cavities. We concentrate on the fundamental Gaussian beam, used in current advanced detectors. Thermally-induced displacement noise due to the optical coatings in Advanced LIGO detectors can be reliably reduced by a factor of 1.6 by increased beam size (from 5.31 cm to 8.46 cm at the ITM and from 6.21 cm to 9.95 cm at the ETM) during the third generation upgrade [21, 27].

In theory, the larger the beam size, the higher the improvement due to the reduction of thermal noise. There are, however, two factors at play limiting the maximum beam size: the available mirror size and the stability of the cavity. The mirror size is usually determined by the available substrate size and maximum coated area. A large beam size without a sufficiently large mirror and coated area will lead to clipping and scattering losses. An empirical ratio of mirror radius to beam radius is 2.5, in which the clipping loss is only a few ppm (parts per million) [46].

The main concern with using large beam sizes lies on the stability of the cavity, which can easily become critical. Using longer arm cavities would certainly help in achieving larger beam sizes whilst maintaining stability, but the cavity length is limited in ground-based detectors. Using large beam sizes thus requires pushing the cavity parameters towards the edge of geometric stability. In such cases, the cavity degeneracy increases significantly, as small cavity length perturbations or mirror imperfections can drive the cavity out of a stable configuration. Problems associated with near-unstable cavities are summarised in Section 1.8.

1.6 Stability of Fabry-Perot cavities

The Fabry-Perot cavity is the simplest optical resonator configuration, consisting of two partially reflective mirrors. The stability of a Fabry-Perot cavity is determined by three parameters: the ROCs of the two mirrors, R_{c1} and R_{c2}, and the mirror separation length, L. Most laser setups, including interferometric gravitational wave

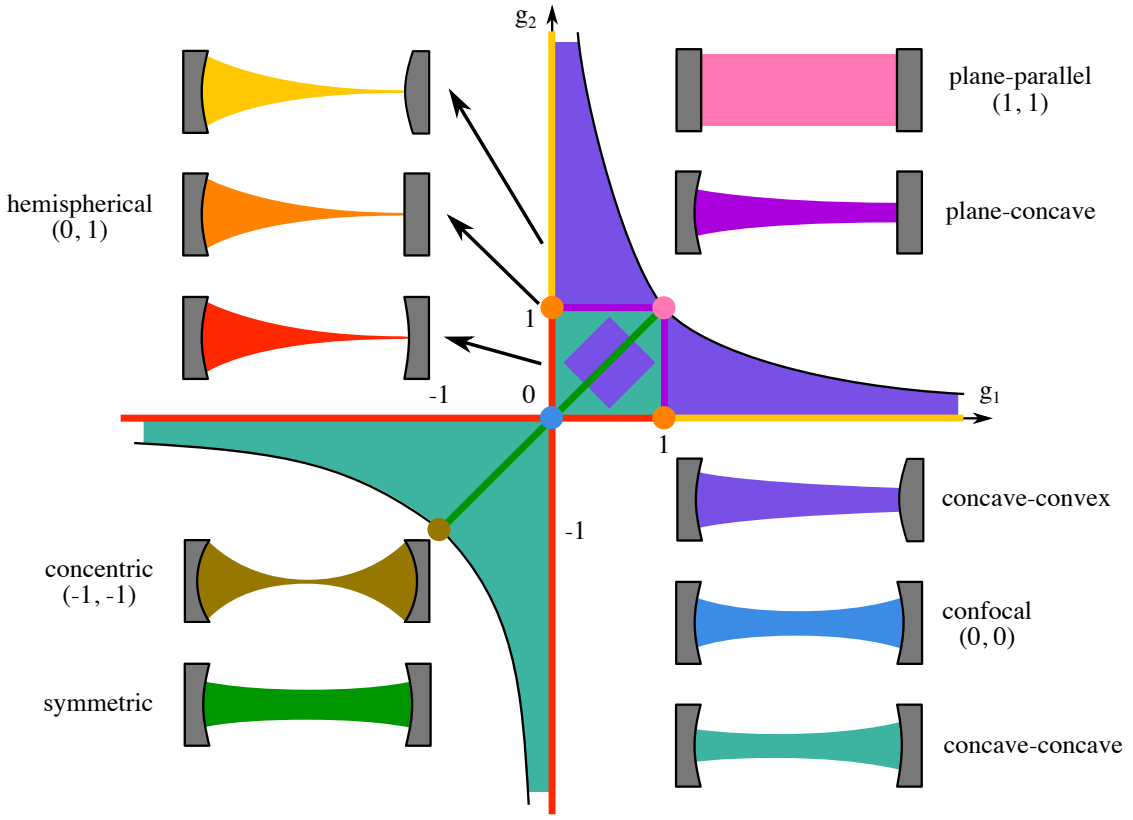

Figure 1.5: The stability diagram of a Fabry-Perot cavity. All coloured regions bounded by the curves $g_1 = 0$, $g_2 = 0$ and $g_1 g_2 = 1$ correspond to stable configurations. The coloured dots, lines and areas represent cavity configurations whose optical field has the same colour. Cavities placed close to the edges are less stable.

detectors, require cavities operating on a stable configuration. Stable resonators produce resonant enhancement of the input excitations, and under a continuous (periodic) excitation they reach a steady state which can last indefinitely and in which the circulating power is maximised. The stability criterion for a Fabry-Perot cavity is given by [47]:

$$0 < (1 - \frac{L}{R_{c1}})(1 - \frac{L}{R_{c2}}) = g_1 g_2 < 1, \tag{1.7}$$

with

$$g_1 = 1 - \frac{L}{R_{c1}}, \quad g_2 = 1 - \frac{L}{R_{c2}}, \tag{1.8}$$

where g_1, g_2 are known as the *g-factor* of the two mirrors respectively. We define $g_c = g_1 g_2$ as the *g-factor of the cavity*. The sign criterion of ROCs is that ROC is

positive when the mirror is concave towards the cavity centre and negative when the mirror is convex towards the centre. Figure 1.5 shows the stability diagram of a cavity. All coloured regions bounded by the curves $g_1 = 0$, $g_2 = 0$ and $g_1 g_2 = 1$ correspond to stable configurations.

It is usually unwise to design a cavity that lies close to the stability boundary. A slight ROC change or displacement of one mirror can drive the cavity out of stability, leading to drastic reductions in circulating power. The advantage of near-unstable cavities is that they provide large beam spot sizes, which leads to a reduction in coating thermal noise for ground-based gravitational wave detectors. Two types of cavities need special mention: the plane-parallel cavity ($g_1 = g_2 = 1$) and the symmetric concentric cavity ($g_1 = g_2 = -1$), as they can both offer large beam spots on their mirrors with compact designs. Another kind of interesting cavity lies on the axis in the stability diagram (except the origin). For example, when $g_1 = 0$ and $g_2 \neq 0$, the mirror m1 has a large beam size while the beam spot on the mirror m2 is focused to a point no matter what R_{c2} is. Specifically, if R_{c2} is infinity (i.e. the mirror m2 is flat), the cavity is called a *hemispherical cavity*. Such a cavity used in our tabletop experiment introduced in Chapter 4.

In this thesis, we use the term *near-unstable cavity* (NUC) to refer to a cavity with parameters that put it close to an edge of the geometrically stable region. The practical stability of the cavity is difficult to determine and the cavity behaviour in this region can be irregular.

1.7 Thermal issues and influences on stability

A series of thermal issues were observed in both the initial LIGO and the initial Virgo detectors [48, 49]. A small part of the high power laser circulating in the arm cavities is absorbed by the high-reflective coatings, which induces thermal gradients in the test masses. Advanced detectors, which are projected to increase the circulating laser power in the arm cavities from the current 100 kW to 750 kW, will

be subject to more substantial thermal issues. The temperature dependence of the refractive index of the ITMs results in *thermal lensing*. Thermal expansion of both ITMs and ETMs lead to mirror surface distortions. These effects can introduce optical aberrations to the wavefront and reduce the level of circulating power. A comprehensive introduction to the thermal issues in Advanced interferometric detectors can be found in [50].

Thermal compensation systems (TCS) are used to reduce the impact of these issues on the performance of the interferometer [51, 52]. The TCS keeps thermal lensing and distortions in check so that the optical loss is kept below a target level. In Advanced detectors, the TCS is implemented by two types of actuators: a CO_2 laser and a ring heater. A CO_2 laser illuminates additional transmissive glass plates, known as the Compensation Plates (CPs), which are placed between the central beam splitter and the ITMs. The additional temperature gradients on the CPs induced by the CO_2 laser compensate the thermal lensing in the ITMs, thus reducing aberrations in the recycling cavities. Thermal resistive ring heaters surround each cylindrical test mass to induce a stable thermal gradient that can tune the ROC of the test masses.

Wavefront sensors are used to measure modal patterns and wavefront aberrations of the beam caused by thermal effects, which provide compensation solutions for the TCS [53, 54, 55]. For stable cavities the consequences of the same amount of thermal drift is smaller than for near-unstable cavities. Stable resonators are also well understood and we use well-defined paraxial Gaussian solutions to describe their behaviour. Optical aberrations lead to couplings from the fundamental mode to higher order modes and can be quantified by calculating the coupling factor [56]. Thus, the compensation of thermal effects in stable cavities can be well guided. For NUCs, however, the thermal compensation is much more difficult, time-consuming and in some cases even unsolvable.

In initial LIGO and initial Virgo, the recycling cavities were designed to be near-unstable due to the limited space available. Thermal drifts altered the stability

of the cavity. Mode patterns changed a lot and even behaved erratically in these cavities when the thermal status of the mirrors was altered. TCSs sometimes failed to maintain high circulating power. To get rid of these problems, as part of the Advanced LIGO upgrades, the original power recycling cavity was replaced by a stable cavity [57, 58]. However, Advanced Virgo still uses near-unstable recycling cavities due to construction time and cost constraints, and the increased suspension complexity required for a stable-cavity solution. Instead, the recycling cavities have been pushed further towards the edge of instability as larger beam sizes have been used [13]. This makes the recycling cavities in Advanced Virgo extremely sensitive to aberrations caused by thermal effects. In order to keep these cavities stable, more stringent requirements are imposed on the thermal compensation system, which promises to be a challenging task.

1.8 Problems of near-unstable cavities

There are two main classes of problems for NUCs that limit their application in gravitational wave detectors. These can be summarised as follows:

1. High optical loss The NUC is extremely sensitive to mirror deformations caused by thermal effects and even mirror surface defects. In NUCs, beam parameters will change significantly in response to a small change in the cavity geometry (discussed in Section 3.2). Mirror imperfections including figure errors, surface roughness and coating non-uniformity couple the fundamental mode more strongly to higher-order modes when compared with a stable cavity. The energy coupled from the fundamental mode to higher-order modes is in many cases effectively lost, leading to a reduced gain. The reduced power in the carrier light will make the interferometer lose signal-to-noise ratio at high frequencies where the laser shot noise is the dominant noise term. As RF sidebands are used to extract signals which control degrees of freedom for the mirrors in the interferometer, the drop in the power in these sidebands will reduce signal-to-noise ratios for these control system [51].

Moreover, ROC changes due to thermal effects can easily drive the cavity to unstable regions where the optical gain reduces dramatically.

2. Gaussian mode degeneracy Gaussian mode degeneracy is caused by having insufficient Gouy phase difference between modes. The degeneracy happens in both the mode frequency and the field amplitude, as power will inevitably be transferred between modes that are co-resonant (discussed in more detail in Section 3.3). In a stable cavity, higher-order modes are strongly suppressed and reflected by the cavity. However, in NUCs, higher-order modes introduced by mirror deformations and mirror surface imperfections in above have the ability to resonate together with the fundamental mode in the cavity. These resonant higher-order modes are coupled to even higher higher-order modes through the mirror, and so on, eventually producing a very disordered beam profile. Furthermore, the superposition of the field between the fundamental mode and higher-order modes will introduce offsets to control signals of length stabilisation and auto-alignments system [59, 60]. These effects will reduce the feasibility of operating the interferometer at its maximum laser power.

1.9 Thesis overview

This thesis focuses on the behaviour of NUCs. As seen in this introduction, a comprehensive understanding of cavity behaviours in the near-unstable region is required. This understanding can benefit the operation of Advanced Virgo and future interferometers that will apply near-unstable cavities.

Chapter 1 gives a brief introduction on gravitational waves, an overview of gravitational wave detectors and noises sources that limit the sensitivity of advanced detectors. In this chapter, the stability of the two-mirror cavity is introduced. A special kind of cavity, the near-unstable cavity (NUC) is the main focus throughout this thesis. Problems of NUCs and motivation of this thesis is given.

Chapter 2 describes the work I carried out in the TCS group in Advanced LIGO Livingston Observatory. The aim was to help the thermal compensation perform more accurately, which can potentially benefit the control of cavity stability. In this chapter, I build up a model that helps monitor the thermal status of the test mass. The mechanical mode frequency is used as an accurate probe of the overall temperature of the test mass. I estimate the coating absorption which is the main reason that causes thermal drifts in test masses. The model is also tuned and tested for long term thermal simulation. This work has been published in [1] and a large proportion of this chapter comes from that paper.

Chapter 3 discusses applications of near-unstable cavities for gravitational wave detectors. Their configurations and features are compared with stable resonators. Behaviours of transverse higher-order modes in NUCs are studied.

Chapter 4 and Chapter 5 describe the tabletop experiment I carried out throughout my Ph.D. investigating behaviours of NUCs. Chapter 4 concentrates on the construction of the tabletop setup, including the cavity design, control systems and characterisation of all optical and electronic devices. The 1 m cavity is built at first in the stable region, tested and then pushed towards the edge of stability by stepwise changing the cavity length. Accurate control is performed on the cavity through longitudinal length stabilisation and angular aligning systems, which allows us to carry out a variety of precise measurements in the near-unstable region. Results are presented in Chapter 5. A series of resonant frequencies and transverse shapes of higher-order modes are measured. We find a way of accurately quantifying the stability of the cavity. Mode patterns and behaviours are well understood up to a certain point. This point is the boundary where the cavity becomes inoperable. Results have been summarised into a paper and will be submitted for publication.

Chapter 6 summarises the conclusion of this thesis and provides a discussion for the future work.

Chapter 2

Thermal modelling of test masses

In advanced gravitational wave detectors, a good knowledge of the thermal status of all test masses is required to aid relieving problems caused by thermal lensing and radius of curvature changes. This will also benefit the thermal compensation system used in current Advanced Virgo as well as future detectors that employ near-unstable cavities. In this chapter, we investigate the method of thermal modelling for the test mass using the mechanical mode frequency as a reference of the average temperature. Core results presented in this chapter have been published in the paper *H Wang, C Blair, M Dovale Álvarez, A Brooks, M F Kasprzack, J Ramette, P M Meyers, S Kaufer, B O'Reilly, C M Mow-Lowry and A Freise. Thermal modelling of Advanced LIGO test masses. Classical and Quantum Gravity, 34(11):115001, 2017* [1].

2.1 Brief introduction

Advanced LIGO is currently the most sensitive length sensing device ever created. The upgraded detectors use high laser power to increase their sensitivity. The arm cavity is composed of fused silica mirrors with high-reflectivity coatings, known as the input test mass (ITM) and end test mass (ETM). The optical power in each cavity will eventually reach 750 kW [61]. A small portion of this power will be absorbed

by test masses and converted into heat. When the arm cavities control systems are locked, resulting in the optical power build-up, the absorbed heat creates a thermal transient in the mirrors [62]. This thermal transient impacts the performance of the interferometer in many ways while the following effects currently dominate the interferometer's behaviours:

1. Thermal lensing [63, 64, 65] is caused by a change of refractive index via the thermo-optic effect. It induces a change in the optical path length within optical components resulting in aberrations in the power recycling and signal recycling cavities [3]. Such aberrations normally contribute to a deterioration of mode matching [51] and can reduce the optical gain, causing a reduced sensitivity of the interferometer.

2. A change in the tuning conditions for parametric instabilities [66, 67, 68] is caused by two factors. First, thermal expansion due to self-heating through coating absorption deforms the high-reflectivity coatings of the test masses. The first order deformation is a change of the radius of curvature (ROC) of the mirror [69], which will shift the frequency of the transverse optical modes (TEM) resonant in the cavity, changing the mode spacing between the fundamental mode and TEM modes (by $\sim 10^3$ Hz). Second, the Young's modulus of the mirror substrates has a small positive thermal dependence which results in an increase ($\sim 10^{-1}$ Hz) in the mechanical mode frequencies as the mirror warms. Parametric instabilities are most severe when the mechanical mode frequency equals the frequency spacing between the fundamental mode and TEM modes, a condition that is altered by the thermal change, where the interferometer may become unstable and inoperable.

3. A change in the cavity stability. This issue is problematic in gravitational wave interferometers that employ near-unstable cavities, such as Advanced Virgo and future detectors that use NUCs to reduce coating thermal noise. Problems of using NUCs have been discussed in Section 1.8.

These issues need to be addressed in order to minimise their impact on detector sensitivity. The power of the circulating beam in arm cavities at Advanced LIGO

during the first observation run was 100 kW and thermal effects were managed with various mitigation strategies [52]. However, these effects will become more severe in future as the detectors employ higher laser power to reach design sensitivity. Many of the current mitigation strategies will therefore require further attention.

To aid the design and development of such strategies, a good thermal model of test masses, along with good estimates of their coating absorptions, is required. Monitoring the coating absorption also provides a means of identifying coating damage or contamination. The coating absorption of Livingston's Y-arm end test mass (ETMY) was measured to be less than 0.5 ppm [70, 71] before installation. New on site thermal lensing measurements recently showed that the coating absorption of ETMY is 2.1 ppm [72]. The increased coating absorption may be indicative of such contamination.

In this chapter, we build a thermal model of the test mass and its surroundings that uses shifts in mechanical mode frequencies as a probe for the overall temperature of the mirror. Thermal transients on the time scale of minutes to a few hours are well understood, which enables us to estimate the energy absorbed by the ETMY coating. Scattered light heating surrounding elements is observed and introduced in the model. A model of the long term thermal behaviour of the test mass is then introduced, where complex structures in the vicinity of the optic are simplified to a single element. Such an empirical model helps predict the thermal behaviour on the time scale of tens of hours.

This model provides good estimates of the coating absorption of the ETMY of the Livingston detector. Using the model for ongoing absorption monitoring provides early warning for potential contamination or degradation of test masses and tracking mechanical mode frequencies that might be relevant for parametric instability mitigation strategies.

2.2 Using acoustic modes as temperature probes

Mechanical mode frequencies can be used as very accurate test mass thermometers. This technique was first introduced by M. Punturo and F. Travasso in 2001 [73] as a method to characterise the mirror absorption of the French-Italian gravitational wave detector Virgo [74, 10, 13]. Mechanical mode frequencies depend on the mirror dimensions and on two material properties that have a temperature dependence: the Young's modulus and the Poisson ratio. The eigenfrequencies of a cylinder can be expressed analytically as [75, 76, 77]

$$\omega_m = \beta_m \sqrt{\frac{E}{\rho(1+\nu)}}, \tag{2.1}$$

where β_m is a parameter encompassing several aspects of cylinder dimensions and has restricted values, E is the Young's Modulus, ν is the Poisson ratio, and ρ is the density of the material.

Our model shows that the change in eigenfrequencies due to the thermal expansion of the substrate is negligible when compared to the change due to the temperature dependence of E and ν. Most materials soften with increasing temperature, but fused silica's Young's modulus increases in the $(-200, 1100)\,^{\circ}\mathrm{C}$ interval [78, 79] and the rate of change at 17 °C is 11.5 MPa/K. The Poisson ratio of fused silica also increases in the $(0, 1200)\,^{\circ}\mathrm{C}$ interval with a rate of $5.5 \times 10^{-5}/\mathrm{K}$ at 17 °C [78, 80]. These rates can be considered constant within the small temperature range considered here of $\pm 0.6\,^{\circ}\mathrm{C}$ around 17 °C. Equation 2.1 implies that temperature-induced changes of E and ν have contributions with opposite sign to the mechanical mode frequencies with a ratio of $3.4 : -1$. Therefore, the change in the mechanical mode frequencies due to the change in Young's modulus dominates over the change due to the Poisson ratio, and the eigenfrequencies increase as the test mass becomes warmer.

Mechanical modes of test masses are sensed at the cavities' transmission port when the cavities are locked, and we experimentally track the frequency of the 15.5 kHz

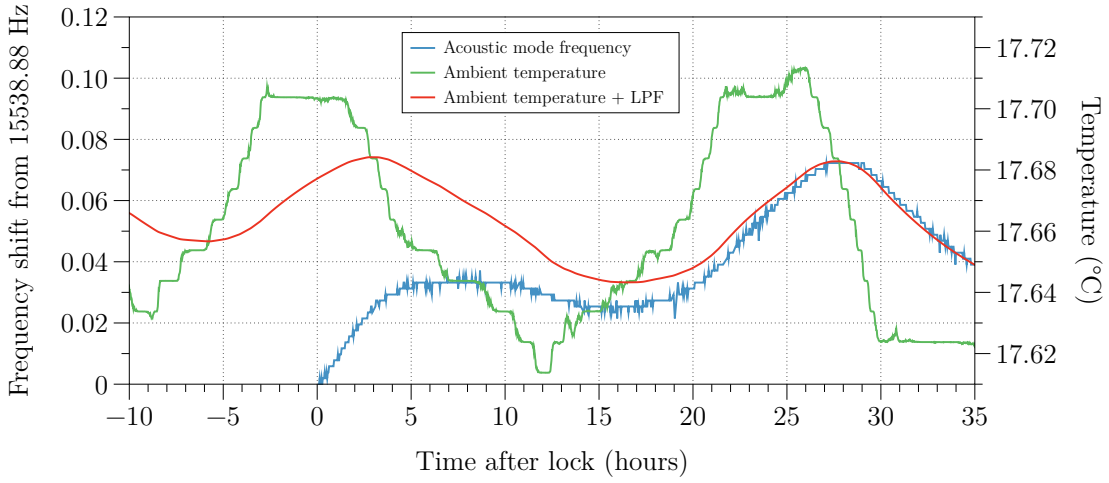

Figure 2.1: Frequency shift of the 15539 Hz eigenmode of LIGO Livingston's ETMY and ambient temperature fluctuations during a 36 hour lock.

mode of ETMY using a quadrant photodetector on the y-arm transmission port [81, 68]. We focus on this mode because it has significant sensing gain. Its frequency is read out through the power spectrum density of the photodetector's signal. Figure 2.1 shows the mode's frequency shift over a 36 hour lock on 8th October 2015 (blue curve). The figure also shows the ambient temperature data as measured by a sensor inside the vacuum tank. The green curve represents the raw sensor data and the red curve represents the data after a one-pole low pass filter is applied with a time constant of 7.2 hours [1] determined by our finite element model. We can see about 25 hours into the lock that the frequency change is completely determined by the ambient temperature fluctuation.

[1]The time constant relates to the test mass itself only and does not include the surrounding chamber.

2.3 Heat transfer model of Advanced LIGO test masses

2.3.1 Thermal couplings

To improve the accuracy of our thermal modelling, we include the radiative heat transfer between the mirror and elements in proximity of the mirror.

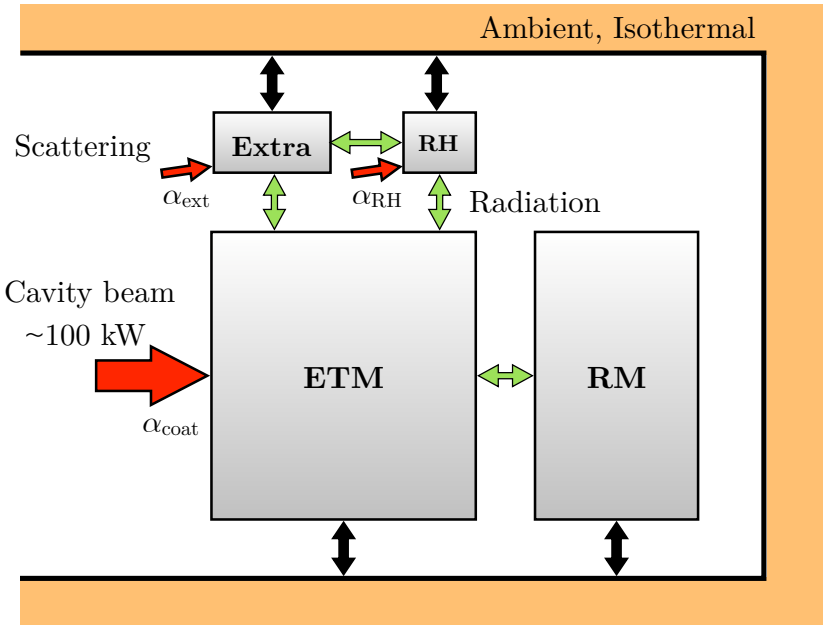

Figure 2.2: A heat transfer model between an end test mass (ETM), a reaction mass (RM), a ring heater (RH), the ambient isotherm, and an extra term representing the complex structures surrounding the test mass that could not be modelled in detail. Red arrows represent energy coming from the intra-cavity beam through coating absorption or scattering. Green arrows represent the radiative heat couplings between different elements and black arrows the radiative heat couplings with the ambient.

Figure 2.2 depicts different mechanisms by which heat is transferred in the system. When the arm cavity is locked, ∼100 kW of laser power is incident on the test masses. The absorption, in the order of 1 ppm, of the high reflectivity coatings results in a portion of the light being converted into heat. In addition, scattered light from the beam illuminates elements surrounding the mirror, part of which will be absorbed and converted into heat by those elements.

Some of the heat from absorbed scattered light radiatively couples to other elements, introducing longer time constants to the test mass thermal transient. The surrounding elements used in this model are the reaction mass, the ring heater, and an empirical element called the 'extra term' that is a simplification of all other nearby objects.

Finally, all elements will exchange heat with the ambient via radiation. The ambient temperature is recorded by a sensor in the vacuum tank, and the data from this sensor is included in the model. The amount of scattered light hitting the reaction mass as well as the radiative coupling between the reaction mass and the ring heater are negligible and have been omitted from Figure 2.2 for simplicity.

2.3.2 Ambient temperature effect

We can treat each of the heat transfer mechanisms discussed in the previous section for the test mass as having a linear effect on its mechanical mode frequency. This constitutes a good approximation since each process only changes the overall temperature of the test mass by approximately 0.2°C around room temperature. The mechanical mode frequency change of the mirror can thus be expressed as:

$$\Delta f_m(t) = \Delta f_{\text{laser}}(t) + \Delta f_{\text{surroundings}}(t) + \Delta f_{\text{ambient}}(t) \tag{2.2}$$

where the terms on the right hand side correspond to contributions from the laser heating of the ETM, the radiative heat transfer with its surroundings (ring heater, reaction mass and extra term), and the radiative heat transfer with the ambient respectively.

We examine mode frequency data from 5 locks where the cavity was in a *clean* thermal status. The clean status means that light wasn't circulating in the cavity for at least 30 hours prior to the lock, and therefore the test mass and surrounding elements were, to a good approximation, in thermal equilibrium.

For each lock, $\Delta f_{\text{laser}}(t)$ and $\Delta f_{\text{surroundings}}(t)$ are calculated by our finite element model while $\Delta f_{\text{ambient}}(t)$ is not. Instead, it is included by applying the low-pass filter to the measured ambient temperature data as shown in Figure 2.1. More data is shown in Appendix B.1.

2.4 Finite element model

We use COMSOL Multiphysics to build a model of the whole thermal system. The heat transfer module is attached to the model to calculate the temperature of the ETM and the ring heater over time. A solid mechanics study is attached to the module calculating eigenfrequencies of the ETM at each time point.

The only input of the model is the laser power step function that is 0 when the cavity is unlocked and when the cavity is locked the measured power is typically 100 kW. The actual time to reach full power can be up to 40 minutes but this has no significant effect on the thermal evolution modelled here. Outputs are the frequency shift of the 15539 Hz mechanical mode and the ring heater temperature change as a function of time. The output data, after adding the ambient temperature influence, is compared with the measured data. There are several free parameters that we can tune to fit our model to the measured data, discussed later in this section. Figure 2.3 provides an input-output diagram for this model.

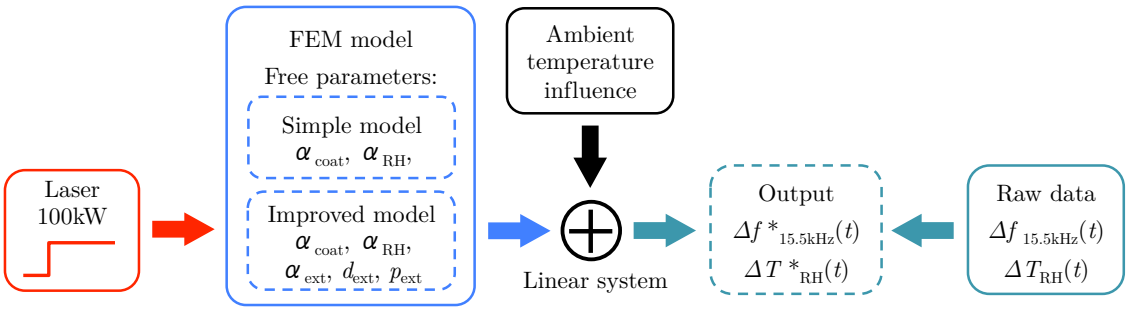

Figure 2.3: Inputs, outputs, and free parameters of the finite-element model.

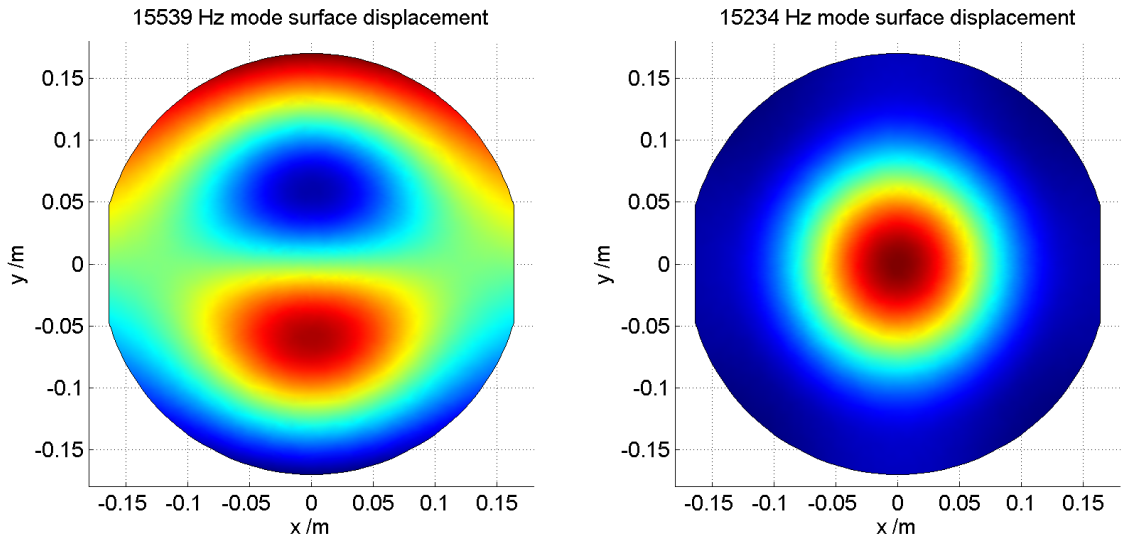

Figure 2.4: Surface distortions of the 15539 Hz "second order drumhead" mechanical mode and 15234 Hz "circular drumhead" mode.

2.4.1 2D-axisymmetric model

In a finite element modelling work, it is important to choose a proper model which can make you much more time-efficient. The Advanced LIGO test mass is almost a cylinder but is cut off by two parallel plates on the edges for holding suspension fibres. It is obvious that using a 2D-axisymmetric (2DAS) model requires much less computational resources than using a more practical 3D model with all details. Before using a 2D-axisymmetric model, we investigated the error in mechanical mode frequency shift between a 2D-axisymmetric model and a 3D test mass with two cut blocks. The mesh size is another important parameter that we need to consider as the computing time increases exponentially when the mesh size getting smaller and smaller.

The 15539 Hz acoustic mode is like a "second order drumhead" mode (see the left plot in Figure 2.4). In COMSOL, only axisymmetric modes will be calculated under the 2D-axisymmetric model. We choose the 15234 Hz mode (the right plot in Figure 2.4) which is the closest "circular drumhead" mode to the 15539 Hz. Table 2.1 shows the eigenfrequencies that COMSOL gives to us using different models including the

Table 2.1: Comparison of mode frequencies using different models and mesh sizes.

15539 Hz mode

Mesh size	3D ETM		3D Cylinder	
	f [Hz]	diff [Hz]	f [Hz]	diff [Hz]
Coarse	15569.890099		15551.869519	
Normal	15540.660151	29.229948	15526.875780	24.993739
Fine	15535.871191	4.788960	15521.362988	5.512792
Finer	15532.856261	3.014930	15518.344829	3.018159
Extra fine	15532.142607	0.713654	15517.634469	0.710360
Extremely fine	out of memory		out of memory	

15234 Hz mode

Mesh size	3D ETM		3D Cylinder		2DAS Cylinder	
	f [Hz]	diff [Hz]	f [Hz]	diff [Hz]	f [Hz]	diff [Hz]
Coarse	15249.476188		15198.192821		15179.347716	
Normal	15233.827974	15.648214	15183.786869	14.405952	15178.758857	0.588859
Fine	15230.850844	2.977130	15180.765766	3.021103	15178.655722	0.103135
Finer	15229.126177	1.724667	15179.059136	1.706630	15178.600263	0.055459
Extra fine	15228.698882	0.427295	15178.660985	0.398151	15178.583870	0.016393
Extremely fine	out of memory		out of memory		15178.582408	0.001462

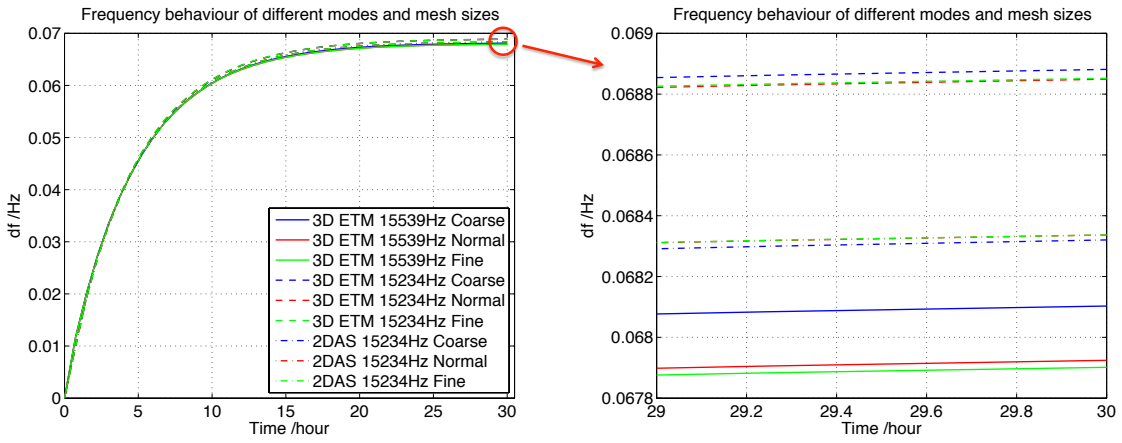

Figure 2.5: The frequency behaviour of different modes using 3D or 2D-axisymmetric models with different mesh size. The maximum error is less than 1.4% after 30 hours' self-heating with 1 ppm coating absorption. The difference between 15234 Hz mode of the 2D-axisymmetric cylinder and 15539 Hz mode of 3D ETM with real shape is just 0.6%.

3D ETM in real shape (with two cut blocks), a 3D cylinder and a 2D-axisymmetric cylinder with different mesh sizes. The top table gives 15539 Hz mode frequencies calculated by COMSOL in a real 3D model and a 3D cylinder model with different mesh sizes. The *diff* means the frequency difference between two contiguous mesh size options. The bottom table gives 15234 Hz mode frequencies in a a real 3D model, a 3D cylinder model and a 2D-axisymmetric model. We can see that the

absolute eigenfrequencies strongly depend on the shape of the test mass and the mesh size used[2]. But here we only care about the eigenfrequency shift over time in our thermal transient model. Figure 2.5 shows that the maximum error using 15234 Hz mode in the 2D-axisymmetric model is just 0.6% from using the 15539 Hz mode in the real 3D ETM model after 30 hours' laser beam heating supposing 1 ppm coating absorption.

2.4.2 A simple model

We start by building a simple model that only considers the end test mass, the reaction mass and the ring heater, because these components have regular shapes and can be easily modelled in COMSOL.

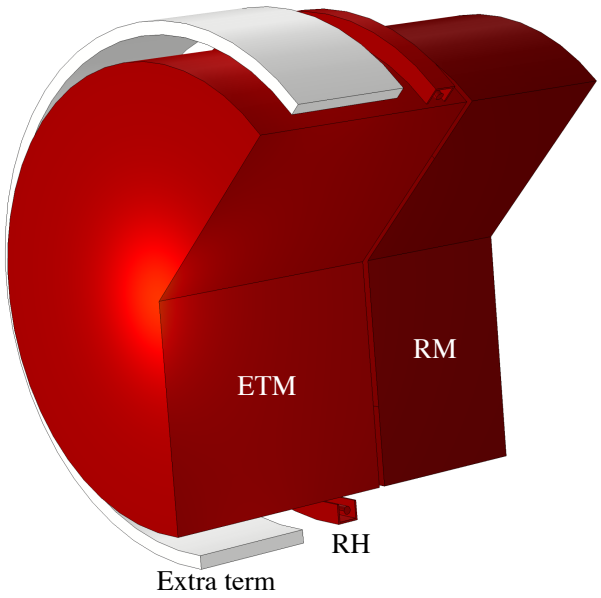

Figure 2.6: 3D view of the geometry of the ETM, ring heater, reaction mass, and extra term as modelled in COMSOL (225° slice). Geometric parameters of the model are shown in the appendix.

[2]The material property is another factor that determines the eigenfrequency, especially the Young's modulus.

End test mass

The Advanced LIGO ETM is a cylinder with a 170 mm radius and 200 mm thickness made of Heraeus Suprasil 3001 fused silica. When the 100 kW laser beam impinges on it, the high-reflectivity coating of the ETM absorbs some energy and converts it into heat. In the model, a heat source boundary condition with a Gaussian profile is used to simulate the beam spot on the mirror surface. The intensity of a Gaussian beam with beam radius w and power P_0 at a distance r from the beam axis is

$$I(r) = \frac{2P_0}{\pi w^2} \exp\left(-\frac{2r^2}{w^2}\right) \ \mathrm{W/m^2}, \tag{2.3}$$

where w =6.2 cm and P_0 is the circulating laser power heating the ETM, measured by a photodetector, which is around 100 kW. The energy absorbed by the coating is given by $\alpha_{\mathrm{coat}} I(r)$ where α_{coat} is the absorption coefficient of the coating. For a laser power of 100 kW, a coating absorption of 1 ppm corresponds to a total absorbed energy of 0.1 W. The high reflectivity and low transmission of the ETM coating result in negligible absorption in the substrate.

Reaction mass

The reaction mass (RM) is another fused silica cylinder with the same radius as the ETM, but a thickness of 130 mm. It is located coaxially 5 mm away from the rear surface of the ETM. Its primary purpose is to allow longitudinal actuation of the test mass via an electrostatic force.

Ring heater

The ring heater (RH) is a glass ring surrounding the ETM that is wrapped with nichrome wire and surrounded by a U-shaped aluminium shield. The inner surface of the aluminium shield is gold-plated to reflect infra-red light. The ring heater is used to create a thermal gradient to compensate for the change in radius of curvature

induced by laser heating on the surface of the optic [52, 82]. There is a thermometer inside the ring heater shield monitoring its temperature. During O1 the power fed to the ring heater was small and fixed (approximately 1 W), changing the ring heater temperature by 0.25°C at around 18°C from the initial cool status with zero power. Since the ETM-RH system was in thermal equilibrium during our measurements we don't take this gradient into account, as it has a negligible effect on the ETM's temperature fluctuations. The ring heater is, however, subject to scattering by the ITM and ETM. The thermal sensor inside the ring heater shield registers a rise in temperature during the first five hours of each lock. In our model this is described by a heat source on the surface of the ring heater shield facing the cavity. The contribution of ambient temperature fluctuations to the ring heater temperature is determined in a process similar to that in section 2.3.2. The finite element model predicts a time constant for a simple low-pass filter of approximately 1.43 hours.

Material properties of fused silica and aluminium used in the model are listed in Table 2.2.

Table 2.2: Material properties.

Property	Symbol	Fused silica	Aluminium	Unit
Density	ρ	2203	2700	kg/m^3
Young's modulus at 16°C	E	73×10^9	–	Pa
dE/dT at 17°C [a]	dE/dT	11.5×10^6	–	Pa/K
Poisson's ratio	ν	0.17	–	–
$d\nu/dT$ at 17°C	$d\nu/dT$	5.5×10^{-5}	–	1/K
Thermal conductivity	k	1.38	160	W/(m·K)
Thermal expansion coefficient	α	5.5×10^{-7}	–	1/K
Heat capacity	C_p	740	900	J/(kg·K)
Relative permittivity	ϵ	3.8	1	–
Surface emissivity	ϵ_e	0.93	0.1 [b]	–

[a] This property has been found to be constant over a 40°C temperature range as $(dE/dT)/E = +1.52\times10^{-4}$/K [83].
[b] See Appendix B.5.

There are only two parameters we can tune in the simple model: the energy absorbed by the ETM coating from the laser beam (α_{coat}) and the energy absorbed by the ring heater surface from the scattered light (α_{RH}). These two parameters are constrained

by the thermal transient in the initial hours of lock (see Figure 2.7). After two hours this simple model fails to match the measured data, discussed in section 2.5.

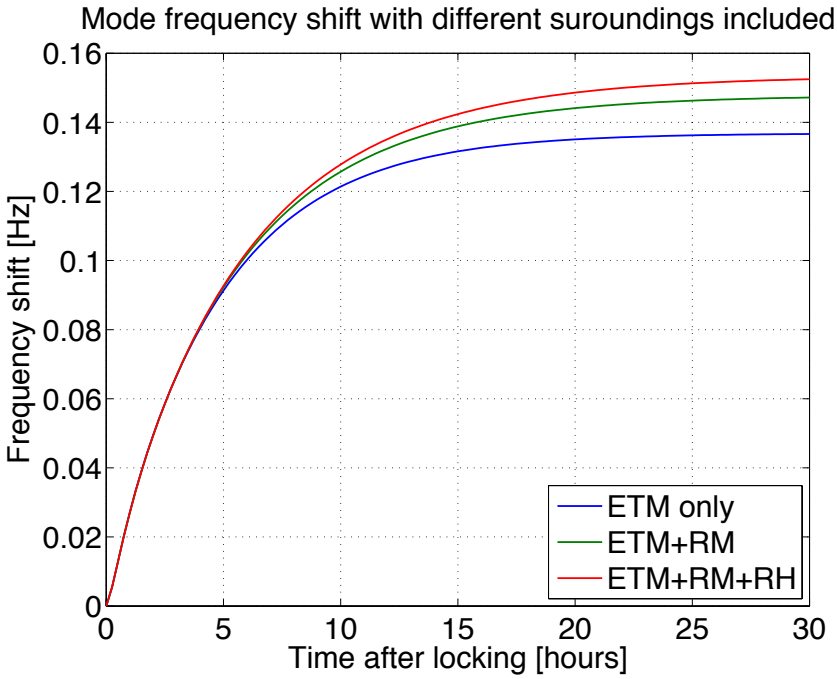

Figure 2.7: The thermal transient of the ETM with different surrounding included during 30 hours' lock with 1ppm coating absorption. The initial thermal transient is entirely determined by the absorption. The model that takes into account the ring heater and the reaction mass has a larger mode frequency shift at the equilibrium than the model with the ETM only. This is due to the thermal radiation between the ETM and its surroundings. But the thermal radiation has a much slower time constant and will not affect the initial thermal transient after the lock.

2.4.3 The improved model

The short term thermal behaviour of the system is reliably predicted by the simple model. The reliability of long-term models, however, depends on how accurately test mass surroundings are modelled. Simulating all surrounding elements in detail quickly becomes an impractical task as the computation time rises exponentially with each new radiative surface. To approximate effects of all elements in the vicinity of the test mass we improved the simple model by introducing the extra term, an aluminium annulus that surrounds the ETM (see Figure 2.6). This extra term couples to the ETM radiatively and also receives scattered light from the cavity. By

doing this, we obtain another three free parameters to tune: the energy absorbed by the extra term from the scattered light (α_{ext}), and dimensional and position parameters for the extra term (d_{ext} and p_{ext} [3]), shown in detail in B.2. The method used to tune the improved model are shown in the next section.

2.5 Creating an accurate long time-scale model

The finite element model calculates eigenfrequencies of the ETM over time and compares results with measured data. Tuning the model required three steps:

1. The laser heating term is estimated from the first three hours of the lock where the dominant term is coating absorption. This gives an estimate of the coating absorption coefficient, α_{coat}.

2. The ring heater scattered light heating term is also estimated from the first hours of the lock. The temperature recorded by the ring heater sensor is used to estimate the amount of scattered light absorbed by this element α_{RH}.

3. Finally parameters of the extra heating term are obtained. Setting α_{coat} and α_{RH} from the previous two steps the extra term parameters are chosen to minimise the residual between the measured data and the long-term simulation of the test mass, including all heat transfer effects depicted in Figure 2.2. The parameters adjusted are dimensions, scattered light absorption and the proximity of the ring to the test mass.

2.5.1 Coating absorption measurement

The first three hours of several locks is used to estimate the energy absorbed by the Livingston ETMY coating. We chose 5 lock periods from April to December 2015 (information of each lock is shown in B.3). These lock stretches were chosen

[3] We only chose these two geometric parameters for the extra term as others largely degenerate with them.

because in each case there was no light in arm cavities and no anomalies in the laboratory temperature for at least 30 hours prior. This justifies the assumption that the test mass is in thermal equilibrium with its surroundings at the start of the lock. The raw data from these locks is shown in the left plot of Figure 2.8. The circulating power varied from 105 kW to 112 kW within the lock segments used here (see Appendix B.4). We have linearly scaled the measured coating absorption to the 100 kW beam.

The right plot of Figure 2.8 shows the *corrected data*, where ambient temperature effects are removed from the raw data. The simulated (black) curves display the effect of coating absorption for 1.5 to 2.0 ppm of the laser power. It is clear that the slow radiative effects start affecting the test mass temperature after about 1.5 hours. All 5 locks display a similar trend but don't exactly overlap. The data seem to bunch in two groups. We suspect this is due to some unmodelled effects of the interferometer. There are many possible explanations for the small differences in the 5 traces, such as error in ambient temperature measurements, the long-term ambient temperature to test mass temperature transfer function (see section 2.6), other heating terms including in-vacuum electronics or difference of the alignment of the arm cavity and the beam heating position in each lock.

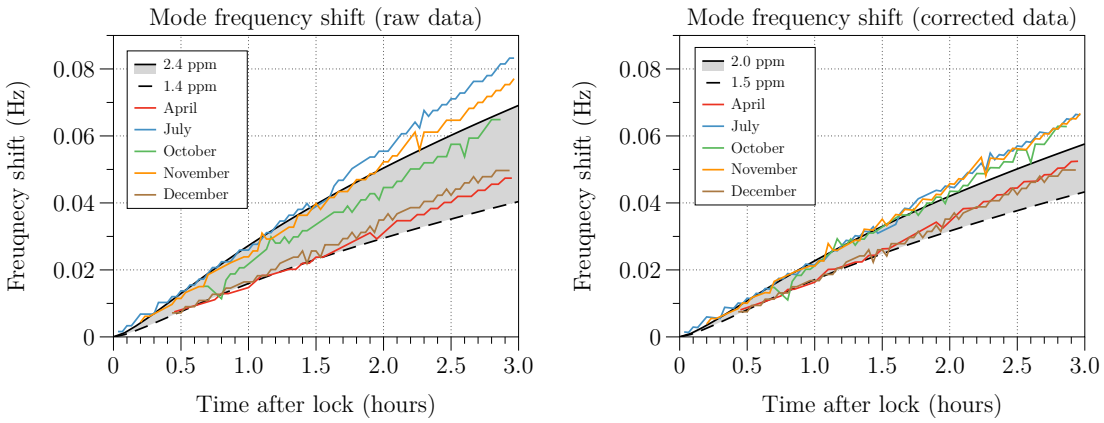

Figure 2.8: Mode frequency shift data from the first 3 hours after lock. The raw data shows a disagreement because the ambient temperature, the alignment of the arm cavity and the beam heating position in each lock are different. After ambient temperature effects are removed from the data, the trends are in better agreement with modelled coating absorptions of 1.5 to 2.0 ppm.

2.5.2 Scattered Light

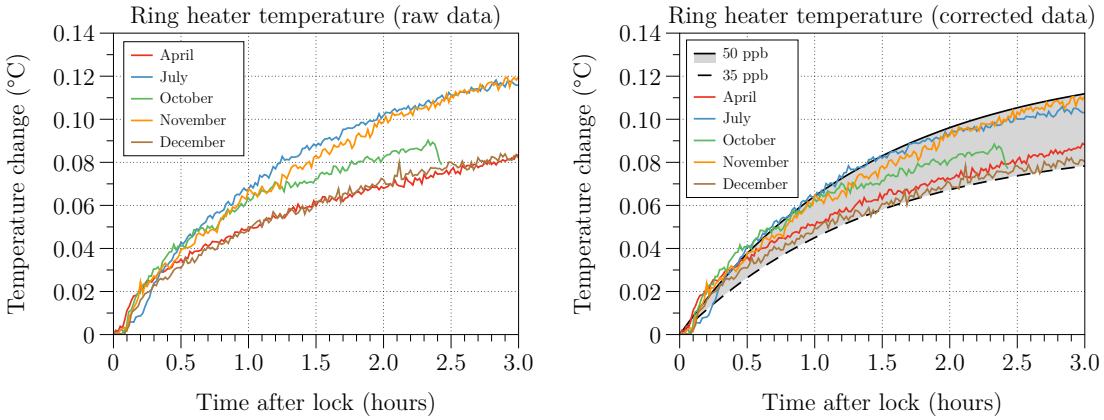

Figure 2.9: Ring heater temperature data from the first 3 hours after lock. After removing ambient temperature effects, the data agrees with the models for between 35 ppb and 50 ppb of ring heater absorption.

The scattered light absorbed by the ring heater completely dominates the initial thermal transient of this element. The data from the ring heater temperature sensor is compared to the model absorption estimates in Figure 2.9. We obtain estimates for α_{RH} of 35 to 50 ppb of the laser power in the cavity. The absorption of aluminium at 1064 nm varies greatly between 4% and 12% depending on the surface roughness and the thickness of the oxide layer [84]. As a result, the estimated scattered light incident on the ring heater could range from 0.3 to 1.25 ppm of the 100 kW beam. This energy can come from the small angle scattering of the ITMY or the large angle scattering of the ETMY. For example, the estimated small angle scattering from the ITMY is about 10 ppm [85].

2.5.3 Long-term simulation

We use the lock period of April 12, 2015, lasting for 31 hours, to tune the parameters of the extra term in the model in this section.

Our long-term model includes the ETM, reaction mass, ring heater, and the extra term depicted in Figure 2.2. The coating absorption is set to the medium value of the estimated range which is 1.8 ppm, as derived in section 2.5.1. The scattered light

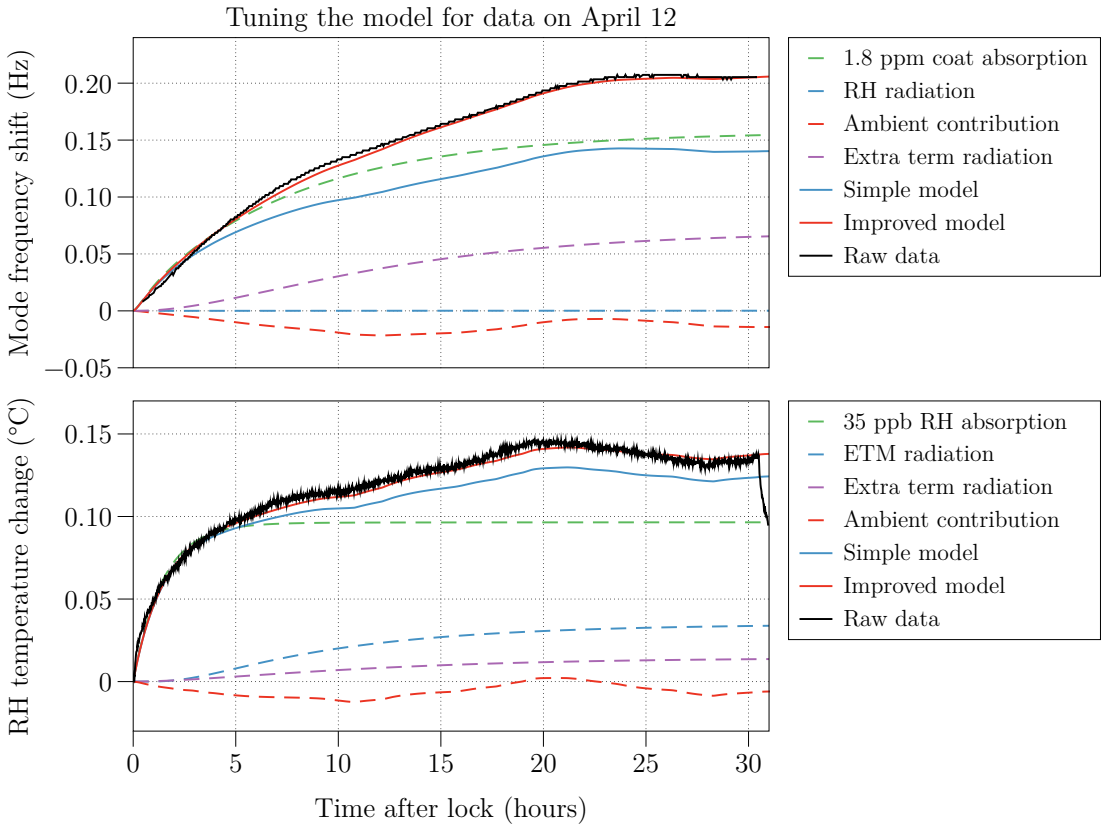

Figure 2.10: Long-term comparison of the April data (black curves) with both models. As temperature changes are small the system is linearised such that the contributions of the various components can be examined separately.

absorbed by the ring heater is chosen to be 35 ppb of the circulating laser power, because this value agrees better with the April data, as derived in section 2.5.2. Finally the ambient heating term is generated using the similar method shown in Figure 2.1.

In Figure 2.10 a linear decomposition of the contributions to the model are displayed. On the top, the green dashed line shows the coating absorption component of the 15.5 kHz mode frequency change. The ring heater scattered light heating component is shown dashed blue, it turns out to be very small. The red dashed line is the ambient temperature contribution to the mode frequency change. The sum of these three contributions determines the simple model shown in solid blue. In the improved model, the parameters of the extra term (d_{ext}, p_{ext} and α_{ext}) were adjusted based on visual comparison and the resulting error was reduced to less than 5%. On

the bottom the ring heater measured data (black curve) and the component heating terms from our model are shown. The green dashed line is the ring heater scattered light absorption term, the blue dashed line is the radiation influence from the ETM and the dashed red is the ambient contribution. The solid blue and red lines are the sum of component terms corresponding to results of the simple model and improved model respectively.

We can see in both sub-plots that the simple model deviates from the data after about 2 hours. The slow effect indicates radiative coupling, resulting in an maximum error of 40% in mode frequency change. The extra term geometry parameters, d_{ext} and p_{ext}, were chosen to match the time constant of the residual based on visual comparison. The extra term absorbed power parameter, α_{ext}, was subsequently tuned to minimise the residual between the model output and measured April data; also its value is chosen within the range of the small angle scattering loss from ITMY which is up to 10 ppm.

2.6 Testing the model

Figure 2.11 shows results of applying the model developed with the April data set to a dataset starting December 21, 2015. The first lock lasts 17 hours and is followed by 3 locks each of about 10 hours. The black curve is the raw data and the red curve is the prediction from the improved model.

There is good agreement between the model and the measured data in the first lock period, where the deviation between model and experiment is only 3%. However, there is significant deviation in subsequent locks, caused by different long-term behaviours measured from the ring heater temperature sensor and the ambient temperature sensor. As shown in the lower plot in Figure 2.11, the measured ring heater temperature (black curve) at the beginning of the 4th lock is lower than at the start of the 1st lock, where we expect a thermal equilibrium state. This can be only explained by a decrease in ambient temperature. However, the ambient temperature

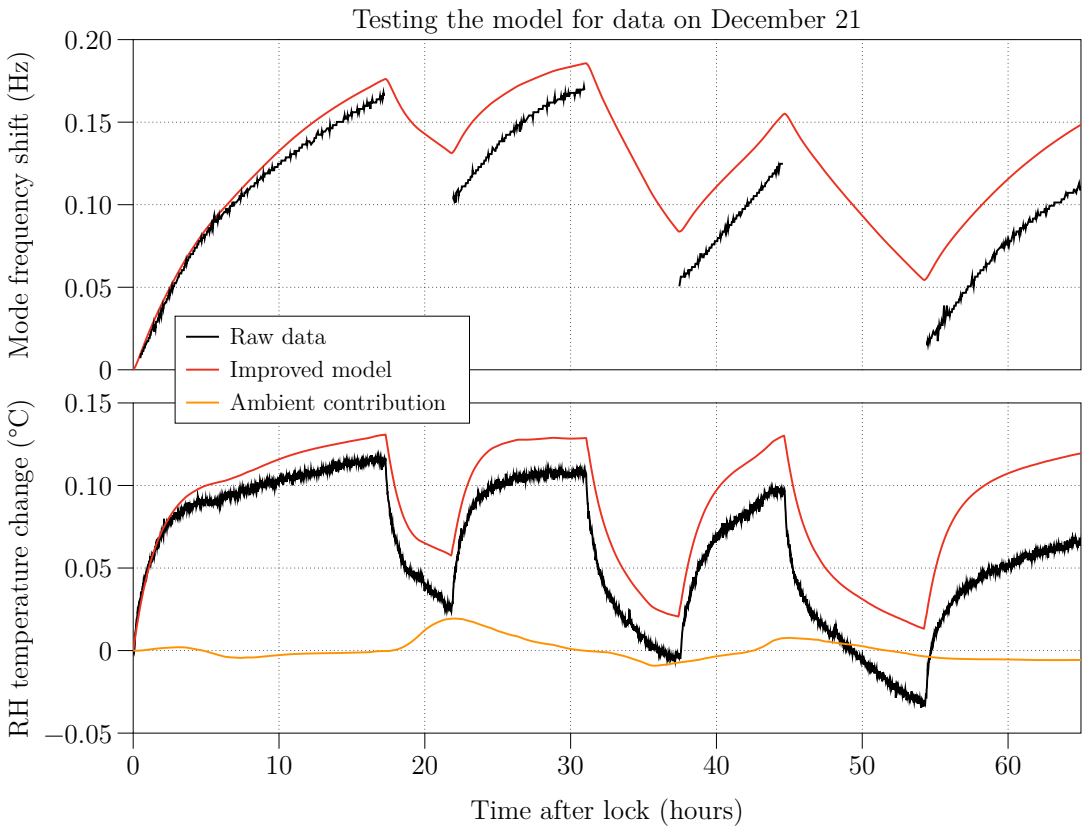

Figure 2.11: Testing the tuned model with the December lock data. The black line is the raw data, the red curve is the improved model, and the orange line in the lower plot represents the ambient contribution to the ring heater temperature.

sensor we used displays a flat trend. Data stretches from long locks starting from a clean thermal state are rare, and further tests of this model will require data from LIGOs second observation run.

Despite the possibility that the ambient temperature sensor data is corrupted, we demonstrate a good model estimating the ETMY temperature over the first 17 hour lock. We expect an improvement in the model accuracy given reliable ambient temperature data and following investigations of long-term features of the transfer function from ambient temperature to test mass temperature.

2.7 Conclusion

Mechanical mode frequencies can be used as very accurate thermometers. We have provided an estimate of LIGO Livingston's ETMY coating absorption of 1.5 to 2.0 ppm. The scattered light incident on the ring heater is estimated to be 0.3 to 1.3 ppm. We have described a thermal model that estimates the test mass temperature in a long-term scale. The accuracy of the thermal model of the test mass was improved with the addition of an extra term to account for radiative contributions from objects in the vicinity of the test mass. The model is tuned to a data set from April, matching the ETMY measured temperature shift within 5%. The model is then tested on a data set from December. The agreement is good over the first 17 hour lock but deviates significantly in subsequent locks. We expect to improve the model further when reliable ambient temperature sensors become available.

Chapter 3

Near-unstable cavities

The stability of a cavity is a geometric property of the cavity, which characterises how the transverse dimensions of the beam (the beam 'spot size') evolve when it is reflected multiple times within the cavity. If the beam is reflected and refocussed such as to maintain a finite transverse size for an arbitrary number of reflections, the cavity is classed as being 'stable'. If, on the other hand, the beam spot size grows without limit upon multiple reflections, the cavity is referred to as being 'unstable'. The property of stability is independent of the mirror reflectivities, although the practical consequences of having a given stability can depend strongly on the cavity finesse.

Most cavities used in interferometers will use stable resonators, because these have well-defined eigenmodes which can be used for control signals, and they can provide high cavity gain without experiencing clipping and diffraction. There are some applications in which unstable cavities may be preferable; for instance in high power lasers, where their large mode volumes can produce a higher gain [86, 87]. Characterising mode behaviours of unstable cavities are quite difficult. Some methods can be found in [88, 89].

The near-unstable cavities (NUC) studied in this thesis are cavities that have a stable geometric configuration but are very close to the edge of the stability. NUCs

have previously been employed in atomic physics applications, in order to increase the photon-atom interaction time [90, 91]. However, as introduced in Section 1.8, this kind of cavity can easily lose stability, as a small length perturbation or radius of curvature (ROC) change in a mirror may push the cavity over the boundary of the region of stability. Wavefront aberrations introduced by surface imperfections and deformations can scatter light out of the beam path, which will in most cases appear as losses, but also from the fundamental mode into higher order modes, which will affect the cavity's effectiveness as an optical filter. NUCs have more stringent requirements on the surface quality of the mirrors than standard stable cavities.

3.1 Application for gravitational wave detectors

There are two broad areas for studying NUCs in gravitational wave detectors: 1. Current detectors employ these cavities in the stable region, but thermal perturbations may drive them towards the near-unstable or even the unstable region. 2. Future detectors may use them because of their large beam spot leading to a reduction of thermal noise. These two cases are described in more detail below. There has so far been no reported systematic investigation into the behaviour of NUCs for gravitational wave detectors. In this thesis, we investigate NUCs as applied to these two areas.

Advanced Virgo uses the power recycling cavity and the signal recycling cavity in a near-unstable configuration. It requires TCSs to maintain ROCs of ITMs, as well as strict requirements on mode matching and mirror flatness. The effectiveness of the TCS is, however, limited by the precision of the readout mechanism in the feedback loop. At present, the thermal status of the ITM can be modelled quite precisely [92, 93, 82], and thermally induced aberrations can be measured by Hartmann sensors [94] and phase cameras [60, 55], which can be translated into a predicted change in stability. The control of the TCS would, however, benefit if the stability of the cavity could be measured directly.

Despite the disadvantages listed above, NUCs are being considered for use in arm cavities in future gravitational wave detectors, due to their larger beam spot size on cavity mirrors, which can provide a reduction in coating thermal noise [95, 96]. Beam sizes on mirrors depend on the cavity length and ROCs of mirrors. As the cavity length in the interferometer is essentially fixed first in the experimental design, to achieve the large beam size needed, we can then choose adequate ROCs to push the cavity's configuration towards the boundary of geometric stability. Cavities in such cases would easily lose stability and thus practical issues need to be addressed.

In the following sections, I will summarise some general characteristics of NUCs with different configurations.

3.2 Configurations

3.2.1 Recycling cavity in Advanced Virgo

The current recycling cavity in Advanced Virgo is a concave-convex cavity (CVC) with a cavity length of 11.952 m, formed by the power (or signal) recycling mirror with a ROC of 1430 m and the input test mass with a ROC of 1420 m [13]. Both mirrors are placed in the same side of the waist of the eigenmode, shown in Figure 3.1. As their ROCs are much larger than the cavity length, the cavity is near-unstable with a g-factor extremely close to 1 ($g_c = 0.9999885$). The stability criterion requires the ROC of the power recycling mirror, Rc_1, to be smaller than the sum of the ROC of the ITM, Rc_2, and the cavity length, L, that is $Rc_1 < |Rc_2| + L$. Notice that here Rc_2 is negative according to the sign criterion introduced in Section 1.6.

For a near-unstable concave-convex cavity, given a small ROC deviation, the change in waist position is much more significant than that in beam spot size. In Figure 3.1, we show an simulated example in which the cavity stability is tuned from a stable region (the top plot) to the near-unstable region (the bottom plot) by changing the ROC of the ITM by tens of metres. If this happened in Advanced Virgo using

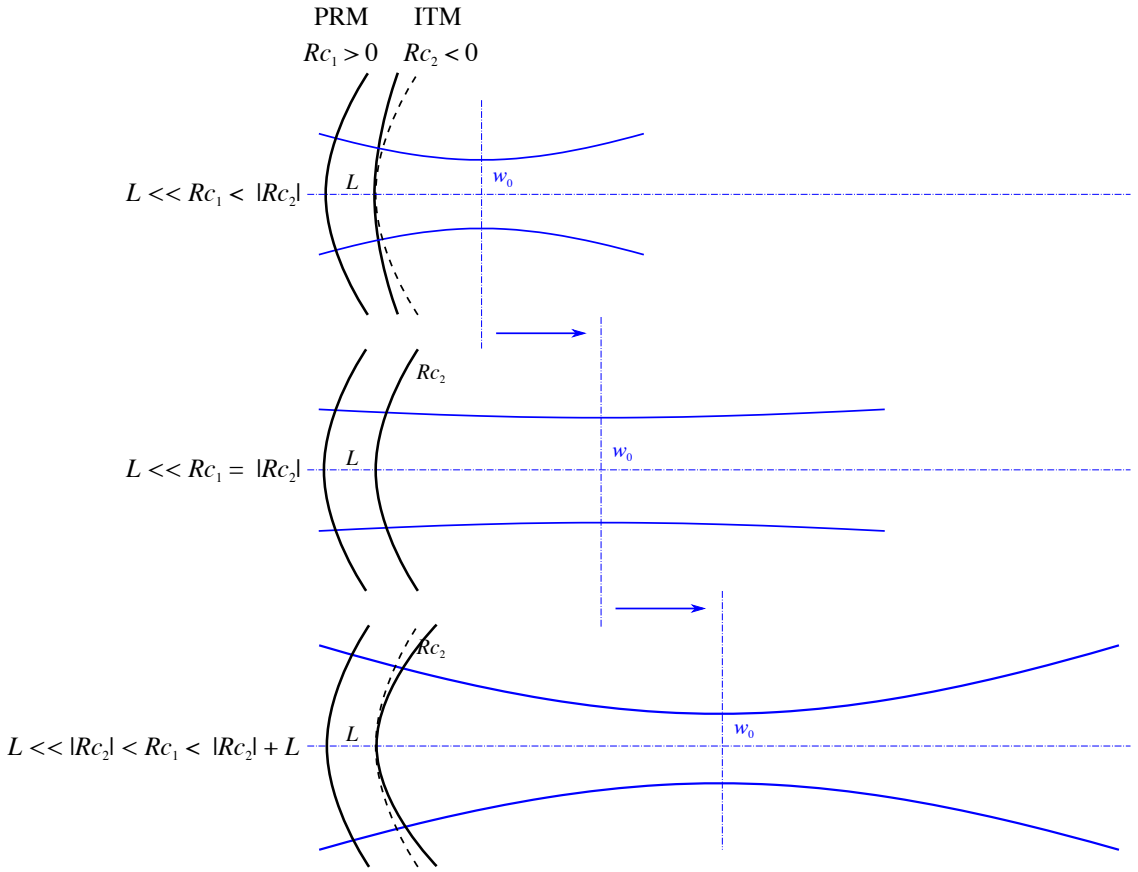

Figure 3.1: The configuration of the concave-convex power recycling cavity for Advanced Virgo. A change in Rc_2 can cause a large change in the waist position of the cavity eigenmode. From the top to the bottom, $|Rc_2|$ decreases by tens of metres. Accordingly, the cavity is pushed from a more stable configuration to the near-unstable situation. The beam waist moves approximately a thousand metres from its original position. Advanced Virgo recycling cavity is in the bottom case with $Rc_1 = 1430\,\mathrm{m}$, $|Rc_2| = 1420\,\mathrm{m}$ and $|Rc_2| + L = 1431.952$.

arm cavities with a length of 3 km, the beam waist would move approximately a thousand metres from its original position.

The power circulating in arm cavities is expected to be about 750 kW in advanced gravitational wave detectors. The change in the ROC of the input test mass due to heating by this laser power could be of order 10^2 m, resulting in significant changes in waist positions of cavity eigenmodes. In Advanced Virgo, $Rc_1 = 1430\,\mathrm{m}$ and $|Rc_2| + L = 1431.952$, corresponding to the bottom plot in Figure 3.1. The TCS mitigating this problem in Advanced Virgo are designed to maintain the ROC change of the ITM within $\pm 2\,\mathrm{m}$ from its initial value [97]. Within such control accuracies,

recycling cavities are near-unstable.

3.2.2 Arm cavity for future detectors

As discussed in Section 3.1, using a larger beam spot size on cavity mirrors is desirable in gravitational wave detectors as this reduces the effect of mirror-coating thermal noise (see Equation 1.6). This will inevitably push the cavity to near-instability, given that the maximum cavity length is limited. There are two configurations of NUCs that could provide large beam sizes on both mirrors, given a fixed cavity length: the long radius cavity (LRC) and the near-concentric cavity (NCC).

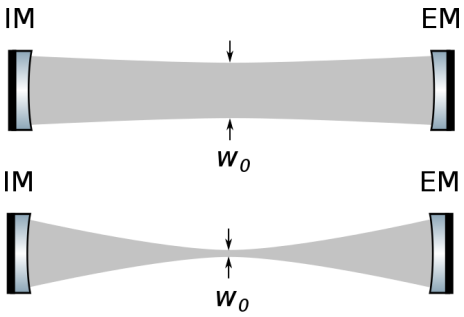

Figure 3.2: Two possible choices of NUCs to provide a large beam size with a compact design: the long-radius cavity (the top) and the concentric cavity (the bottom). In this thesis, we study the latter.

For a long radius cavity (ROC$\gg L$), the two mirrors will be almost flat, with a very slightly concave figure (see the top configuration in Figure 3.2), and the beam size will be close to the size of the beam waist. The advantage of this kind of cavity is that Gaussian beam parameters don't change too drastically with changes in ROCs and mirror longitudinal motions. However, the cavity is very sensitive to mirror tilt and even a small angular misalignment will lead to a significant decrease in the circulating power inside the cavity. As a result, it is very difficult to align two near-flat mirrors with sufficient accuracy. Moreover, even if it were possible to perfectly align the mirrors so that the optical loss is small, to use long radius cavities for ground based gravitational wave detectors, the ROCs would have be in the range of 10^4-10^6 m which is difficult to polish at the moment [98].

The bottom configuration in Figure 3.2 represents the concentric cavity whose ROCs are very close to $L/2$. Current gravitational wave detectors use similar configurations but go further towards the stable region; for instance, Advanced LIGO detectors employ arm cavities with total g-factors of 0.832. This sort of near-concentric cavity will form the main focus of this thesis. In Chapter 4, I present a tabletop experiment which aims to investigate the challenges involved in using this type of cavity when it is close to the edge of stability. Rather than constructing a near-concentric cavity, though, we use a different but related cavity configuration, the plane-concave cavity (PCC), which can be thought of as just half of the near-concentric cavity. This is discussed in more detail in chapter 4.

Requirements on ROC accuracy

The near-concentric cavity requires a precise control of the ROCs. As the cavity total g-factor is very close to 1, a small deviation of ROC (e.g. due to thermal deformations) could drive the cavity into the unstable region. For a symmetric cavity with $R_{c1} = R_{c2} = R_c$, we have $g = g_1 = g_2 = 1 - L/R_c$, and so the total g-factor for the cavity equals

$$g_c = g^2 = \left(1 - \frac{L}{R_c}\right)^2, \tag{3.1}$$

We can find the deviation in the ROC required to make the g-factor equal to 1 (edge of stability) as follows:

$$1 = \left(1 - \frac{L}{R_c + \Delta R_c}\right)^2. \tag{3.2}$$

With equation 3.1 and 3.2, the maximum deviation of ROC allowed is

$$\eta = \frac{|\Delta R_c|}{R_c} = \frac{1 - \sqrt{g_c}}{2}. \tag{3.3}$$

For a typical total g-factor value of 0.998 (used in the AEI (Albert Einstein Institute) 10 m prototype arm cavities, see Appendix A), the maximum deviation of ROC allowed is $\eta = 0.05\%$. This value corresponds to a meter change in the ROC for a

typical value around 2 km for Advanced LIGO detectors, which is beyond the control accuracy applied by the current thermal compensation system.

Beam spot size change

In the following chapters we present an experimental investigation into the behaviour of a cavity with different values of the g-factor, including values closer to the unstable region than can be measured in the NUCs used in current gravitational wave detectors. In a practical setup, replacing mirrors with different ROCs is much more time-consuming and expensive than changing the distance between the two mirrors. For a concentric cavity, we can easily adjust the cavity length to change the stability, and observe beam parameter changes as a function of cavity length, and hence of the g-factor. Using the Gaussian beam equation, we can derive the equations for the beam waist and beam spot size on the mirrors for a symmetric near-concentric cavity:

$$w_0 = \sqrt{\frac{\lambda R_c}{2\pi}\sqrt{1-g_c}} \tag{3.4}$$

and

$$w = \sqrt{\frac{\lambda R_c}{\pi}\sqrt{\frac{1+\sqrt{g_c}}{1-\sqrt{g_c}}}} \tag{3.5}$$

with w_0 the beam waist radius, and w the beam spot radius on the mirrors.

Beam spot sizes on the end mirrors in near-concentric cavities increase dramatically as the total g-factor tends to 1 (see Figure 3.3). Its eigenmode also has a thinner beam waist than that of a more stable cavity. This is shown in Figure 3.3b. The large beam sizes on mirrors in the near-unstable region are desirable for reducing mirror coating thermal noise. But a small displacement of the cavity mirror will result in a significant change in the beam profile and can even drive the cavity out of stable region.

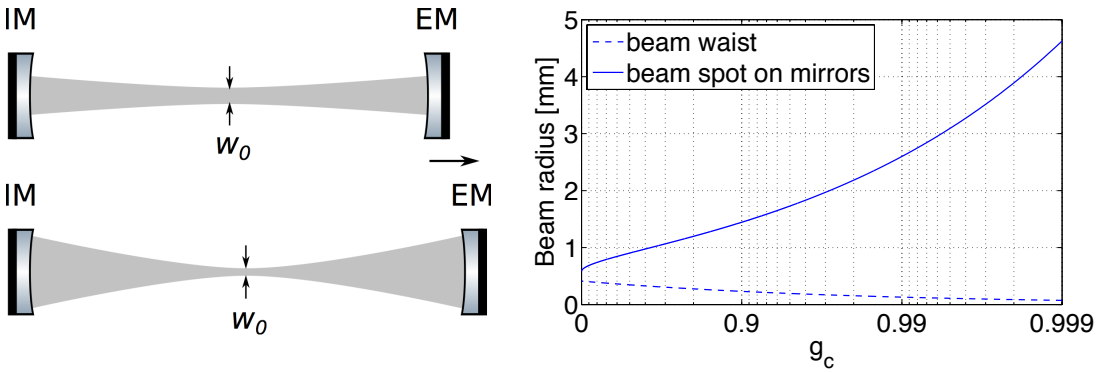

(a) Pushing the cavity to near instability (b) Beam radius as a function of total g-factors

Figure 3.3: The change of parameters of a certain Gaussian beam mode matched to the cavity when g_c varies from 0 to 1 by increasing cavity length. (a) shows the shape variation of the beam in a near-concentric cavity, with the less stable cavity (lower figure) having a thinner waist but larger beam size on mirrors. (b) shows the beam radius as a function of the total g-factor of a cavity with the mirror curvatures of 1 m and a cavity length close to 2 m. The beam size will increase significantly while the beam waist decrease dramatically as g_c tends to 1.

3.3 Mode behaviours

3.3.1 Gaussian modes

Gaussian modes are solutions of the paraxial wave equation, which can be used to describe the transverse beam geometry for a given frequency component as a sum of different spatial modes [56]. Current gravitational wave detectors use Gaussian beams (fundamental mode, or zero-order mode) as their input beams. The non-zero-order modes are called higher-order modes (HOMs). There are different basis sets for HOMs with different symmetry properties. Two of the most practically important bases are the Laguerre-Gauss modes, which exhibit rotational symmetry about the optical axis, and Hermite-Gauss modes, which exhibit rectangular symmetry in the x- and y-planes, *i.e.* in two orthogonal planes containing the optical axis.

The electric field for a single frequency component at one moment in time (t = 0)

can be expanded as [56]:

$$E(x,y,z) = e^{-ikz}\sum_{n,m} a_{nm}u_{nm}(x,y,z), \tag{3.6}$$

where a_{nm} are complex amplitude factors and u_{nm} are the appropriate special functions describing the spatial properties of the beam. For Hermite-Gauss modes, we have:

$$\begin{aligned} u_{nm}(x,y,z) =& (2^{n+m-1}n!m!\pi)^{-1/2}\frac{1}{w(z)}e^{i(n+m+1)\Psi(z)} \\ & \cdot H_n(\frac{\sqrt{2}x}{w(z)})H_m(\frac{\sqrt{2}y}{w(z)})e^{-i\frac{k(x^2+y^2)}{2R_c(z)}-\frac{x^2+y^2}{w^2(z)}}, \end{aligned} \tag{3.7}$$

where $H_n(x)$ is the Hermite polynomial of order n. In order to see the change in phase of a Hermite-Gauss mode of a given orderr, compared to a plane-wave, we write the equation 3.6 in the following form:

$$E_{nm}(x,y,z) = A_{nm}e^{-i\frac{k(x^2+y^2)}{2R_c(z)}-\frac{x^2+y^2}{w^2(z)}}e^{i(-kz+(n+m+1)\Psi)}, \tag{3.8}$$

where A_{nm} is the complex amplitude of this mode. The middle exponential term shows the phase distribution in x-y plane and the last exponential term shows the phase lag along z-axis.

3.3.2 Gouy phase

In Equation 3.8, we can see there is an extra phase shift along the z-axis of $(n + m + 1)\Psi(z)$, called the *Gouy phase*, which is equal to

$$\Psi(z) = \arctan\frac{z-z_0}{z_R} \quad \text{with} \quad z_R = \frac{\pi w_0^2}{\lambda}. \tag{3.9}$$

z_R is called the Rayleigh range.

The Gouy phase is an additional phase lag between each order HOM and the zero-order fundamental mode, which results in different conditions of resonance for each

order mode in a cavity. The separation of these resonances is determined by the round-trip accumulated Gouy phase of that cavity. Figure 3.4 shows the Gouy phase of a Gaussian beam. The zero-crossing point is the position of the beam waist. The Gouy phase changes from $-\pi/2$ to $\pi/2$ as z increases from $-\infty$ to $+\infty$. For the near-unstable conCave-conVex Cavity (CVC), the beam waist of its eigenmode is located at the same side of the two mirrors and its *round-trip accumulated Gouy phase* is:

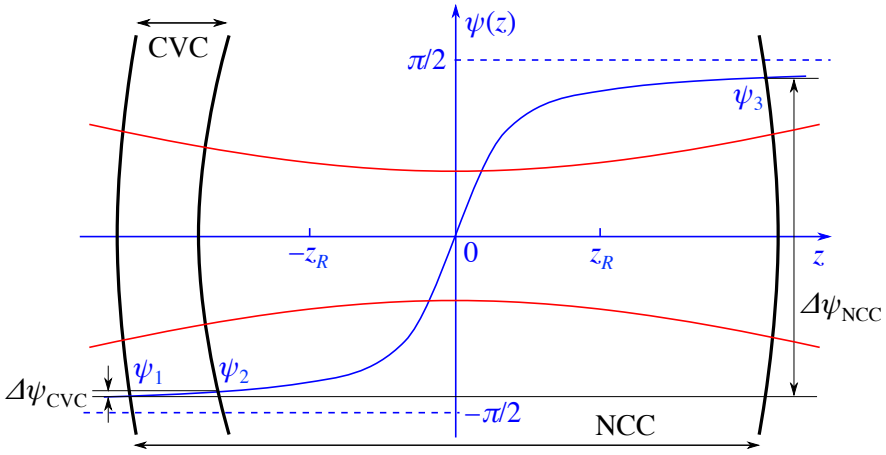

Figure 3.4: One-way Gouy phase difference in NUCs. In the near-unstable conCave-conVex Cavity (CVC), the beam waist of its eigenmode is located at the same side of the two mirrors and its round-trip accumulated Gouy phase is close to zero. In the near-concentric cavity (NCC), its waist is located between the two mirrors, and the round-trip accumulated Gouy phase is close to 2π.

$$2\Delta\Psi_{\mathrm{CVC}} = 2|\Psi_1 - \Psi_2| \to 0.$$

For the near-concentric cavity (NCC), its waist is located between the two mirrors, so the round-trip accumulated Gouy phase is:

$$2\Delta\Psi_{\mathrm{NCC}} = 2|\Psi_1 - \Psi_3| \to 2\pi.$$

In both of these cases, as the Gouy Phase tends to either 0 or 2π, there will be the problem that resonances of higher-order modes will become close to that of the fundamental mode. This is referred to as 'Mode Bunching', which we will discuss in the next section.

3.3.3 Modes bunching

In real interferometers, the fundamental mode can be coupled to higher-order modes through a number of mechanisms. Firstly, when the mirror size to spot size ratio is not large enough because of the limited practical mirror size, diffraction would always transform one order mode to the other. Secondly, practical mirrors have imperfections, such as figure errors, distortions and surface roughness, coming from manufacturing limits and thermal effects. These can also couple the fundamental mode to higher-order modes. Thirdly, even for perfect mirrors, mode mismatch and cavity misalignment would produce some higher order mode content in the cavity (introduced in detail in Section 4.4).

The resonance condition is determined by the frequency of the laser and the cavity length. The optical cavity acts as a filter where one or more modes resonating inside will be transmitted, while other modes with different frequencies are anti-resonant and are reflected. Cavities in gravitational wave detectors are usually designed to be in the stable region, with Gouy phases selected to keep higher-order modes far away from the resonance of the fundamental mode. In this case, the fundamental mode is the only resonant frequency component in the cavity. All other higher-order modes are suppressed by the cavity response and are reflected back.

One can make different modes resonate in the cavity, either by tuning the cavity length over length scales of order of the laser wavelength, or by adjusting the laser frequency. Figure 3.5 presents a cavity scan simulation where resonant conditions for each order mode are shown. The x-axis is the mirror tuning in phase corresponding to the microscopic displacement of that mirror:

$$\phi = \frac{2\pi}{\lambda} d. \tag{3.10}$$

According to this relationship, a mirror tuning phase of 180° or π corresponds to a displacement of $\lambda/2$ of the mirror, which is the FSR of the cavity. Peaks represent resonances of these modes. In a more stable cavity, higher-order modes are far

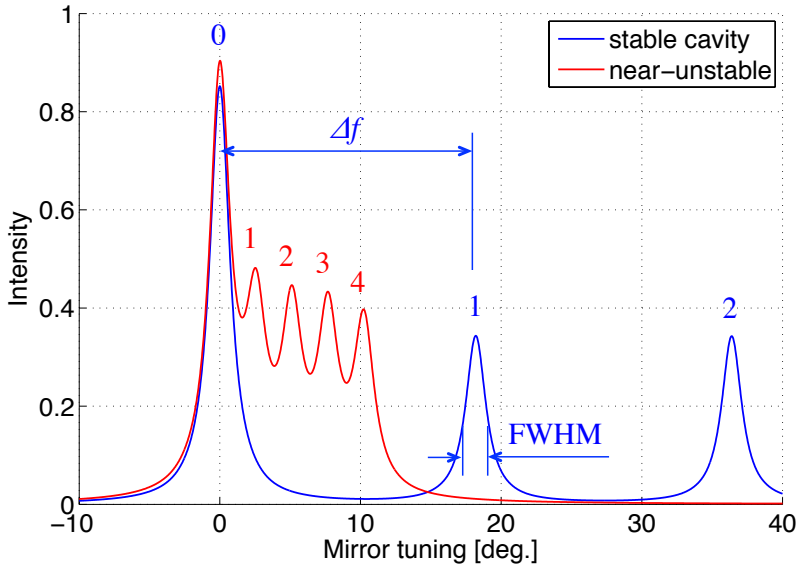

Figure 3.5: The intensity of light transmitted from the cavity when tuning the microscopic position of one cavity mirror. A mirror tuning of 180° corresponds to a mirror displacement of $\pi\lambda$. This figure compares the Gaussian mode separation in two cases: A stable cavity, with a g-factor of 0.9 and a near-unstable one, with g-factor 0.998. More specifically, this figure shows a simulated cavity scan of a near-unstable concave-convex cavity whose one way accumulated Gouy phase $\Delta\Psi$ is close to zero. The maximum order of higher-order modes scanned is 4. The number above each peak in the plot is the order of that mode.

away from resonating together with the fundamental mode (the blue curve). The frequency separation between each order mode and the selectivity of the cavity allow us to extract stable control signals to operate the interferometer, as well as ensuring that the light resonant in the cavity is of a single mode, which can be efficiently extracted to produce the gravitational wave signal. However, as the cavity becomes near-unstable, Gaussian modes bunch together and overlap with one another (the red curve). The resonance separation (described in phase) between each order mode is determined by the *one-way accumulated Gouy phase* of the cavity

$$\Delta\phi = \Delta\Psi^{mn} = (m+n)|\Psi_1 - \Psi_2|, \tag{3.11}$$

where $\Delta\Psi^{mn}$ is the one-way accumulated Gouy phase between two Gaussian modes with orders of m and n. If m and n are not specified, the $\Delta\Psi$ is the one-way Gouy

phase lag between two contiguous modes (where $m + n = 1$). Ψ_1 and Ψ_2 are the Gouy phases at the location of the two end mirrors of the cavity. By calculating the frequency change that would be required to counteract this phase shift, the frequency separation of two contiguous order modes can be derived as

$$\Delta f = \mathrm{FSR}\frac{\Delta\Psi}{\pi}. \tag{3.12}$$

The cavity scan simulation shown in Figure 3.5 corresponds to a near-unstable concave-convex cavity in which the one-way accumulated Gouy phase $\Delta\Psi_{\mathrm{CVC}}$ is close to zero. Resonances of higher-order modes appear on the right-hand side of the fundamental mode. For the near-concentric cavity, however, whose $\Delta\Psi_{\mathrm{NCC}}$ is close to π, the frequency separation between two contiguous order modes Δf is close to the free spectral range of the cavity. In this case, resonances of higher-order modes are close to those of fundamental modes in 'next generations'. For example, the resonance of the first order mode is close to the 'next' resonance of the fundamental mode; the resonance of the second order mode is close to the 'next but one' resonance of the fundamental mode. Resonant peaks of higher-order modes appear slightly to the left of the fundamental mode (not shown here but Figure 3.6 indicates this feature).

We define the mode separation frequency MSF^{mn} as the *shortest* frequency separation of resonances between two Gaussian modes. The m and n represent the order of the two modes. Without specifying m and n, the MSF means the frequency separation between two contiguous modes (e.g. the first order mode and the fundamental mode).

$$\mathrm{MSF} = \begin{cases} \Delta f, & \Delta f \leqslant \mathrm{FSR}/2, \\ \mathrm{FSR} - \Delta f, & \Delta f > \mathrm{FSR}/2. \end{cases} \tag{3.13}$$

In the near-concentric cavity, according to Equation 3.12 and Equation 3.13, we have

$$\mathrm{MSF}_{\mathrm{NCC}} = \mathrm{FSR}\left(1 - \frac{\Delta\Psi_{\mathrm{NCC}}}{\pi}\right). \tag{3.14}$$

For a symmetric concentric cavity, according to the cavity eigenfrequency equations

(Equation 3.4 and Equation 3.9), we can derive the one-way accumulated Gouy phase as a function of the cavity g-factor

$$\begin{aligned}\Delta\Psi_{\mathrm{NCC}} &= |\Psi_1 - \Psi_2| = \arctan\frac{L/2}{z_R} - \arctan\frac{-L/2}{z_R} \\ &= \pi - \arccos\sqrt{g_c}.\end{aligned} \tag{3.15}$$

Figure 3.6 depicts behaviour of resonances of each order mode when the near-concentric cavity is pushed to the stability boundary with cavity g-factor close to 1.

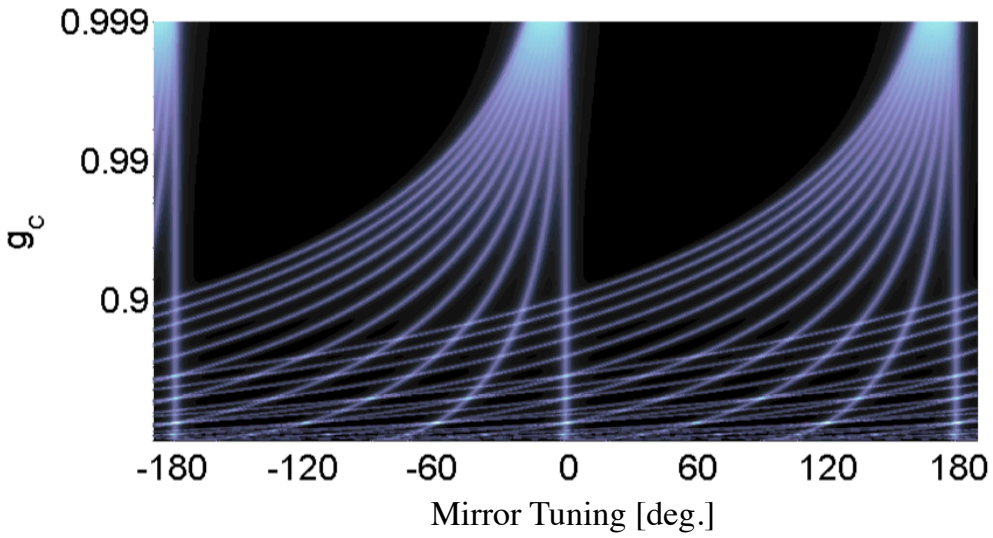

Figure 3.6: This figure depicts changed in resonance separations of Gaussian modes in a cavity as the cavity stability is varied. The bright lines show the position where Gaussian modes are resonant [99]. The $N \cdot 180°$ phase tuning positions in the x-axis are points where the fundamental mode is resonant (where N is an integer). Resonances of all of these modes bunch together when the cavity is pushed towards the edge of stability (where $g_c \to 1$). The maximum order of higher-order modes used is 10.

The mode bunching results in a significant increase in degeneracy of the fundamental mode. Higher-order modes introduced by mirror imperfections or misalignments are able to resonate, alongside the fundamental mode, especially the 1st order and the 2nd order mode, which are closest in frequency to the fundamental mode. This can cause a number of problems in the interferometer.

3.3.4 Mode separation factor

In order to quantify the resonance separation between each order mode independent of widths of the resonance peaks (shown in Figure 3.5), we define the *separation factor*, which is equal to

$$S^{mn} = \frac{\mathrm{MSF}^{mn}}{\mathrm{FWHM}}, \tag{3.16}$$

where MSF is defined in Section 3.3.3, and FWHM is the *full width at half maximum*, also called the *linewidth*, of the cavity. If m and n are not specified, the S means the separation factor between two contiguous modes. A large separation factor means there is less possibility of the two Gaussian modes interacting with each other. Using the fact that the ratio of the free spectral range and FWHM is the definition of *finesse* of the cavity $\mathscr{F}$ and using Equation 3.12 and Equation 3.13, then the separation factor can be written as

$$S = \begin{cases} \dfrac{\Delta\Psi}{\pi}\mathscr{F}, & \Delta f \leqslant \dfrac{\mathrm{FSR}}{2} \text{ (e.g. for concave-convex cavity)}, \\ \left(1 - \dfrac{\Delta\Psi}{\pi}\right)\mathscr{F}, & \Delta f > \dfrac{\mathrm{FSR}}{2} \text{ (e.g. for near-concentric cavity)}, \end{cases} \tag{3.17}$$

which shows that, in either case, the separation factor is proportional to the cavity finesse.

Current ground based gravitational wave detectors use near-concentric cavity configurations for their arm cavities. More specifically, according to Equation 3.15, the separation factor of the near-concentric cavity can be written as

$$S_{\mathrm{NCC}} = \frac{\mathscr{F}}{\pi} \arccos\sqrt{g_c}. \tag{3.18}$$

Cavity g-factors and mode separation factors of their arm cavities in Advanced LIGO (aLIGO), Advanced Virgo (aVirgo), Einstein Telescope (ET) and the AEI 10 m prototype are summarised in Table 3.1. The mode separation factors are all above 50 apart from the AEI 10 m prototype with $S \approx 10$ when pushed to its designed maximum stability. Figure 3.7 shows the separation factor as a function of

cavity stability in these different interferometers with different arm cavity finesse values. Circle markers represent their current (designed) cavity g-factors and mode separation factors. The tabletop setup we have built in Birmingham will be introduced in detail in Chapter 4.

Table 3.1: Cavity g-factors and mode separation factors of current ground based gravitational wave detectors.

Detectors	ROC [m]		Length [m]	Finesse	g_c	S
	ITM	ETM				
aLIGO [3]	1934	2245	3994.5	446	0.830	60.3
aVirgo [13]	1420	1683	3000	443	0.871	51.8
ET-HF [18]	5690	5690	10000	880	0.574	199.2
ET-LF [18]	5580	5580	10000	880	0.627	184.0
ET-push [100]	5070	5070	10000	880	0.946	65.7
AEI10m [101]	5.7	5.7	10.8	675	0.800	99.6
	5.7	5.7	11.3952	675	0.998	9.6

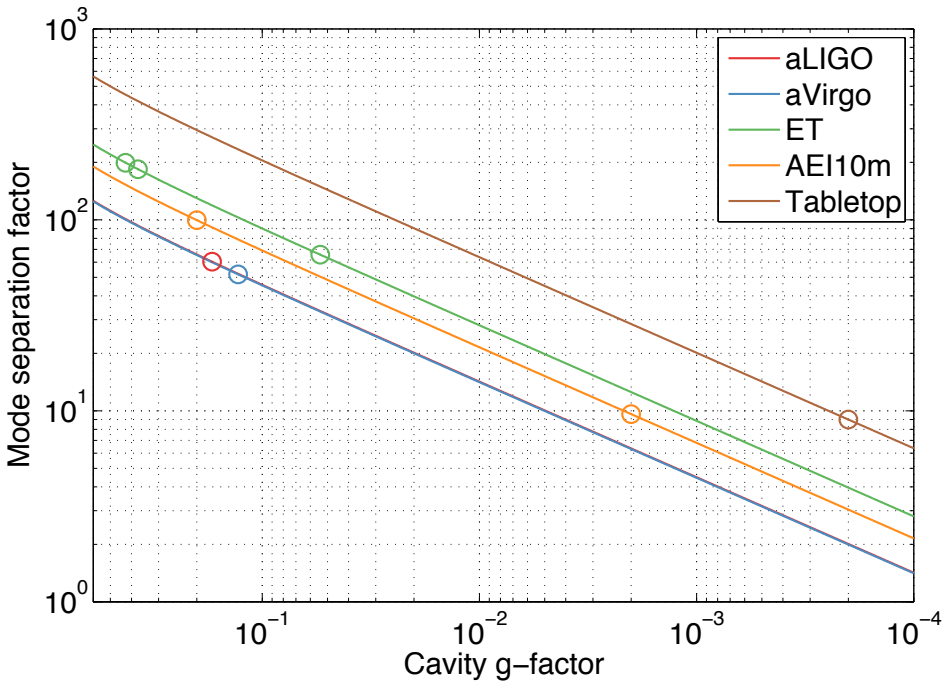

Figure 3.7: The separation factor as a function of total g-factor with different cavity finesse values in current interferometers. The tabletop cavity discussed in Chapter 4 has a high finesse about 2000.

The separation factor can be a useful parameter that gives us a good idea of the upper limit of the g-factor of the cavity. The lower the separation factor, the greater the

mode degeneracy. In practice, the separation factor should be significantly greater than 1, so that there is some tolerance for mirror imperfections and for misalignment. As there is a trade off between cavity g-factor and the finesse, high finesse is usually necessary in a near-unstable cavity in order to maintain the separation factor.

3.4 Angular instabilities

There are some other factors that can limit the maximum achievable cavity stability in advanced gravitational wave interferometers, such as the angular instability induced by radiation pressure effects [102]. The mirror angular motions cause the cavity axis to deviate from the centre. Then the radiation pressure forces from high power beams stored in arm cavities exert torque upon suspended mirrors, which makes the control of the cavity more difficult. It has been studied that the torsional stiffness is totally determined by the geometric stability of the cavity, specifically by g-factors of the two mirrors g_2 and g_2 [102]. A detailed modelling work of radiation pressure torques in gravitational wave detectors has been carried out in [103, 104]. This effect will be further investigated experimentally in the AEI 10 m prototype using suspended mirrors when the arm cavities are pushed to the edge of stability. In our tabletop experiment introduced in the following chapters, we won't take this effect into account.

3.5 Conclusion

In this chapter, we have introduced the application and configuration of NUCs in gravitational wave detectors. For current detectors, they are used as recycling cavities in Advanced Virgo due to its simplicity. For future detectors, NUCs are proposed to be used as arm cavities due to their larger beam spot which can provide a reliable reduction in coating thermal noise.

Mode behaviours have been studied when the cavity is pushed from stable regions to unstable regions. In stable regions, resonances of Gaussian modes are well isolated. But in the near-unstable region, they bunch together causing mode degeneracies. We have defined the mode separation factor which can tell the relationship between mode degeneracy and the cavity stability. The separation factor can be a useful parameter that gives us an idea of the upper limit of the g-factor of the cavity. Current detectors employ arm cavities with a MSF around 10^2. The AEI 10 m prototype interferometer is going to push the MSF to the level of 10^1. In the next chapter, I will design and set up a tabletop cavity with a targeting MSF of 10^1.

Chapter 4

Setup and characterisation of the near-unstable cavity

As discussed in the previous chapter, near-unstable cavities could allow a larger spot size to be used in GW detectors, reducing the mirror coating thermal noise. This is expected to be experimentally demonstrated in the Albert Einstein Institute (AEI) 10 m prototype interferometer, an ultra-low displacement noise facility [105, 106, 107]. The primary goal of this prototype interferometer is to reach standard quantum limit sensitivity as thermal noise reduced, in order to conduct a variety of experiments in macroscopic quantum mechanics. A number of secondary goals must be achieved in order to reach this point. One of them is a reduction of mirror coating thermal noise, which would involve using a NUC; this is the first experiment to study in detail the practical aspects of using NUCs in a GW detector. The experiment described in this chapter is a much simpler tabletop experiment, providing a test-bed for a number of relatively quick and easy measurements of important aspects of the behaviour of a near-unstable cavity. This experiment could give us a greater understanding of whether NUCs are compatible with ground-base gravitational wave detectors, and of how close one can go towards cavity instability. The results of this experiment, and the comparison between these measurements and the results of simulations, also provide a reference and for the simulation and experimental

studies at the AEI prototype, as well as for the design or optimisation for current and future gravitational wave detectors.

4.1 Optical design of the setup

We have built an optical setup which allows us to study the behaviour of a near-unstable cavity with different stabilities. In this section, we introduce the design and parameters of the optical layout of this tabletop experiement, and we describe the optical and electronic components used to control and characterise the cavity.

4.1.1 Configuration: a plane-concave cavity

The AEI 10 m prototype uses symmetric cavities in its two arms. Large spot sizes on both mirrors in each cavity can be achieved when the cavities are pushed to the boundary of stability. This contributes to a reduction of the thermal noise in this instrument so that it can perform quantum level experiments in the future. The mode matching between the input beam and the symmetric cavity is very important, especially when the cavity has a tunable stability. The strategy to do this has been carefully designed in the prototype, and involves using collimated input beams, rather than converging beams. This follows a detailed analysis of the interferometer's operability and sensitivity [101].

The aim of our tabletop experiment is to investigate the behaviour of NUCs using commercially available equipment and established techniques that can be quickly applied. For considerations of simplicity of mode matching, we decided to set up a plane-concave cavity (PCC), also called a hemispherical cavity, instead of the symmetric near-concentric cavity (NCC). A plane-concave cavity has exactly same eigenmodes as a near-concentric cavity with twice the cavity length, shown in Figure 4.1. With a shorter cavity length, the plane-concave cavity is easier to control. For example, the length stabilisation is easier, as the air flow between two cavity mir-

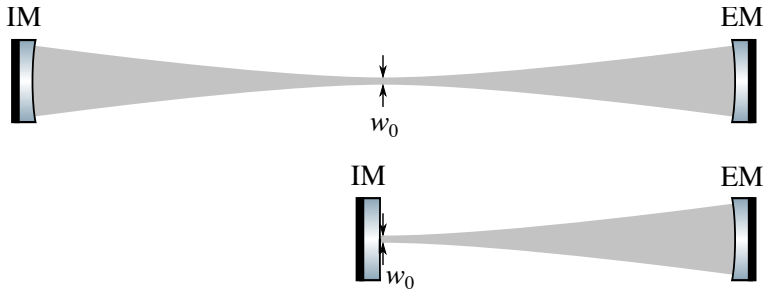

Figure 4.1: Comparison of a plane-concave cavity and a symmetric near-concentric cavity. The beam waist lies in the centre of the near-concentric cavity (the top). If we put a flat mirror just at the position of the beam waist, this forms the plane-concave cavity with half cavity length (the bottom). In this case, the plane-concave cavity has exactly same eigenmodes as the near-concentric cavity.

rors is less. There are some other important differences between the plane-concave cavity and the near-concentric cavity: Firstly, the plane-concave cavity has a different stability (g-factor) from the near-concentric cavity. Secondly, having half the cavity length, means that the plane-concave cavity has half the one-way accumulated Gouy phase compared to an equivalent near-concentric cavity.

The stability of plane-concave cavity

Both the plane-concave cavity and the near-concentric cavity can be pushed to the stability boundary by increasing the cavity length. However, they have different configurations and their g-factors go in opposite directions. The geometric stability of a cavity is defined in Equation 1.7. ROCs of both mirrors in the near-concentric cavity are close to $L/2$. According to Equation 1.8, the g-factor of the cavity is

$$g_c \to 1 \quad \text{with} \quad g_1 \to -1,\, g_2 \to -1 \quad \text{(for near-concentric cavity)}. \tag{4.1}$$

For the near-unstable plane-concave cavity, as the ROC of the flat mirror is infinity (plane), the cavity g-factor becomes

$$g_c \to 0 \quad \text{with} \quad \begin{cases} g_1 \to 0,\, g_2 = 1 \\ g_1 \to 1,\, g_2 = 0 \end{cases} \quad \text{(for plane-concave cavity)} \tag{4.2}$$

From the stability diagram shown in Figure 1.5, we can see that the near-concentric cavity is near to the point $(-1, -1)$. Near-unstable plane-concave cavities can lie anywhere close to one axis (where one of the g-factors goes to zero), though not at the origin; having both g-factors tends to zero would produce a confocal cavity. Even though the plane-concave cavity and the near-concentric cavity have different g-factor values, their distances from 0 or 1 respectively reflect how close they are to the stability boundary. A comparison of g-factors with some typical values between the plane-concave cavity and the near-concentric cavity can be found in Table 4.1 in Section 4.1.2.

Higher-order modes bunching

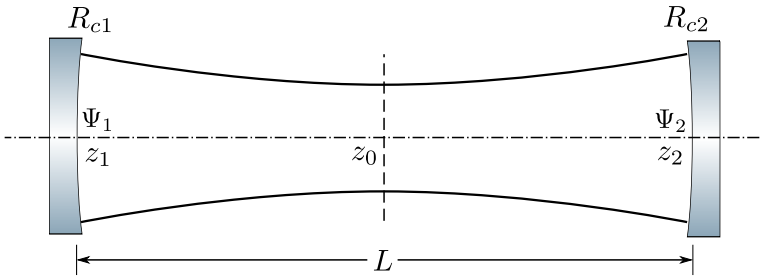

Figure 4.2: The Gaussian beam in a stable cavity.

The higher-order mode separation frequency, given by Equation 3.12 is proportional to the one-way accumulated Gouy phase $\Delta\Psi$. For a symmetric near-concentric cavity (see Figure 4.2), the accumulated one-way Gouy phase, for a mode of order N, is

$$\begin{aligned}\Delta\Psi_{\mathrm{NCC}} &= \Psi_2 - \Psi_1 \\ &= \arctan\frac{L_{\mathrm{NCC}}/2}{z_R} - \arctan\frac{-L_{\mathrm{NCC}}/2}{z_R} = 2\arctan\frac{L_{\mathrm{PCC}}}{z_R},\end{aligned} \tag{4.3}$$

where z_R is the *Rayleigh range*. For a plane-concave cavity with the same beam waist, the one-way Gouy phase lag is

$$\Delta\Psi_{\mathrm{PCC}} = \Psi_2 - \Psi_1 = \arctan\frac{L_{\mathrm{PCC}}}{z_R} - 0 = \arctan\frac{L_{\mathrm{PCC}}}{z_R}. \tag{4.4}$$

In the near-unstable region,

$$\arctan \frac{L_{\mathrm{PCC}}}{z_R} \to \pi/2.$$

So $\Delta\Psi_{\mathrm{NCC}} \to \pi$ but $\Delta\Psi_{\mathrm{PCC}} \to \pi/2$. Correspondingly, the mode separation frequencies between two contiguous order modes for the near-concentric cavity and the plane-concave cavity are $\Delta f_{\mathrm{NCC}} \to \mathrm{FSR}$ and $\Delta f_{\mathrm{PCC}} \to \mathrm{FSR}/2$, respectively. This means that all the higher-order modes in the near-concentric cavity will become coresonant with the fundamental mode (which we have discussed in Section 3.3.3), whereas in the case of the plane-concave cavity, only even order higher-order modes are close to the fundamental mode; the higher-order modes with odd order are all anti-resonant. Figure 4.3 shows the resonance differences of Gaussian modes between the plane-concave cavity and an equivalent near-concentric cavity that has the same eigenmodes. The first order mode is often used to extract alignment signals (described in detail in Section 4.4), while the second order mode is often used as a reference signal for mode matching. The modes bunching in the near-concentric cavity results in both of these modes being co-resonant in the cavity, potentially leading to cross-talk between alignment control and mode matching signals. The control signal in the plane-concave cavity will be much cleaner as the first order mode is isolated from the fundamental mode.

Mode separation factor

The mode separation factor of the near-concentric cavity is given by Equation 3.17,

$$S_{\mathrm{NCC}} = \left(1 - \frac{\Delta\Psi_{\mathrm{NCC}}}{\pi}\right)\mathscr{F} \tag{4.5}$$

In the plane-concave cavity, the frequency separation between the first order mode and the fundamental mode will be close to half of the FSR. More important, is the separation between the second order mode and the fundamental mode; these will be the lowest order modes that tend towards coresonance. The one-way Gouy phase

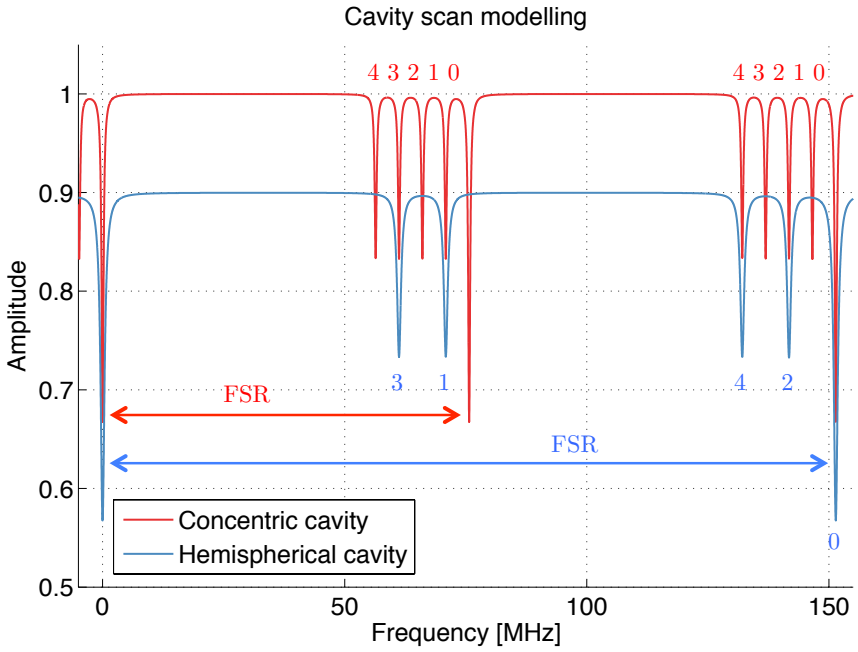

Figure 4.3: Simulated differences in free spectral range (FSR) and modes bunching between the near-concentric cavity and the hemispherical cavity (plane-concave cavity). As the cavity length of the plane-concave cavity is half of that of the near-concentric cavity, the free spectral range of the plane-concave cavity doubles. All higher-order modes in the near-concentric cavity are approaching the fundamental mode. But in the plane-concave cavity, only even order modes tend towards coresonance, while odd order modes approach anti-resonance.

lag between the second order mode and the fundamental mode is

$$\Delta\Psi^{02}_{\mathrm{PCC}} = 2\Delta\Psi_{\mathrm{PCC}} = \Delta\Psi_{\mathrm{NCC}}. \tag{4.6}$$

If the plane-concave cavity and the near-concentric cavity have same cavity finesse, we have

$$S^{02}_{\mathrm{PCC}} = S_{\mathrm{NCC}} = \frac{1}{2}S^{02}_{\mathrm{NCC}}. \tag{4.7}$$

We see that the separation factor between the second order mode and the fundamental mode in the plane-concave cavity is the same as the separation factor between the first order mode and the fundamental mode in the near-concentric cavity, but half of that between the second order mode and the fundamental mode in the near-concentric cavity.

In practical terms, this means that the difference between the plane-concave cavity and the near-concentric cavity (having same eigenmode and same finesse), is that the plane-concave cavity doesn't have signal degeneracy problems caused by modes bunching in the alignment control, but degeneracy in the signal for mode matching is more severe than for the near-concentric cavity.

4.1.2 The cavity design

The cavity we have built in Birmingham is designed to host experiments in various near-unstable conditions. Compared with the AEI 10 m prototype which has a maximum design g-factor of 0.998, we would like to push our tabletop cavity 10 times closer to the stability boundary. A high cavity finesse is necessary for us to better distinguish problems caused by geometric stability from other technical issues. We choose a finesse of approximately 2000 as a trade off between the mode separation factor and the lock feasibility of the cavity. Such a finesse should produce a mode separation factor of around 10, which is similar to that in the AEI prototype. The higher finesse will lead to stricter requirements on the cavity length stabilisation system. The cavity is formed by a flat mirror as the input mirror (IM) and a concave mirror as the end mirror (EM). The radius of curvature of the concave mirror is chosen to be 1 m due to its easy availability. This results in a cavity length of approximately 1 m according to the stability criterion.

Table 4.1 gives the design parameters of the tabletop plane-concave cavity. The cavity is initially constructed to lie in a stable region, with a g-factor of around 0.8 (see the footnote in the table), similar to that of arm cavities in Advanced LIGO and Advanced Virgo. Once the cavity is aligned and locked, and the error signals and other diagnostics are sufficiently well understood, we would like to incrementally increase the length of the cavity, such as to incrementally change the stability towards the limiting target value for the cavity g-factor in the extreme near-unstable region.

Table 4.1: Parameters of the plane-concave cavity setup.

Cavity length	0.956 m	0.993 m	0.999 m	0.9999 m
Beam waist [μm]	263.56	168.04	103.46	58.19
Beam radius (at EM) [mm]	1.26	2.01	3.27	5.82
Rayleigh range [mm]	205.10	83.37	31.61	10.00
Divergent angle [mrad]	1.29	2.02	3.27	5.82
FSR [MHz]	156.80	150.95	150.05	149.91
Finesse	2092.82	2092.82	2092.82	2092.82
FWHM [kHz]	74.92	72.13	71.70	71.63
Pole frequency [kHz]	37.46	36.06	35.85	35.82
MSF^{01} [MHz]	67.85	71.45	73.51	74.48
MSF^{02} [MHz]	21.10	8.05	3.03	0.95
S^{02}	281.6	111.6	42.3	13.3
g_c	0.044	0.007	0.001	0.0001
g_c^* [a]	0.832	0.972	0.996	0.9996

[a] g_c^* represents the g-factor of a near-concentric cavity that has the same eigenmode but twice the cavity length of the plane-concave cavity.

4.1.3 Layout of the setup

The schematic layout of the whole optical setup is shown in Figure 4.4. Two infrared lasers are used for different purposes. One is called the 'reference laser', the other, the 'probe laser'. Both lasers are diode-pumped Nd:YAG lasers with the same nominal wavelength of 1064 nm. The optical layout immediately following the laser is the same in both cases: the beam passes through a quarter-wave plate, a half-wave plate, then a polariser, a Faraday Isolator (to be described below), then another half wave plate, and another half-wave plate. This sequence of components allows the output power and polarisation to be controlled. The Faraday isolator allows the transmission of the laser beam in only one direction so that unwanted back reflections are prevented from entering into the laser cavity. This prevents back reflections leading to amplitude fluctuations and possibly even damaging the laser. The beams from the two lasers are polarised orthogonally to each other before being combined at the central non-polarising beam splitter (CNBS). The orthogonal polarisation ensures that they don't interfere. Before being combined, each of them passes through a Electro-Optic Modulator (EOM) that generates phase modulation

sidebands in radio frequencies (RF) for control purposes, such as for the frequency stabilisation and the alignment control. The probe laser is used for experimental studies of the 1 m NUC such as measuring Gaussian mode resonance conditions, and quantifying the geometric stability of the cavity. The reference laser is used to stabilise the frequency of the probe laser, as well as all the important lengths in this setup, which would otherwise experience fluctuations due to air turbulence, acoustic noise, and variations in temperature and stress in the components and the optics table. The cavity length is stabilised relative to the reference laser through Pound-Drever-Hall technique. The frequency of the probe laser is phase locked to that of the reference laser with a tunable offset. The following sections in this Chapter will introduce these subsystems.

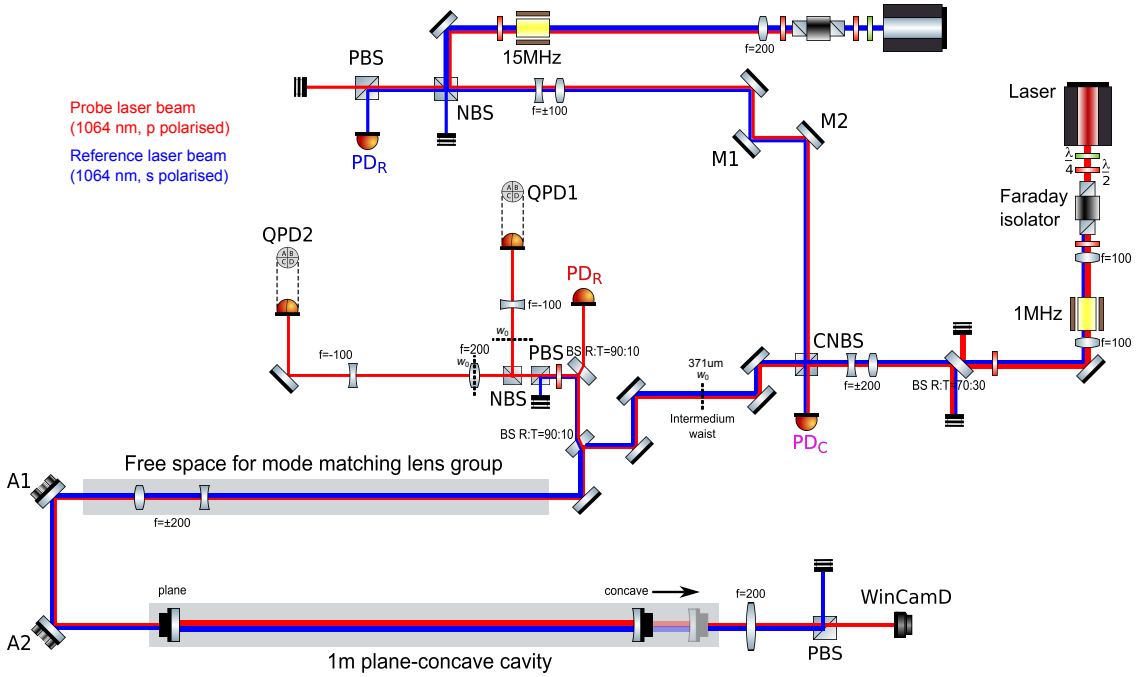

Figure 4.4: The schematic layout of the Birmingham 1 m NUC experiment setup. The red and blue lines represent beams from the probe laser and the reference laser, respectively.

4.1.4 Mode matching of the cavity

For a Fabry-Perot cavity, once the ROCs of the two end-mirrors, and the distance between them have been defined, the eigenmodes of the cavity are determined. Mode

matching refers to matching Gaussian parameters of the incoming field to those of the cavity's eigenmodes. In practical terms, there are two aspects to this: matching the waist size of the incoming beam to that of the eigenmodes, and matching the waist position of the incoming beam to the cavity's eigenmodes as well. In our tabletop setup, the length of the 1 m cavity is altered by adjusting the position of the concave end mirror, while the flat input mirror remains fixed. When the cavity configuration changes, the waist size of its eigenmodes also changes but the waist position remains fixed on the flat input mirror; this will always be the case in a hemispherical cavity.

The mode matching is usually performed by adjusting the positions of one or more lenses. In general, two lenses, with one converging and the other diverging, will suffice. These can be seen as acting as a telescope. The two lasers in our tabletop setup both have their own mode matching telescopes before combining together at the central non-polarising beam splitter (CNBS). These telescopes are used to produce a Gaussian beam with the required beam waist size and position to match the cavity modes. They ensure that beams from the two lasers have same parameters after combination, yielding a resulting beam waist of 371 μm and 25 cm after the CNBS, shown in Figure 4.4. A rigid triangular cavity is placed (not included in the figure) at the location of this intermediate waist for laser calibration purposes (introduces in Section 4.2.3), and removed after calibration.

In our mode matching scheme, we use two lenses with focal length of ± 200 mm to match the intermediate beam waist to the cavity's eigenmode. This lens group is installed on a rail in which we manually change positions of lenses according to different cavity configurations. The two lenses are carefully aligned so that the beam goes through the centre to a high precision, so that their longitudinal motions won't significantly affect the transverse position of the beam spot incident to the input mirror.

The free space for moving the lens group in principle allows the cavity stability to be varied from $g_c = 0.044$ (where $w_0 = 263.56\,\mu$m) to $g_c = 0.00004$ (where

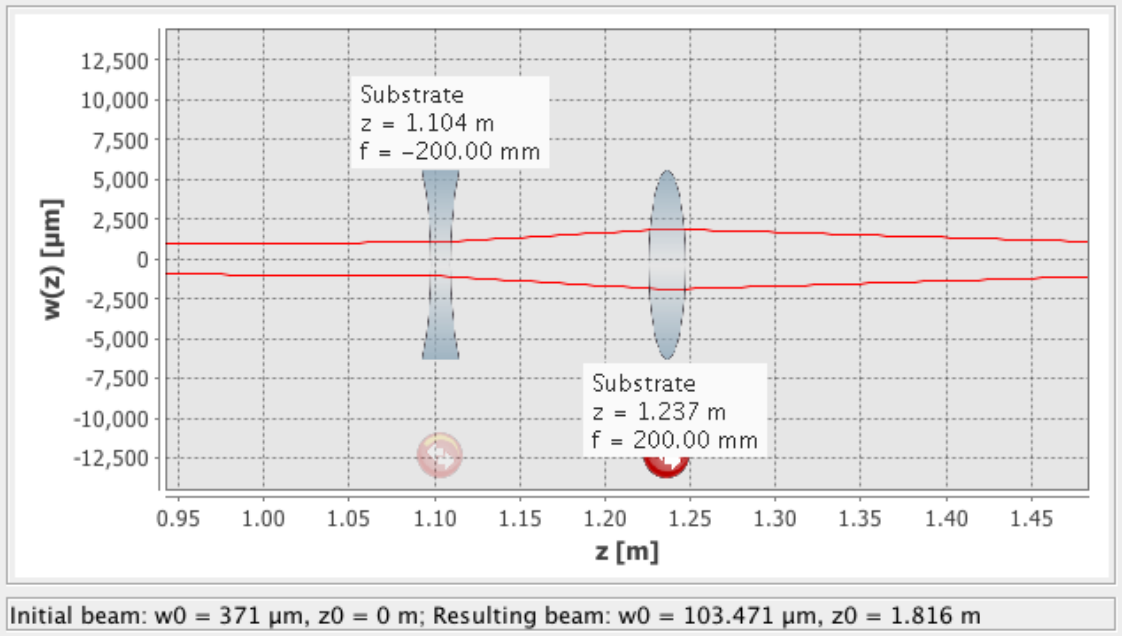

Figure 4.5: Lens group positions for $g_c = 0.001$.

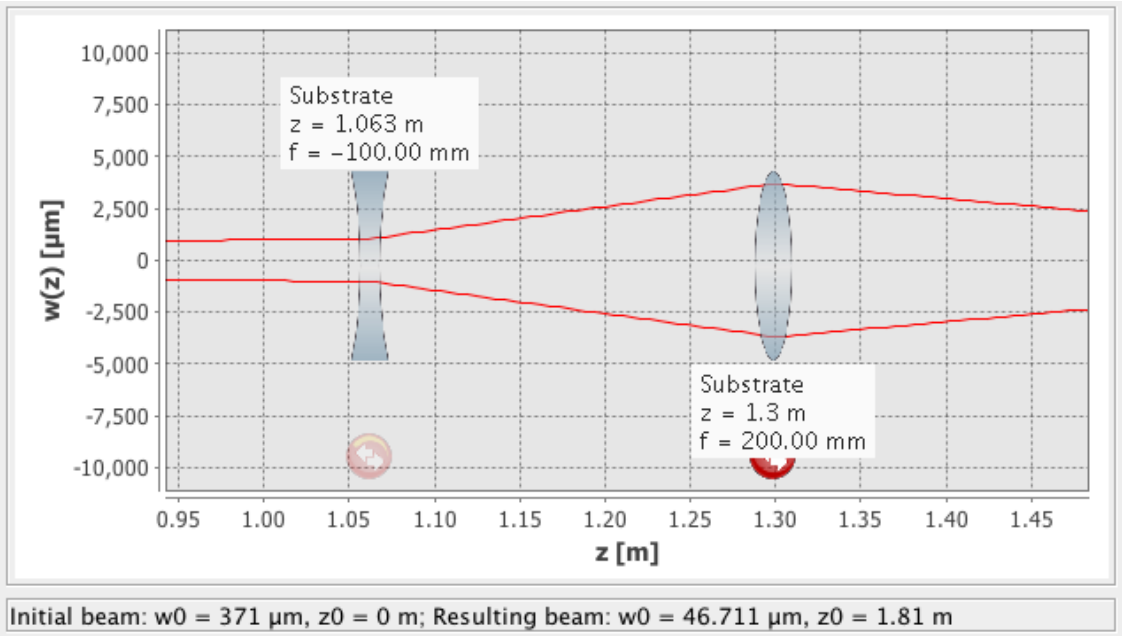

Figure 4.6: Lens group positions for $g_c = 0.00004$.

$w_0 = 46.28\,\mu$m). Figure 4.5 and Figure 4.6 give lens group positions for an intermediate stability $g_c = 0.001$ (where $w_0 = 103.46\,\mu$m) and the minimum stability $g_c = 0.00004$. These two figures are plotted by the software JamMt [108]. The x-axis is the distance between the lens and the position of the intermediate waist. Note that the -200 mm lens moves about 4 cm and the $+200$ mm lens moves about

6 cm. In the near-unstable region, a small movement of the lenses will result in a large change in beam properties.

In practice, one limiting factor for the mode matching is the limited precision to which one can measure the exact size and position of the resulting beam waist. Another is the precision to which the position of of the lenses can be controlled. In practice, one first uses the position and size of the beam waist to carry out 'coarse' mode matching, then using the cavity itself for fine tuning. As mode mismatch couples the fundamental mode to the second order mode, what we do is to minimise the resonance of second order mode as best as we can by slightly tuning positions of the two lenses around their design values. As the second order mode content will in general depend non-linearly on the lens positions, it is not easy to find their optimum positions.

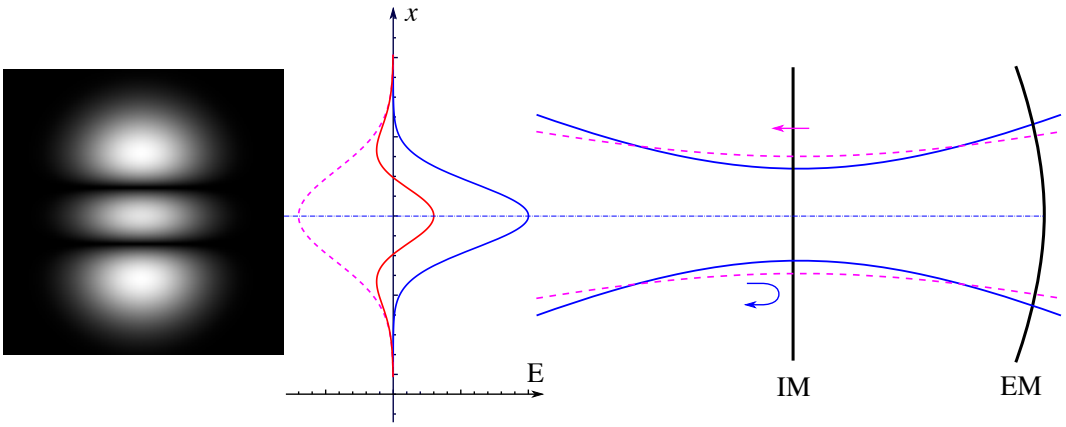

Figure 4.7: A schematic showing how waist size mismatch couples the fundamental mode to the second order mode.

Figure 4.7 illustrates how the fundamental mode is coupled to the second order mode due to mode mismatch. There are two kinds of mode mismatch: waist size mismatch and waist position mismatch. Both of them result in producing power in the second order mode if the incoming beam is purely in the fundamental mode. The plot here only shows the mechanism of waist size mismatch. The field in blue is the Gaussian beam directly reflected by the input mirror (IM). The pink field represents the transverse profile of the component of the cavity's eigenmodes which leaves the cavity through the input mirror. The total reflected beam is just the

sum of the two fields. On resonance, there is a phase shift of 180° between them; it is this condition that ensures that, in the ideal case, beams resonant in the cavity will interfere destructively at the input mirror, and so will not be reflected. In this case, due to the diffrent beam sizes, the difference of their amplitudes will produce a beam profile which in general, will contain a large component in the second order mode.

4.2 Length stabilisation of the cavity

The stabilisation of the cavity length is critically important in this experiment. The cavity will be pushed to extreme conditions where it is very sensitive to changes in its configuration. Noises introduced by air turbulence and mechanical resonances can cause a large error in our measurements. Furthermore, as we use the light field effectively as a ruler in most of our measurements, a free running laser also introduces frequency noise. Thus the cavity length and the laser frequency must be stabilised relative to one another before a precise measurement can be made.

The cavity length or laser frequency stabilisation is usually performed by the Pound-Drever-Hall technique [109, 110]. The idea behind it is that the laser frequency can be measured by the length of an optical resonator and vice versa. Many modern lasers can create continuously tunable frequencies. Given a rigid cavity, known as the *reference cavity*, the laser frequency can be measured and this measured signal is fed to the tuning port to maintain the laser frequency at its target value. Similarly, the cavity length can be measured and stabilised relative to a reference laser, by actuating on positions of cavity mirrors. The Pound-Drever-Hall technique is described in more detail in Appendix C.

The key point of the Pound-Drever-Hall technique is that it creates a measurement signal, called the *error signal*. This signal is, over some range, linear in the deviation of the cavity from resonance (see Figure C.3). By feeding back this signal to either the laser frequency or to the cavity length, it is possible to maintain the light field in

the cavity resonating at its maximum intensity. In this case, the wavelength of the laser and the length of the optical resonator are maintained relative to each other; the cavity length will be maintained at an integer multiple of the laser wavelength, though the value of this integer will not necessarily be known.

4.2.1 Optical components for the setup

A typical schematic layout of the Pound-Drever-Hall frequency stabilisation setup including all relevant optical and electronic devices is shown in Figure C.2. In the tabletop setup shown in Figure 4.4, we establish a complete Pound-Drever-Hall loop for each laser source. The loop for the reference laser is always closed, to stabilise the reference laser and the cavity. The Pound-Drever-Hall loop for the probe laser is open for most of time and only closed if it is necessary for a measurement. The frequency of the probe laser is stabilised to the reference laser by another loop, the offset phase lock loop introduced in Section 4.3. We now in the following two sections describe in more detail the important optical and electronic components used in the tabletop experiment for the Pound-Drever-Hall technique.

Lasers

Table 4.2: Manufacturer specified specifications of the Mephisto lasers.

Specification	Mephisto laser
Maximum output power	300 mW, 1200 mW
Beam quality factor	TEM_{00} $M^2 < 1.1$
Spectral Linewidth	1 kHz over 100 ms
Thermal Tuning Coefficient	-3 GHz/K
Thermal Tuning Range	30 GHz
Thermal Response Bandwidth	$\approx$ 1 Hz
PZT Tuning Coefficient [1]	1 MHz/V to 2 MHz/V
PZT Tuning Range [2]	$\approx \pm 65$ MHz
PZT Response Bandwidth	100 kHz
Frequency Stability	$\approx$ 1 MHz/min

[1, 2] These two parameters are calibrated in our experiment with a small rigid cavity introduced in Section 4.2.3.

The two lasers we use are commercial products (Mephisto 300 NE for reference laser and Mephisto 1200 NE for probe laser) from Innolight, Germany. They are both diode-pumped single frequency continuous-wave solid-state lasers, which use a monolithic Nd:YAG crystal in the Non-Planar Ring Oscillator (NPRO) configuration [111]. The device provides a tunable output frequency over 30 GHz, centred at a wavelength of 1064 nm, and has very narrow linewidth of 1 kHz over 100 ms. The two Mephisto lasers we have can deliver up to 300 mW and 1200 mW power, respectively. Their specifications are listed in Table 4.2.

The laser system itself has a control box which stabilises the temperature to a value set by the user. The thermal tuning coefficient is about -3 GHz/K. The output frequency can also be fine-tuned with an integrated Piezo-electric transducer (PZT) that changes the microscopic length of the laser cavity. The Piezo-electric transducer is usually used as a precise positioning actuator in which a piezo-electric crystal stretches according to the electric voltage applied to it. This is known as the piezoelectric effect. The maximum range of piezo devices varies from about a micron, to hundreds of microns or millimetres for stacked piezo devices. They are often used directly as linear translators, but can apply large forces, so are sometimes used in alternative configurations in which, for instance, they act to bend a plate which responds with a buckling motion. In general, a the smallest possible adjustment to position will be proportional to the range of motion, as the motion is generally close to being linear in the applied voltage; the dynamic range then depends on the voltage source. The PZT integrated in the Mephisto laser has a tuning coefficient of about 1 MHz/V and the input voltage range is ± 100 V (specified by the manufacturer).

The frequency noise is measured in [112] (see Figure 4.8) where 8 Mephisto lasers are used for the measurement. The noise shows little variation between different lasers, and is stable with time. The amplitude spectral density of the noise has a shape referred as $1/f$, noise in which the noise amplitude is inversely proportional to the frequency. The peaks between 10 kHz and 40 kHz are due to resonances of the piezoelectric element. There are also peaks between 50 Hz and 1 kHz, probably caused electronic modules, but it is unknown if these peaks come from the laser

output or the locking system for the measurements.

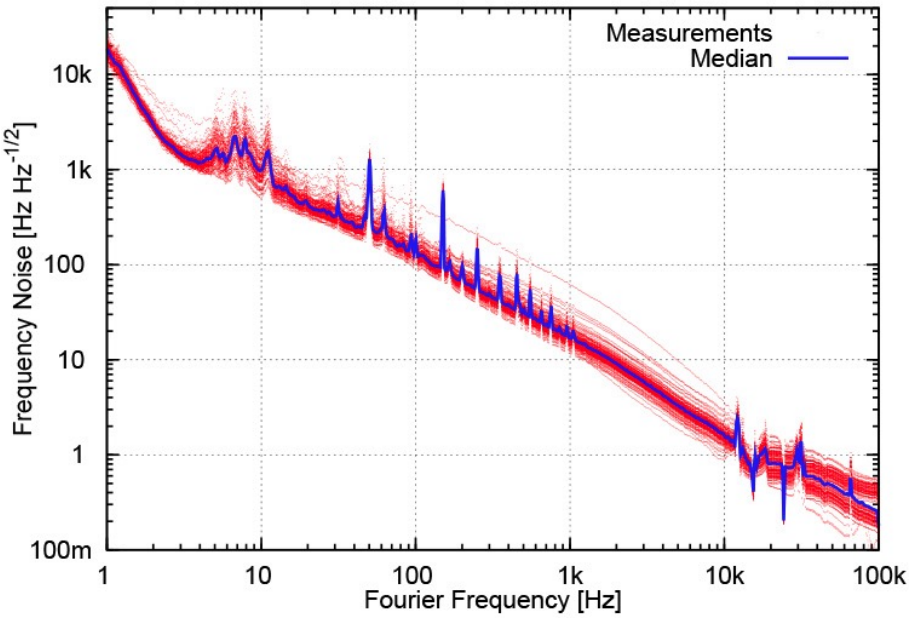

Figure 4.8: The frequency noise of the Mephisto laser measured in [112]. This picture is taken from that reference.

Waveplate

A waveplate is a plate of crystal that can change the polarisation state of light by the birefringence effect, in which polarisation components along different axes will experience different indices of refraction. A birefringent crystal will have two preferred directions in the plane perpendicular to the optical axis; one in which the refractive index is maximised, and another in which it is minimised. These are referred to as the slow axis and fast axis, respectively. The corresponding indices of refraction are called the ordinary and extraordinary indices of refraction; which of these corresponds to the fast and slow axes can vary for different crystals. Two types of commonly used waveplates are half-wave plates and quarter-wave plates. The former are usually used for rotating the polarisation direction of linearly polarised light, while the latter can change linearly polarised light into circularly polarised light. For a half-wave plate, the relative phase difference between the component of light polarised along the slow axis, and that in the fast axis, is an odd multiple of

π:

$$\frac{2\pi\Delta nL}{\lambda} = 2N\pi + \pi, \tag{4.8}$$

where Δn is the difference in index of refraction between the ordinary and extraordinary light, L is the thickness of the crystal and N is an integer corresponding to the order of the waveplate. A multi-order waveplate will usually be at least 10 times more sensitive to wavelength and temperature changes than the zero-order waveplate. The angular drift in polarisation due to thermal fluctuations in the waveplate will translate into power fluctuations if the beam subsequently passes through polarising components, such as a polarising beam splitter (PBS). In experiments requiring stable laser power, multi-order waveplates should be avoided whenever possible. A zero-order waveplate uses two kinds of birefringent crystals with roughly equal and opposite response to temperature changes, to compensate. These are usually much more expensive. In the Pound-Drever-Hall locking scheme, though the intensity fluctuation is not coupled to laser frequency or cavity length stabilisation, it does have an influence on the loop calibration (introduced in section 4.2.3). For this reason, we use only zero-order waveplates (from ThorLabs).

Faraday Isolator

The Faraday Isolator we use comes from LINOS (FI-1060-5SI). It is a device that allows the light to pass through in only one direction so that back reflections are prevented. Back reflections can damage a laser source, cause it to mode hop, or introduce amplitude and frequency modulation to the original light. In can be difficult to design an optical system without back-reflections, as most optical components exhibit time reversal symmetry, so light travelling from the laser to a mirror at any point would then propagate back to the laser. The basic idea of a Faraday Isolator is to break this symmetry using a strong magnetic interaction. A schematic of a Faraday Isolator is shown in Figure 4.9. It contains a Faraday rotator with two polarisers (polarising beam splitters). The polarising beam splitter reflects all s-polarisation components while only allowing the p-polarisation to pass. The Faraday rotator is

the core component based on the Faraday Effect, whereby the polarisation of light rotates while travelling through optical materials that are exposed to a magnetic field. A critical difference between a Faraday rotator and a half-wave plate is that the direction of rotation in the former is dependent on that of the magnetic field only and not on that of light propagation. So the Faraday Rotator is non-reciprocal while the waveplate is reciprocal.

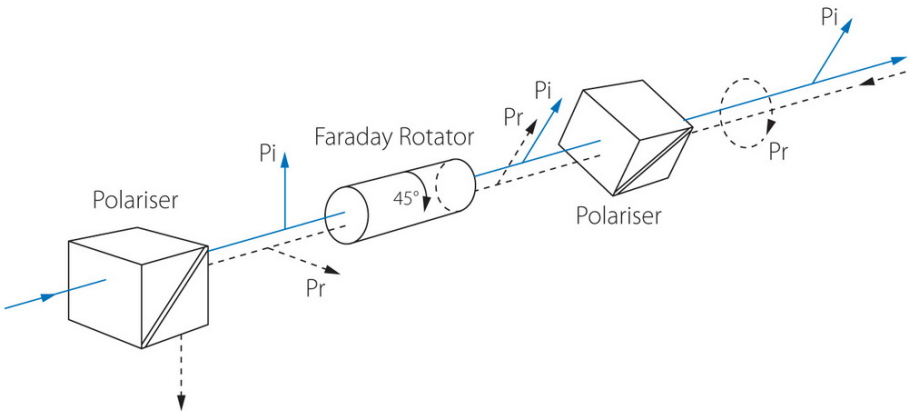

Figure 4.9: A schematic picture online showing the principle of a Faraday Isolator. Pi represents the beam propagating in the direction allowed by the isolator and Pr represents back reflections propagating in the opposite direction. This picture is taken from the website of the Altechna Company [113].

The light transmission allowed by the Faraday Isolator is usually specified by the manufacturer with an arrow on the device due to coating preferences. The incoming beam becomes linearly polarise after the input polariser. The direction of the polarisation is changed by 45° by the Faraday rotator and gets transmitted through the output polariser whose axis is 45° from the input polariser. All back reflections will be polarise by the output polariser, rotated by 45° in polarisation and dumped (reflected) by the input polariser.

The rotational alignment of the input and output polarisers for the Faraday Isolator is carried out in three steps, as follows. Firstly, as the input beam we is already linearly polarise, the direction of polarisation is adjusted to be along the axis of the input polariser so that the transmitted power is maximised. This is achieved by rotating a half-wave plate before the Faraday Isolator and measuring the intensity of the reflected light by the input polariser with a power meter until it is close to

zero. Secondly, the rotational angle of the output polariser is adjusted until the transmitted power from the isolator is maximised, which should be equivalent to the reflected power by the output polariser being minimised. Thirdly, the Faraday Isolator and polarisers are reversed so that the incoming beam is incident on the output polariser. The power meter is used to measure the power transmitted through the whole isolator. If it is not zero, the rotation of the output polariser is fine tuned (in this step it is the polariser close to the input port) until the transmitted power is minimum. The Faraday Isolator is then returned to its original orientation. The third step is a double check to make sure that all back reflections are blocked by the isolator; this is more important than maximising the output.

Electro-Optic Modulator

The Electro-optic modulator (EOM), or so-called *Pockels cells*, is an optical device that can modulate the phase, frequency, amplitude, or even polarisation of the light by applying the electro-optic effect. EOMs are used in the Pound-Drever-Hall technique for modulating the phase of the light field, as generating the error signal requires a modulation-demodulation regime (see Appendix C). All EOMs we use in this experiment are broadband phase modulators (Model 4004) from Newport Corporation.

The phase modulator contains an electro-optic crystal with two electrodes on two opposite sides, with the optical axis passing between them. The index of refraction of the crystal changes when an electric field is applied across the electrodes and thus the phase of the light passing through the crystal is modified. With suitable crystals, this change can be close to linear across one or several wavelengths. The change in index of refraction is given by

$$\Delta n = \frac{1}{2} n_e^3 r_{33} E, \tag{4.9}$$

where Δn is the change in the index of refraction, n_e is the unperturbed index of

refraction along the extraordinary axis, r_{33} is the appropriate element in the electro-optic tensor and E is the electric field applied across the crystal. So the total phase change is given by

$$\Delta\phi = \frac{2\pi}{\lambda}\left(\frac{1}{2}n_e^3 r_{33}\right) V d, \tag{4.10}$$

where V is the voltage of the electric field and d is the thickness of the crystal along the beam propagation direction. The voltage that changes the phase by π is defined as the half-wave voltage V_π, which is usually hundreds or even thousands of volts. For the Model 4004 phase modulator, V_π is quoted as being 210 V at 1064/,nm, corresponding to a modulation depth of 0.015 rad/V.

Figure 4.10 shows the schematic plot of the Model 4004 phase modulator. The crystal axis is placed in the vertical direction and the electric field is applied along this axis. The phase modulator has a preferred polarisation direction, along which the beam polarisation should be oriented to within about 1°.

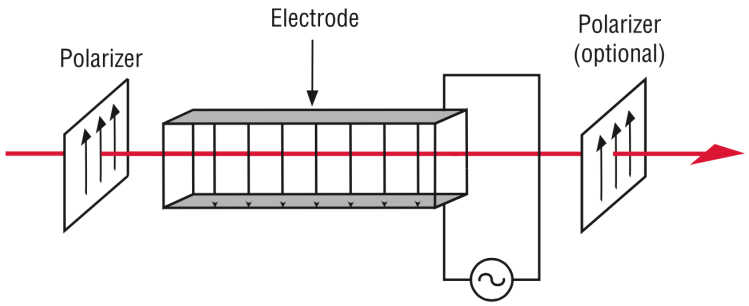

Figure 4.10: A schematic plot of the Model 4004 phase modulator from the Newport Corporation. This picture is taken from its official website [114].

The Model 4004 phase modulator can be operated from DC up to 100 MHz. The specifications as quoted by the manufacturer are shown in Table 4.3. The modulation frequency we use for the Pound-Drever-Hall locking loop for the reference laser is 15 MHz and the voltage amplitude applied to the modulator is 8.4 V. This yields a modulation depth of $\beta_r = 0.126$ rad. According to Equation C.3, the phase modulation creates two sidebands whose amplitudes are both $\beta/2 = 6.3\%$ of the carrier light. The modulation frequency for the probe laser beam is 1 MHz with an voltage amplitude of 9.1 V, producing a modulation depth of $\beta_p = 0.137$ rad.

Table 4.3: Specifications of the Model 4004 phase modulator.

Specification	Model 4004
Wavelength range	900 nm to 1600 nm
Operating frequency	DC to 100 MHz
Modulation depth	15 mrad/V (1064 nm)
V_π	210 V (1064 nm)
Material	MgO:$LiNbO_3$
Maximum optical density	4 W/mm^2 (1064 nm)
Aperture	Φ2 mm
Input impedance	20 pF

4.2.2 Electronic devices

The electronic components used in a Pound-Drever-Hall loop typically include a photodetector, which converts optical signals to electronic signals; a local oscillator; a mixer, which demodulates the signal to produce the error signal; a servo that provides a negative frequency-dependent feedback, and, in most cases, some additional amplifiers and filters.

Photodetector

The photodetector usually consists of a photodiode which converts light photons into current with a large output impedance. To a good approximation it can often be treated as an ideal current source. This current is in most cases fed into some pre-amplification circuits to deliver a voltage output. The photodetector used in the Pound-Drever-Hall stabilisation in our setup is designed and manufactured in house. A schematic of the pre-amplification circuit is shown is Figure 4.11. The detector has two outputs: the DC output and the AC output, with electronic gains of 3.9 and 5.2, respectively. The lower cut-off frequency of the AC port is given by $f_c = 1/(2\pi\tau) \approx 1/(2\pi R_8 C_{16}) = 3.1\,\text{kHz}$. When there is no light incident on the photodetector, it has a dark voltage of $-13.0\,\text{mV}$ at the DC port. The total gain for the DC channel is measured to be 145.7 mV/mW. The gain of the photodiode (including the first op-amp) is therefore estimated to be about 37.4 mV/mW.

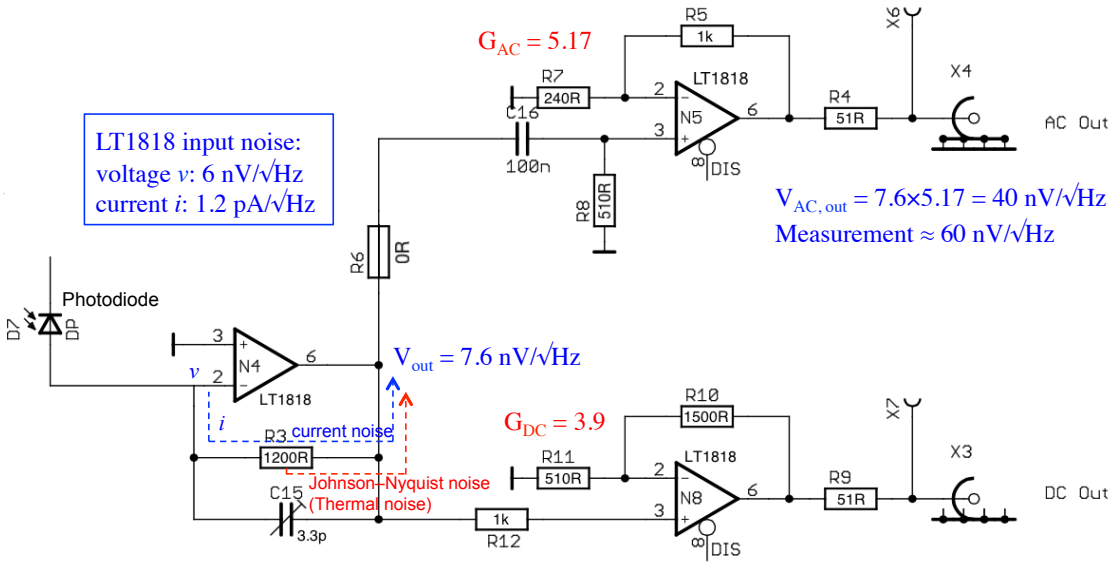

Figure 4.11: The schematic of the photodetector for the Pound-Drever-Hall stabilisation.

Local oscillator

The local oscillator signal is produced using a two-channel signal generator. One of the channels delivers a sinusoidal signal at 15 MHz with an amplitude of 8.4 V to the EOM; the other delivers a power of +7 dBm to the RF mixer. The phase difference between the two channels can be easily adjusted by the signal generator so that the modulation phase and demodulation phase can be matched, generating an error signal at its maximum amplitude, given by Equation C.9.

RF mixer

An RF Mixer is a 3-port active or passive non-linear device whose output signal is, in the ideal case, the product of the two input signals. For two sinusoidal input signals, this produces components with frequencies at the sum and the difference of the frequencies of the input signals at the output port. It is commonly used as a phase detector or as a demodulator where the frequency of a signal needs to be down-converted or up-converted. One of its inputs is the local oscillator signal and the other is the RF signal whose amplitude and phase is to be measured.

The mixer we use is a passive frequency mixer ZAD-1-1+ from MiniCircuits which has a operating bandwidth from 100 kHz to 500 MHz. As the Pound-Drever-Hall stabilisation uses same frequencies for the modulation and demodulation processes, the output signal of the mixer contains a DC term (the difference) and a term with twice the frequency (the sum). The DC term gives the error signal of the technique and the double frequency term is filtered out by a low-pass filter.

Servo

A servo system is, in general, an automated feedback system, which is used to maintain some physical parameter at a target value, or within some range. In most cases, this will involve some sort of electronic feedback control, which can be either analogue or digital. A linear servo system is defined by its transfer function, which determines the feedback response to a sinusoidal driving signal as a function of frequency. The digital servos we use here are designed by our group especially for Pound-Drever-Hall cavity stabilisation techniques. The electronic module can scan the cavity and fit the measured reflected light intensity to the theoretical functional form for a cavity resonance, and hence find cavity resonances and lock the cavity automatically. This uses the DC component of the photodetector signal. This component is only used in this initial stage, to adjust the cavity towards the resonance condition. Once the cavity is on resonance, the AC component of the photodetector output is used in the servo mode to maintain the cavity lock. It is fed into the RF input of the mixer where it is mixed with the Local Oscillator signal to produce the error signal, which is proportional to a deviation of the cavity from lock. This error signal is then fed into the servo. A negative feedback signal is then generated by the servo to compensate the deviation. Specifications of the servo are listed in Table 4.4.

The servo we use can provide a gain up to 10. It has a phase inverter which can be set to give a phase delay of either 0 or 180°. Which phase is used depends on the response of the PZT (stretch or shrink given a positive voltage) and the demodula-

Table 4.4: Specifications of the digital servo used for the Pound-Drever-Hall stabilisation.

Specification	Digital servo
Servo input impedance	$> 4\,\mathrm{k\Omega}$
Servo maximum input (AC)	$\pm 1\,\mathrm{V}$
Servo maximum input (DC)	$\pm 1\,\mathrm{V}$
Servo maximum output	$\pm 10\,\mathrm{V}$ (minimum load $2\,\mathrm{k\Omega}$)
Servo maximum gain	10 (with 0 or 180° phase delay)
Servo bandwidth	300 kHz
Ramp maximum output	20 V peak-to-peak
Ramp frequency	1 Hz to 100 Hz

tion phase. The servo also incorporates three integrators with cut-off frequencies at 100 Hz, 1 kHz and 10 kHz respectively to introduce extra gains below these frequencies. Transfer functions of the servo with and without these integrators are shown in Figure 4.12. Note that a integrator introduces a phase delay of 90° below the zero gain frequency. The reason for using integrators is to suppress the motion of cavity mirrors only at low frequency due to the ground motion and the air flow. At higher frequencies, use of an integrator could excite mechanical and electronic resonances due to the phase delay; this is discussed in the following section.

The digital servo can work in three modes:

1. Ramping mode. In this mode, the feedback loop stays open. The servo outputs a triangular wave, usually at a frequency of about 10 Hz, which is applied to the PZT of a cavity through a high-voltage amplifier. This causes the PZT to stretch and shrink quickly, thus moving the cavity mirror forward and backward over a typical scale of several microns. This mode is used when the cavity is being aligned or whenever a free spectral range and the shape of an error signal need to be observed.

2. Scanning mode. The servo tries to find the operating point by increasing or decreasing its output slowly. Lock detection is performed during this time by checking that the AC signal and DC signal from the photodetector are within specific ranges (introduced in Section 4.2.3). At resonance, the error signal will be close to zero, while the DC signal corresponding to the amount of light reflected by the

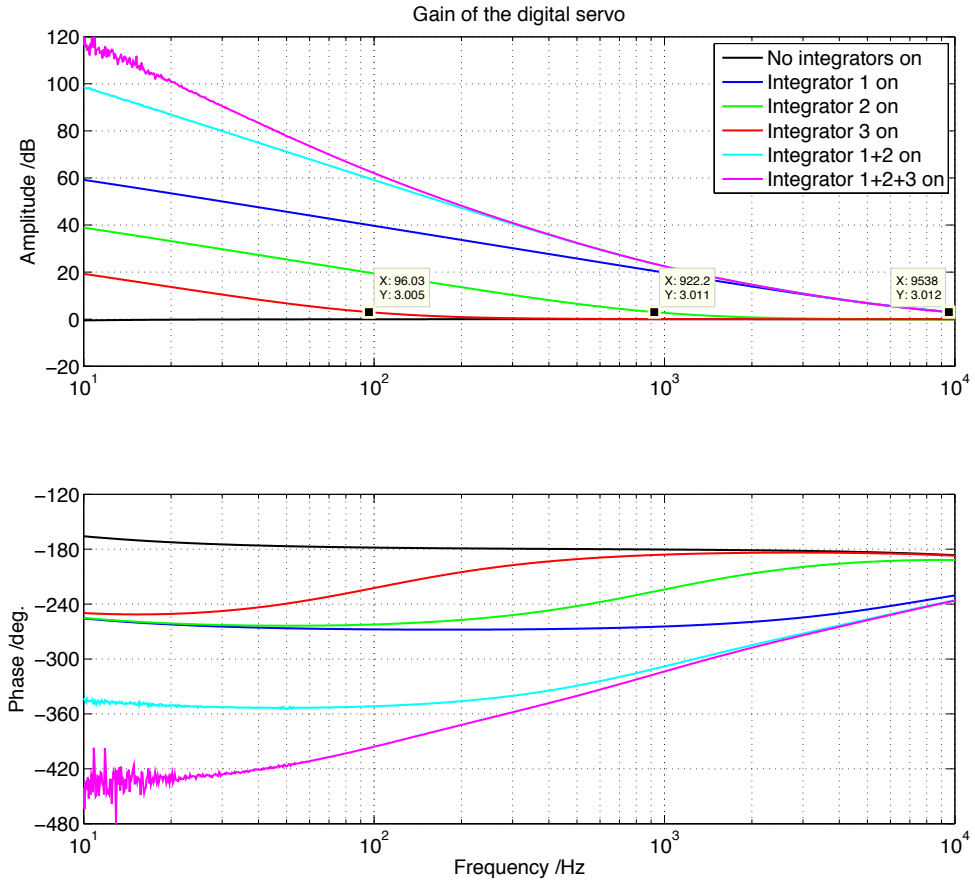

Figure 4.12: Measured transfer functions of our servos. The servo incorporates three integrators with cut-off frequencies at 100 Hz, 1 kHz and 10 kHz respectively. Note that each integrator introduces a phase delay of 90° below the zero gain frequency.

cavity will be at a positive or negative peak depending on the photodetector's DC trans-impedance.

3. Locking mode. When the DC signal and AC input signal are both within the pre-set threshold, the servo automatically closes the loop, and the laser frequency or the cavity length is stabilised at the operating point. All frequency or length equivalent noises are suppressed by a factor determined by the gain of the whole loop.

High-voltage amplifier

The piezo-electric transducer (PZT) requires hundreds of volts to actuate relevant displacements. The transducer used for cavity length control is an expensive device and should be operated in the most efficient and safe way with regard to stroke and reliability. The SVR 500 High-voltage amplifier (HV Amp) we use from Piezomechanik is specifically designed to actuate a capacitive device like the PZT. Specifications are listed in Table 4.5. It has an output voltage range from $-100\,\mathrm{V}$ to $500\,\mathrm{V}$. However, the PZT integrated in the laser only allows a maximum input of $\pm 100\,\mathrm{V}$. To avoid exceeding this limit, an attenuator with a constant attenuation factor of 5 is applied to the output signal from the high-voltage amplifier. This yields a maximum actuator voltage range of $-20\,\mathrm{V}$ to $100\,\mathrm{V}$ applied to the laser PZT.

Table 4.5: Specifications of the SVR 500 high-voltage amplifier.

Specification	HV Amp
Input signal	$\pm 5\,\mathrm{V}$
Input impedance	$10\,\mathrm{k}\Omega$
Output impedance	$5\,\mathrm{k}\Omega$
Maximum output voltage	$-100\,\mathrm{V}$ to $500\,\mathrm{V}$
DC offset range	$-100\,\mathrm{V}$ to $500\,\mathrm{V}$
Gain	100 (without attenuation)
Maximum output current	$15\,\mathrm{mA}$
Bandwidth	$20\,\mathrm{kHz}$
Average power	$7\,\mathrm{W}$

4.2.3 The Control loop

In Figure C.2, we show a schematic of the Pound-Drever-Hall loop including most of the optical and electrical devices. In the remainder of this section, we describe in more detail how the reference laser is locked to the cavity.

Lock acquisition

The signal after the mixer and a low-pass filter (the point e in Figure C.2, called the *error point*) gives the error signal we want. In a practical setup, before a good error signal can be observed, the incoming beam must be mode matched and aligned to the cavity eigenmodes.

The mode matching is performed by tuning positions of the two lenses introduced in Section 4.1.4, so that the size and position of the resulting beam are well matched to those of cavity's eigenmodes. The alignment is usually achieved by adjusting two steering mirrors before a cavity to align the axis of the incoming beam to the the axis of the cavity eigenmodes. Mounts of the two steering mirrors can provide 4 degrees of freedom: x-tilt and y-tilt angles for each mirror, which tune the offset and angle of the resulting beam axis in pitch and yaw directions. We have two laser sources and their beams are both aligned to the near-unstable cavity. The probe laser should be first aligned to the cavity, using the two steering mirrors A1 and A2 shown in Figure 4.4. The reference laser can be then aligned to the cavity by tuning the steering mirrors M1 and M2 which are located before the central beam splitter. In this case, the two laser beams be aligned once they are combined, and should both be matched to the cavity axis.

The mode matching and alignment of a cavity are practically carried out by observing the intensity of the beam reflected or transmitted from the cavity when the cavity or the laser is being scanned. Here, scanning the cavity refers to the cavity length being linearly increased or decreased over a range of order a wavelength. Similarly, scanning the laser means the laser frequency is being linearly changed by the scale of a free spectral range of the cavity. For the Pound-Drever-Hall technique, a photodetector is placed at the cavity's reflection port. The DC output of the photodetector gives the intensity of the beam reflected by the cavity. The servo should be in the 'ramp' mode and output a triangular wave driving the PZT so as to scan the cavity length or the laser frequency back and forth. Usually the scanning should ensure at least resonances over a full free spectral range can be observed. To carry

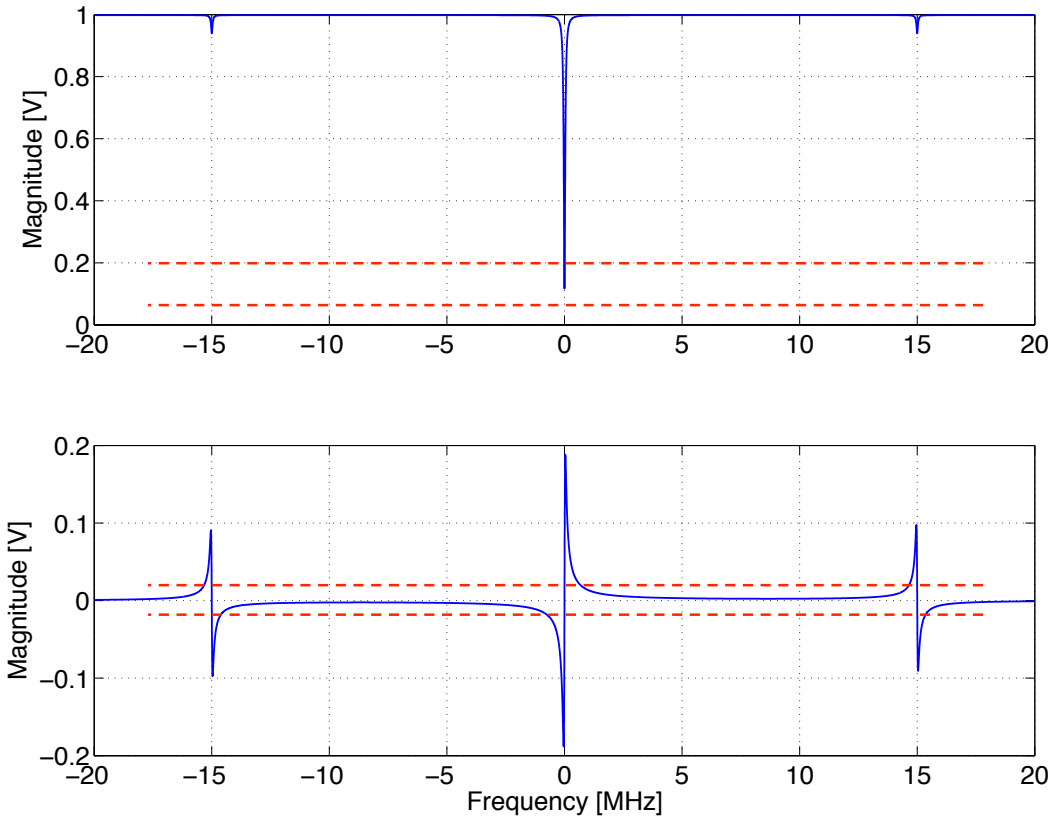

Figure 4.13: The two signals sent to the servo for lock acquisition. The upper plot is the DC output signal from a photodetector measuring the intensity of light reflected by the cavity when scanning the laser frequency. The cavity is usually mode matched and aligned to a fundamental mode. When a strong clear peak corresponding to the fundamental mode is observed, with all higher order mode peaks minimised, the cavity can be assumed to be well-mode matched and aligned. The lower plot shows the corresponding error signal. The predefined threshold window for lock acquisition in this example is (0.06 V, 0.2 V) for DC output of the photodetector and (−0.02 V, 0.02 V) for the error signal.

out mode matching, we need to minimise the resonance of the second order mode, while to optimally align the cavity, we need to minimise the resonance of the first order mode (introduced in Section 4.4). If the measured intensity change over a full free spectral range only shows a clean resonance of the fundamental mode, with all higher-order mode peaks minimised closed to zero, the cavity is well mode matched and aligned. A camera is usually necessary to measure the shape of the transmitted beam in order to distinguish which mode is resonating.

The upper plot in Figure 4.13 shows the simulated DC output signal from the photodetector, where a clean and strong peak of the fundamental mode is observed, as would be the case when the cavity is perfectly mode matched and aligned. The x-axis in the plot is the frequency deviation from the resonance of the fundamental mode. The two small peaks around the fundamental mode at ±15 MHz are phase modulation sidebands. The lower plot in Figure 4.13 gives the corresponding error signal at the error point when the laser frequency is being scanned. In a practical setup, the demodulation phase needs to be adjusted in order to match the phase of the modulation signal. This is performed by tuning the output phase difference in the two-channel local oscillator until the peak-to-peak voltage observed in the error signal is maximised.

The two subplots in Figure 4.13 represent the two signals sent to the servo for lock acquisition. To detect cavity resonance and lock the cavity, the servo is switched to 'scanning' mode. In this mode, the servo examines these two inputs, comparing the signals to predefined threshold windows. If both signals are inside their respective windows, the cavity is assumed to be in resonance and the servo closes the loop immediately with a predefined gain. An integrator is then applied into the loop to suppress the deviation between the cavity length and the laser frequency below its cut-off frequency. Here the integrator number 3 with a cut-off frequency of 100 Hz (see Figure 4.12) is used. The other integrator circuits, integrator 1 and integrator 2 have cut-off frequencies of 10 kHz and 1 kHz, respectively, which are close to the frequencies of electrical and mechanical resonances (the lowest of which are of order 1 kHz). These are therefore not used, as the phase delay just above the cut-off frequency may excite these resonances and destabilise the servo loop.

Improve locking stability

The cavity is contained in a box which has only a small hole for the laser beam to enter. This box reduces air flow between the two cavity mirrors and makes the frequency stabilisation control loops more stable. It significantly increases the

operability and lockability of the cavity.

A Pound-Drever-Hall stabilisation loop is shown in Figure 4.14 including all relevant optical and electrical components. The laser is modulated at 15 MHz before entering the cavity. The reflected beam is detected by a photodetector and demodulated by the mixer also at 15 MHz to generate the error signal. The error signal is then sent to the servo and negatively fed back to the integrated PZT in the reference laser through a high voltage amplifier, to cancel out the deviation of the laser frequency from the cavity length. In this figure, a virtual adder box is placed between the laser and the cavity to represent noise entering the loop.

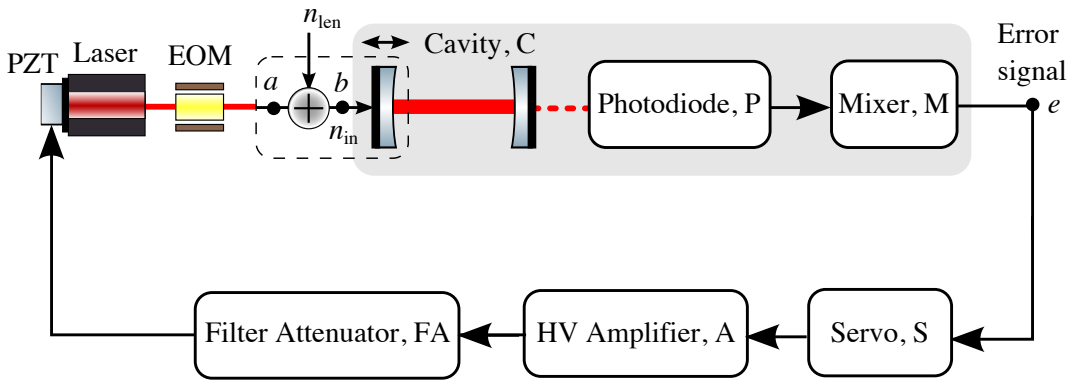

Figure 4.14: A Pound-Drever-Hall loop including all relevant optical and electrical components. Notice that the photodiode is at the reflection port of the cavity for the Pound-Drever-Hall technique.

A brief introduction of control loops can be found in Appendix B in [115]. For an automatic feedback control loop, the in-loop residual noise is inversely proportional to the gain of the whole loop:

$$n_{\text{in}} = \frac{n_{\text{len}}}{1 - G_{\text{OL}}}, \tag{4.11}$$

where G_{OL} is the open loop gain of the whole system, n_{in} is the in-loop residual noise and n_{len} is the out-of-loop length equivalent noise that moves the system away from the operating point, *i.e.*, the noise when the feedback loop is open and the system is free running. The in-loop noise means the residual noise after the system has been controlled, by closing the servo loop. The length-equivalent noise here represents

deviations between the cavity length and the laser frequency in terms of length. As the laser frequency change is equivalent to the cavity length change according to the following relationship, it is easy to convert between frequency noise and length noise:

$$\frac{\Delta f}{f_0} = \frac{\Delta L}{L_0}, \tag{4.12}$$

where f_0 is the frequency of the light from the laser and L_0 is the length of the cavity.

In control systems, frequency-domain analysis is commonly used, as signals and the response of a system are much simpler to describe as functions of frequency, rather than of time. In the frequency domain, G_{OL} in Equation 4.11 is a complex number with a modulus and argument corresponding to amplitude and phase, respectively. The value of the amplitude is usually a negative number which reflects the ability of the system to prevent itself from deviating from the operating point. In theory, it is ideal to have a constant gain and zero phase delay over all frequencies. But practical devices all involve low-pass filters or band-pass filters, as they cannot have an infinitely fast response. Phase delays happen when the servo's response cannot follow the signal. To determine quantitatively whether these phase delays will destabilise the control loop, it is useful to consider the transfer function as a function in the complex frequency plane, where the amplitude corresponds to frequency (or angular frequency) and the argument corresponds to phase. Poles in this plane represent positions where the transfer function diverges, which corresponds to signals that would cause the loop response to grow indefinitely. Analysing the positions of the poles and zeroes can give some guidance on how the servo can be modified to create a stable loop. The transfer function of the loop should have enough gain at frequencies where the noise is significant. A stable loop require us to ensure that the denominator in Equation 4.11 is not zero at any real positive frequency, as this will make the loop unstable, so that a small noise will lead to an indefinitely growing signal.

In a Pound-Drever-Hall stabilisation setup, the main sources of length equivalent

noise come from mirror motions and air flows at low frequencies, typically below 10 Hz. Correspondingly, the feedback control system should provide sufficient gains at these low frequencies. It is unnecessary and actually not easy to achieve high gains at high frequencies where electrical and mechanical resonances are common. We can therefore aim to produce a simple transfer function for the loop, namely, a one-pole low-pass filter. We use a pole frequency of 10 Hz. The point where the amplitude of the loop gain reduces to 1 is called the *unity gain frequency*. It is obvious that at the unity gain frequency, the phase delay of the whole loop must not be 360° (or the denominator in Equation 4.11 becomes zero). The feedback control loop naturally has a phase flip of 180° and the low-pass filter has a phase delay of 90°. As a result, we only have 90° phase for gain margin (a brief introduction of gain margin and phase margin can be found in Appendix B in [115]). In addition, the high-voltage amplifier has a bandwidth of 20 kHz and the optical cavity acting as a low-pass filter has a pole frequency at about 35 kHz. This means that we will probably accumulate in total 360° phase between 20 kHz and 35 kHz. Phase delays introduced by imperfect electronics and positions of resonances will eventually limit the maximum gain we can practically achieve. On resonances, the response of the system experiences a 180° flip in phase. To avoid the loop becoming unstable, we aim to ensure that the loop gain is smaller than 1 at frequencies where resonances occur.

The transfer function of the servo has been shown in Section 4.2.2. The servo has a bandwidth up to 300 kHz. Figure 4.15 shows measured transfer functions of the high-voltage amplifier and the laser PZT.

The PZT is electrically capacitive. When added to the loop (see Figure 4.16) it acts as a low-pass filter. The pole frequency of a single-pole low-pass filter is the frequency at the gain is reduced by 3 dB; it has at this frequency a phase lag of 45° and can be calculated by

$$f_p = \frac{1}{2\pi RC}. \tag{4.13}$$

In Figure 4.15, the green curve shows the measured pole frequency of the PZT, which

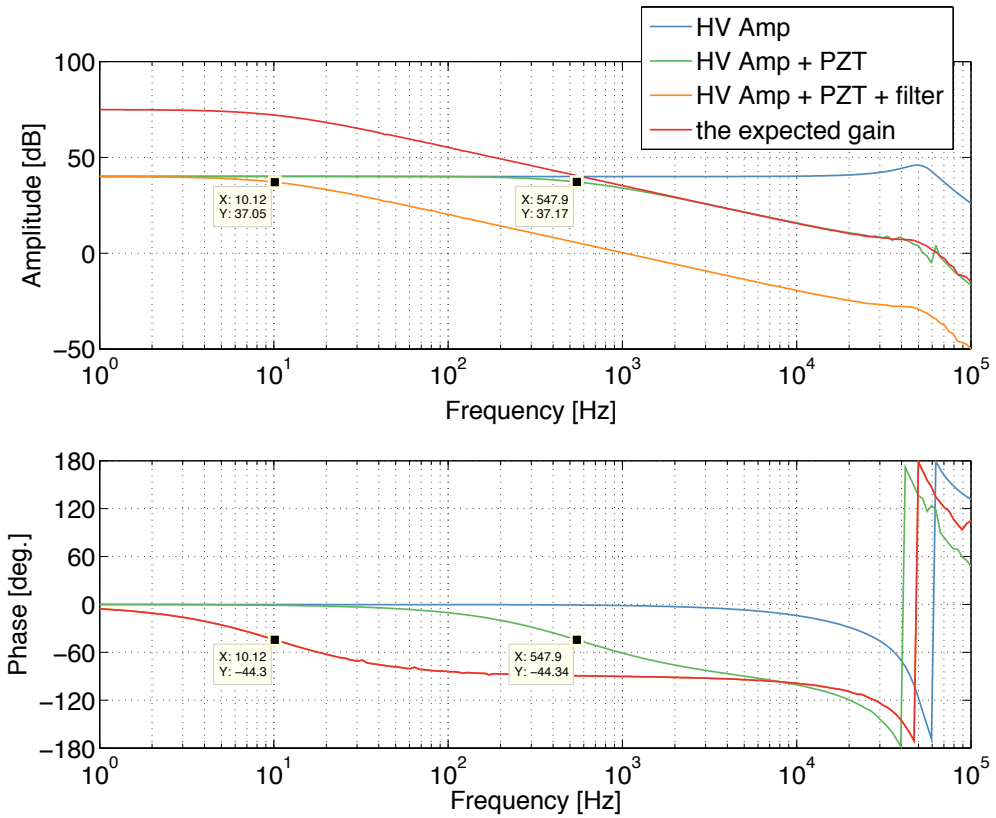

Figure 4.15: Transfer function of the high-voltage amplifier and the laser PZT. The PZT acts as a low-pass filter which has a pole at $\sim 550\,\mathrm{Hz}$. The pole frequency of the loop is expected to be brought down to 10 Hz by using an extra filter, so that we can further increase the gain at low frequencies, while the gain above 550 Hz stays as the same.

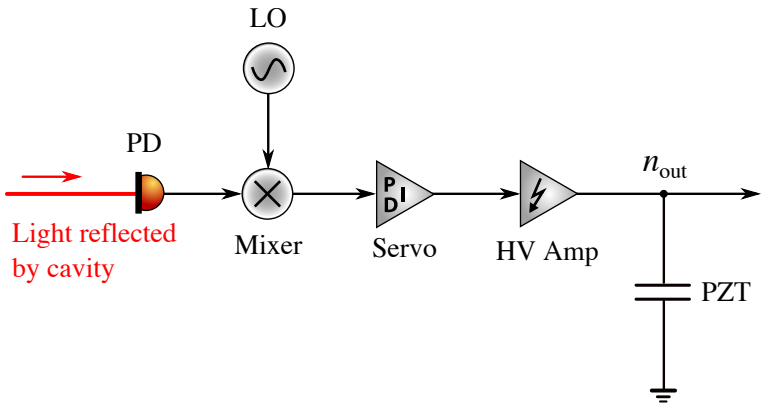

Figure 4.16: Electronic devices in a Pound-Drever-Hall loop. The PZT is electrically capacitive and hence acts as a low-pass filter.

is about $f_{\mathrm{PZT}} = 550\,\mathrm{Hz}$. This determines the pole frequency of the whole loop as all other devices have higher bandwidths. This means we need an extra low-pass filter

to bring the pole frequency down to 10 Hz. The low-pass filter is essentially an RC circuit, with a resistor and a capacitor with a large capacitance, and is connected between the high-voltage amplifier and the laser PZT (see Figure 4.17). This low-pass filter is integrated with an attenuator which is labelled the Filter Attenuator in Figure 4.14. The attenuator has a constant gain of 1/5 to protect the laser PZT, whose input range is smaller than the maximum voltage that the high-voltage amplifier can deliver. The low-pass filter reduces the loop-gain at above its pole frequency, but after we reduce the attenuation from other components in the loop, such as the servo and the high-voltage amplifier, the total open loop gain will be the same above the previous pole frequency at 550 Hz (see the red curve in Figure 4.15) and it will increase like 1/f (compared with the previous gain) down to 10 Hz. At the same time, it will reduce out-of-loop actuator noise and it will save us from attenuating the feedback signal so much, improving electronic noise performance.

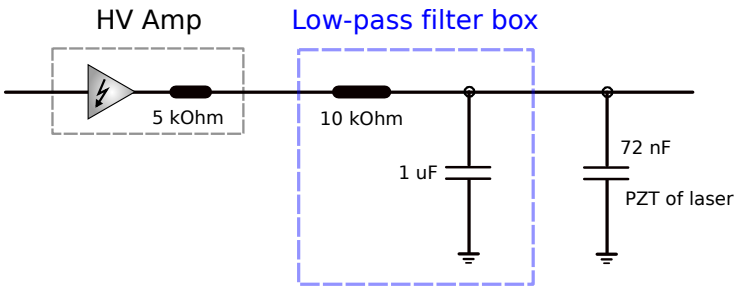

Figure 4.17: An external low-pass filter is introduced into the loop to bring down the pole frequency to 10 Hz.

Transfer function measurements

Transfer functions are very important in control systems. They are not only used for the design of a control loop, but also determine how the noise propagates along the loop. To fully understand this, it is essential to know the transfer function and noise characteristics of each component in the loop.

The transfer function or the gain of a plant is usually measured by taking its output over input signal. It is relatively easy to measure transfer functions of electronic devices such as the servo, the high-voltage amplifier and the filter/attenuator. Fig-

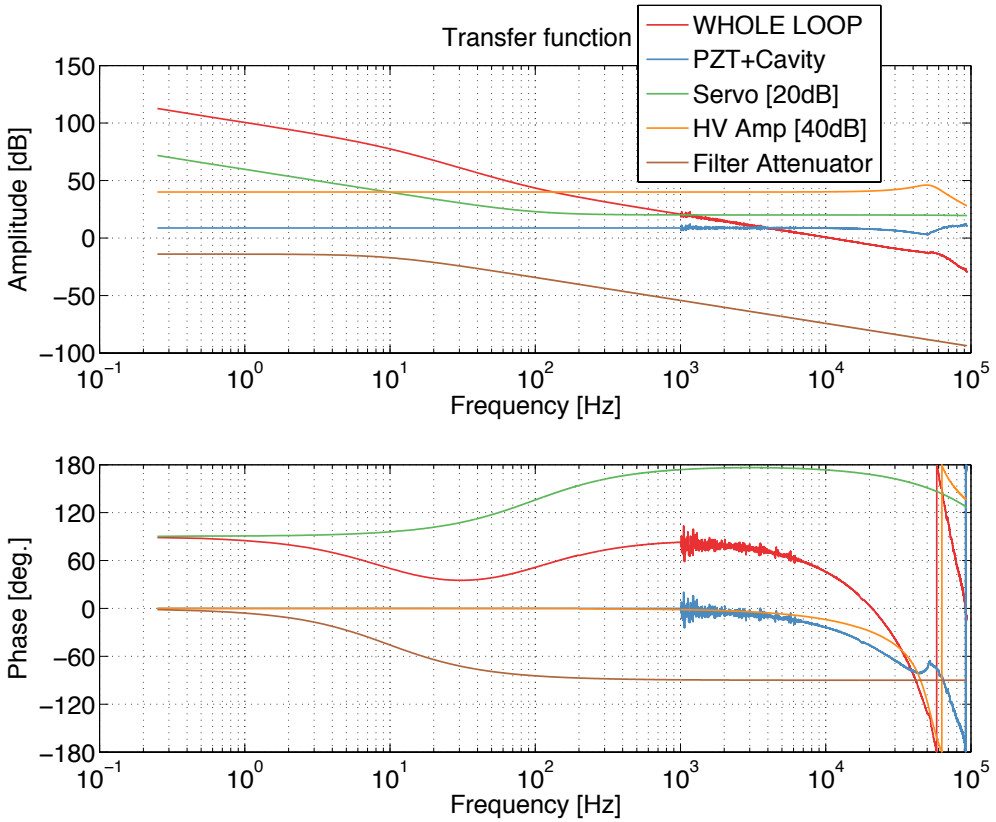

Figure 4.18: The measured transfer functions of components in the Pound-Drever-Hall loop.

ure 4.18 shows the measured transfer functions of these electronic components. They are measured with a network analyser in an open loop. It is more difficult to measure the transfer function of optical components, such as the laser with the PZT, and the cavity with its readout devices (the photodetector and the mixer). Their transfer function measurements are introduced in Section 4.2.3.

The transfer function of the whole loop can be directly measured in the setup shown in Figure 4.19. A swept sine wave test signal s created from the network analyser is injected at the error signal point. The ratio of the signals e and c gives the open loop gain of the whole loop G_{OL}, which can be measured at the network analyser's two input channels:

$$G_{\mathrm{OL}} = \frac{e}{c}. \tag{4.14}$$

The problems of this method is that, at low frequencies, it is not easy to measure

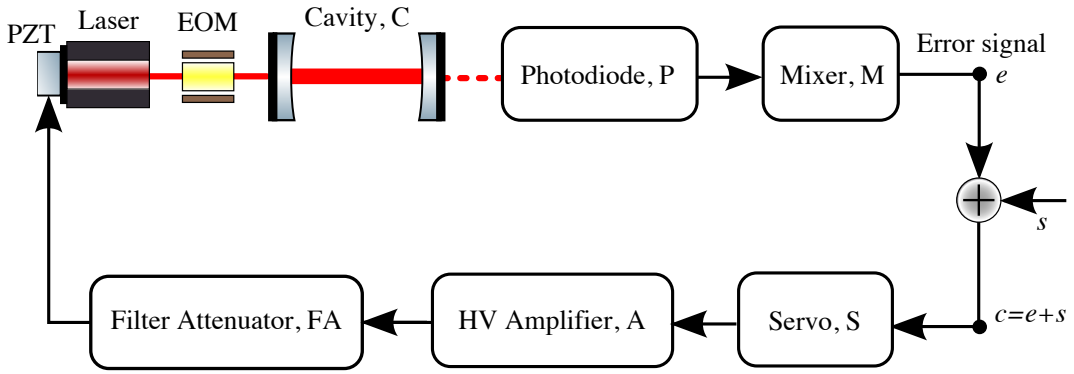

Figure 4.19: A method to measure the open loop transfer function in a closed loop.

the loop transfer function as G_{OL} becomes very large (in the ideal theoretical case it tnds to infinity) due to the integrator in the servo system.

$$e = \frac{G_{\mathrm{OL}}}{1 - G_{\mathrm{OL}}} s \quad \text{and} \quad c = \frac{1}{1 - G_{\mathrm{OL}}} s \tag{4.15}$$

In this case, when G_{OL} is very large, the signal c is too small to measure compared to the noise at this frequency range. As a result, we can only measure G_{OL} accurately above 1 kHz. However, at lower frequencies, it can be inferred from measurements at high frequencies, as we know the overall performance of each component. The gain of the whole loop is simply the product of the gains of all components in the loop,

$$G_{\mathrm{OL}} = G_{\mathrm{PZT}} G_{\mathrm{Cav}} G_{\mathrm{S}} G_{\mathrm{Amp}} G_{\mathrm{FA}}, \tag{4.16}$$

where G_{PZT} is the gain of laser PZT, G_{Cav} is the response of the near-unstable cavity, with its read-out devices, including the photodetector and the RF mixer, G_{S} is the gain of the servo, G_{Amp} is the gain of the high-voltage amplifier, and G_{FA} is the gain of the filter attenuator. We know G_{S}, G_{Amp} and G_{FA} to a high precision, as they are from pure electrical devices and thus can easily be measured over a large frequency range. It is not easy to measure G_{PZT} and G_{Cav} directly, but these are expected to show a frequency-independent response at low frequencies, so their

transfer functions can be calculated from our measurements above 1 kHz.

$$G_{\mathrm{PZT}}G_{\mathrm{Cav}} = \frac{G_{\mathrm{OL}}}{G_{\mathrm{S}}G_{\mathrm{Amp}}G_{\mathrm{FA}}}. \tag{4.17}$$

We expect the PZT has a linear and flat response below 1 kHz. The cavity has a pole frequency above 35 kHz and its response should also be very flat below 1 kHz, so $G_{\mathrm{PZT}}G_{\mathrm{Cav}}$ will both be constant below 1 kHz. Details of the calibration of the PZT and the cavity are introduced in Section 4.2.3. It is found experimentally that they do indeed have constant responses below 1 kHz. The value of $G_{\mathrm{PZT}}G_{\mathrm{Cav}}$ measured at 1 kHz is therefore used for calibration G_{OL} below 1 kHz.

The calibrated transfer functions from 0.1 Hz to 100 kHz are shown in Figure 4.18. Note that $G_{\mathrm{PZT}}G_{\mathrm{Cav}}$ and G_{OL} are inferred from measurements above 1 kHz. The high-voltage amplifier is operating at its maximum gain of 100 (40 dB). The servo provides a negative feedback signal (phase lag 180°) with a gain of 20 dB with an integrator, whose zero frequency is 100 Hz. The filter attenuator contains a low-pass filter with a pole frequency of 10 Hz and an attenuator with a constant gain of 1/5 (−14 dB).

We find that the whole loop has a unity gain frequency at around 10 kHz. The 0 (360°) phase lag point gives the maximum achievable unity gain frequency, which is around 20 kHz. This means that the loop is operating with a gain close to its maximum in the stable range. Figure 4.20 shows the measured in-loop power spectral density of the error signal. The blue curve shows the spectrum with the current loop-gain. If G_{OL} is further increased, a peak is observed at 26 kHz; this is probably due to a mechanical resonance causing the signal at that frequency to be amplified in the loop.

Calibration of optical devices

In this section, we describe how the transfer functions of the laser PZT and the 1 m cavity are measured. For optical devices, it may be not easy to measure their out-

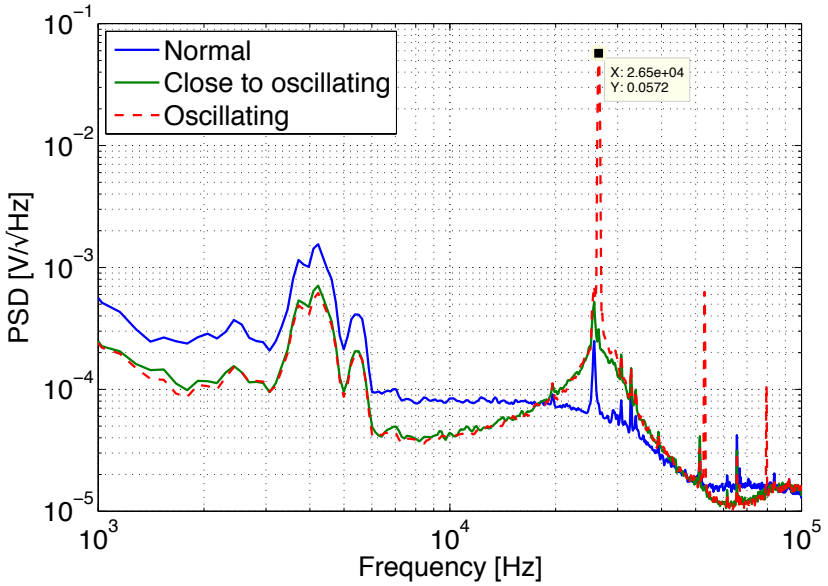

Figure 4.20: Oscillations that cause the loop to become unstable.

puts directly due to the difficulty associated with using optical sensors, and, in many cases, with the complexity of the optical readout system. For example, an optical spectrum must be measured in order to characterise the response of the laser PZT which changes the frequency of the laser. The optical spectrum anaylser usually requires fibre coupled optics with strict requirements on the alignment. An alternative, indirect way of measuring their behaviour is to include them as components in a closed Pound-Drever-Hall loop. Their transfer functions can be calculated if the transfer functions of the other components are measured, alongside the transfer function of the whole loop.

1) Laser PZT calibration

The integrated PZT in the reference laser is calibrated in a Pound-Drever-Hall locking loop with a rigid triangular cavity which we call the mode cleaner (MC) cavity (see Figure 4.21). The laser beam is phase modulated at 15 MHz and injected into the rigid cavity. The mode cleaner is placed after the central beam splitter, at the position of the intermediate waist, which has a size of 371 μm (see Figure 4.4), which is the waist size of the mode cleaner cavity eigenmodes. The reflected beam is detected by a photodetector. The detected signal is then demodulated with an

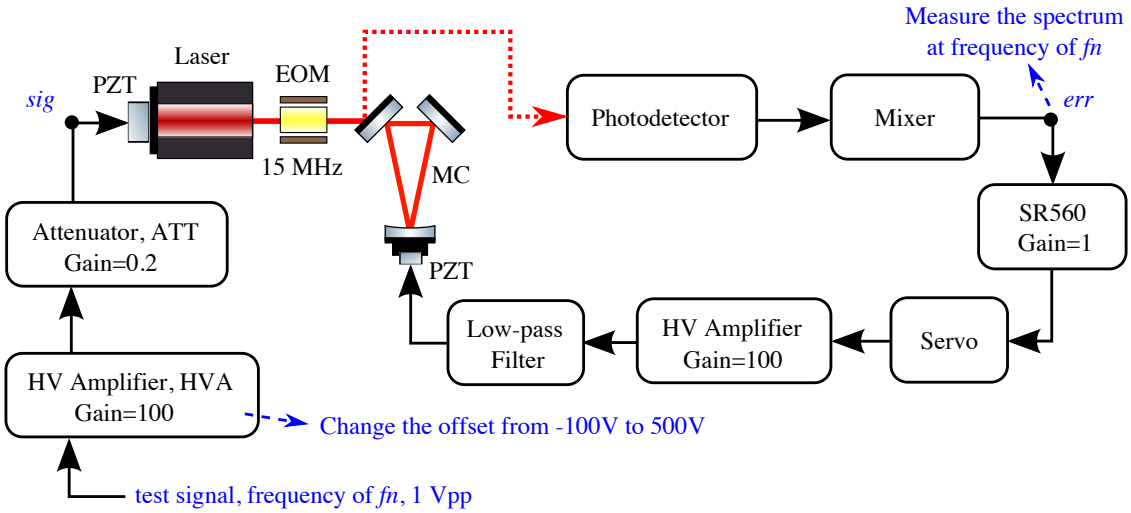

Figure 4.21: A loop used for calibration of the laser PZT.

RF mixer, giving the Pound-Drever-Hall error signal. The mode cleaner is locked by feeding the signal to the PZT attached to one of its mirrors.

In order to measure the gain of the laser PZT, a small sinusoidal test signal, sig, at a frequency of f_n with a known amplitude is injected into the loop via the laser PZT. The noise injected in laser frequency is 'seen' by the mode cleaner and suppressed by the control loop according to the gain of the whole loop. The amplitude of the residual signal can be found by measuring the power spectral density of the error signal, err, at the frequency of the injected signal, f_n. The gain of the laser PZT can then be calculated as

$$G_{\mathrm{PZT}} = \frac{err}{sig} \cdot \frac{1}{G_{\mathrm{MC}}} \cdot \frac{1}{1 - G_{\mathrm{OL}}} \quad [\mathrm{MHz/V}], \tag{4.18}$$

where G_{OL} is the open loop gain of the whole Pound-Drever-Hall loop and G_{MC} is the gain of the mode cleaner. G_{OL} can be measured according to the method described in Section 4.2.3.

The gain of the mode cleaner G_{MC} [1] can be derived from the error signal measured in an open loop. We apply a small ramp signal to the cavity's PZT and observe the

[1] In a Pound-Drever-Hall locking loop, by the gain of an optical cavity, it is usually meant the transfer function of the cavity, including its error signal; it therefore includes its readout circuits, including the photodetector and the RF mixer.

shape of the error signal with an oscilloscope (see Figure 4.22). This plot shows the measured error signal of our mode cleaner. It has a sharp slope in the centre with a zero-crossing point which is the operating point after the mode cleaner is locked. A deviation in the laser frequency from the operating point results in a change in the error signal. The gain of the mode cleaner is just the gradient of the slope at the operating point, which is $G_{\mathrm{MC}} = k_0$. By fitting the error signal according to Equation C.9 it is not difficult to derived the gain of the mode cleaner.

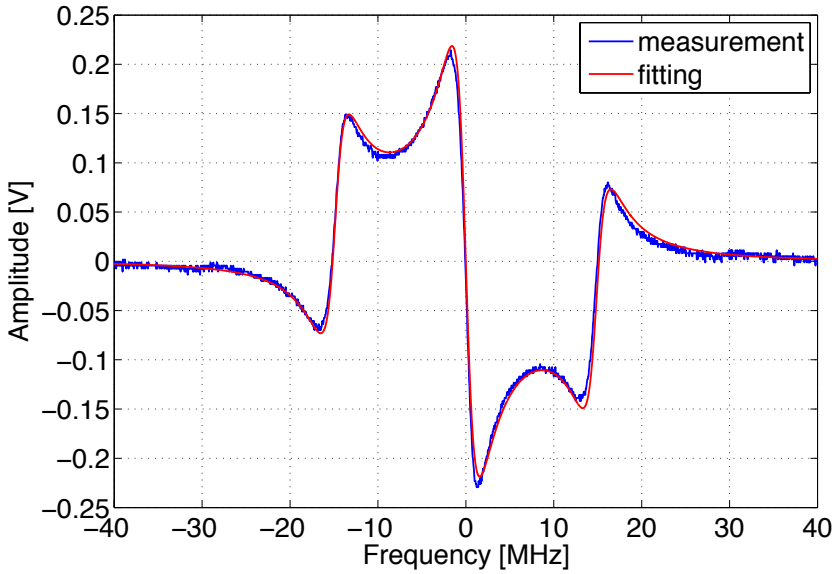

Figure 4.22: The measured and fitted error signals of the mode cleaner.

To check the linearity of the laser PZT, we vary the voltage offset applied to it and in each case measure the resulting cavity gain. Its response curve is shown in Figure 4.23; the gain lies in the range $1.19 \pm 0.09\,\mathrm{MHz/V}$. The PZT seems to have a slightly larger gain with a negative offset voltage. After calibrating the laser PZT, the mode cleaner is removed from the table.

2) The 1 m cavity calibration

The gain of the 1 m cavity can be also derived by fitting its error signal as described in the previous section. Alternatively, as we have already measured $G_{\mathrm{PZT}}G_{\mathrm{Cav}}$ in Section 4.2.3 (see the blue curve in Figure 4.18) and also know the gain of the laser PZT G_{PZT}, we can just take the ratio of them to calculate the gain of the cavity

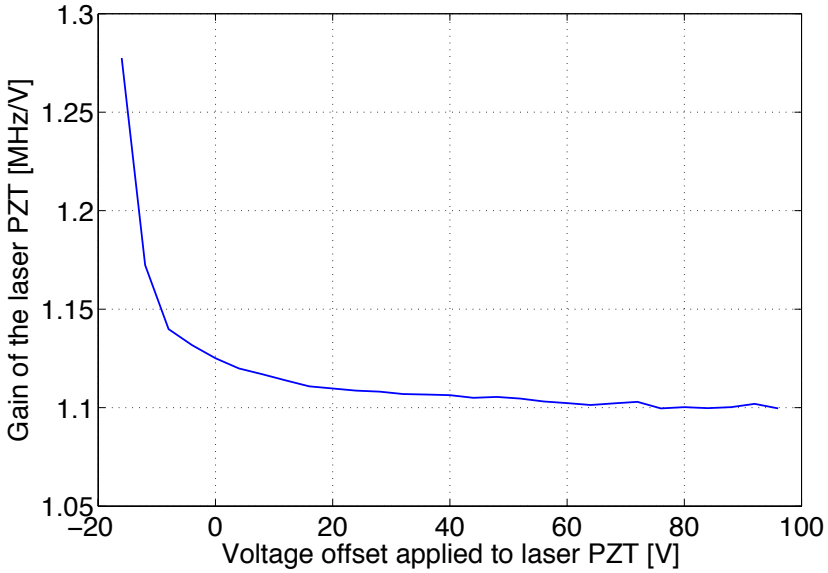

Figure 4.23: The measured gain of the laser PZT.

G_{Cav}.

Figure 4.24 shows the derived gain of the cavity from 1 kHz to 40 kHz. The optical cavity acts as a low pass filter. At low frequencies, the gain is almost flat with a value of $-112.5\,\mathrm{dBV/Hz}$ (or $2.37 \times 10^{-6}\,\mathrm{V/Hz}$). The pole frequency is located at about 36 kHz where its gain is decreased by 3 dB. However, the phase delay at this point is about 55°, which is 10° higher than the expected value for a single pole low-pass filter. The additional phase can be attributed to the finite bandwidth of the photodetector and the mixer.

4.2.4 Noise performance

In the Pound-Drever-Hall loop, by measuring the residual noise, we can know how well the laser frequency or the cavity length is stabilised. In any noise measurement, it is essential to first know the *analyser noise* and the *sensor noise* before measuring the noise of an instrument of interest. The analyser noise in this case is the noise of the network analyser used for the measurement, which imposes a lower limit on what signals we can measure. The sensor noise is the output noise of the sensor with

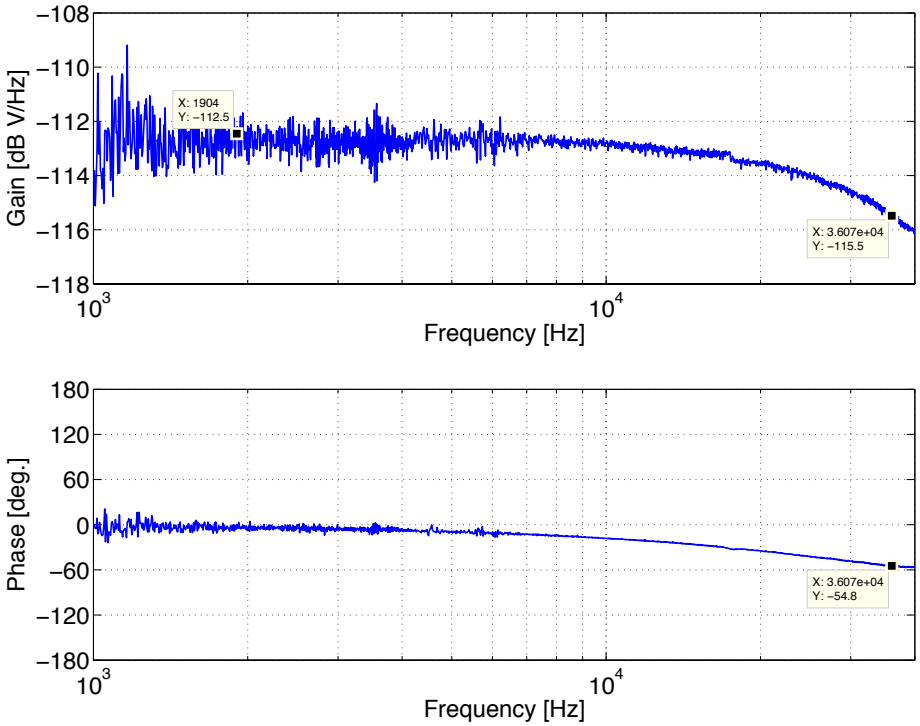

Figure 4.24: The measured transfer function of the 1 m cavity.

no input signals. For an optical sensor like a photodetector, the sensor noise is also called the *dark noise*, which is the electronic noise produced by the photodetector when there is no light incident on it. The sensor noise likewise limits how small a signal we can detect.

The sensor noise

The photodetector designed within our group contains a photodiode and a built in circuit which provides pre-amplification and produces a voltage output. The schematic is shown in Figure 4.11. The power of the light incident onto the photodiode should be in a suitable range where it is large enough to obtain a good signal-to-noise ratio, without saturating the photodiode or any of the subsequent electronic devices. The bias and amplification circuits for the photodiode are designed and built in house, and operate from DC to tens of MHz.

The current from the photodiode goes to an operational amplifier (op-amp) LT1818 through the load resistor R3 (1.2 kΩ). The noise at the output port of the op-amp has three main components: 1) input voltage noise of the op-amp, 2) voltage noise converted from the input current noise of the op-amp through the load and 3) *Johnson-Nyquist noise*, or the so called *thermal noise* of the load. The input voltage and current noise of LT1818 (at 10 kHz) are $6\,\mathrm{nV_{rms}}/\sqrt{\mathrm{Hz}}$ and $1.2\,\mathrm{pA_{rms}}/\sqrt{\mathrm{Hz}}$, respectively. The current noise is converted to voltage noise through R3, resulting in $1.44\,\mathrm{nV_{rms}}/\sqrt{\mathrm{Hz}}$. The thermal noise of a 1.2 kΩ resistor at room temperature is: $n_{\mathrm{Th}} = \sqrt{1.2} \times 4 = 4.38\ \mathrm{nV_{rms}}/\sqrt{\mathrm{Hz}}$. So the output noise in total is $v_{\mathrm{out}} = \sqrt{6^2 + 1.44^2 + 4.38^2} = 7.6\,\mathrm{nV_{rms}}/\sqrt{\mathrm{Hz}}$, which is amplified by the electronic gains at AC and DC out ports. The AC port has a gain of 5.17 thus the total output noise at AC out is expected to be $v_{\mathrm{AC}} = \sqrt{7.6^2 + 6^2} \times 5.17 = 50\,\mathrm{nV_{rms}}/\sqrt{\mathrm{Hz}}$. The red curve in Figure 4.25 shows the measured power spectral density of the AC output noise of the photodetector. The measured noise at 10 kHz is about $60\,\mathrm{nV_{rms}}/\sqrt{\mathrm{Hz}}$, which is close to the calculated value. The peaks at low frequencies are harmonics caused by the 50 Hz background signals in the lab.

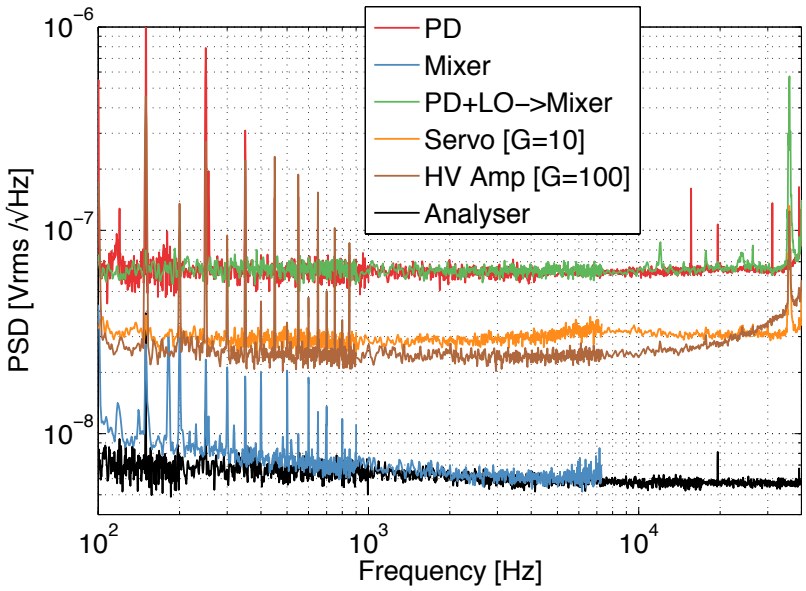

Figure 4.25: The measured electronic noise of each device used in the Pound-Drever-Hall loop.

The AC output signal of the photodetector is then delivered to the RF mixer for

demodulation. The noise of the mixer is usually negligible, but a passive mixer does attenuate the signal in the frequency conversion. The blue curve in Figure 4.25 shows the noise of the mixer. It is measured by feeding the 15 MHz local oscillator signal into the appropriate input, and blocking the RF input port with a 50 Ω terminator. The measured noise is close to the level of the analyser noise, which is much smaller than the noise from the photodetector. The green curve shows the noise after we connect the photodetector output to the RF input port. It is at about the same level as the photodetector's output noise.

Noise of amplifiers

In a loop containing several stages of amplification, in order to achieve a loop whose noise is limited by the sensor noise, the basic rule is that the *input internal noise* of a certain amplifier should be always much smaller than the output noise of the previous stage. Figure 4.26 shows a subsection of the Pound-Drever-Hall loop in which the servo and the high-voltage amplifier supply tunable gains for the loop.

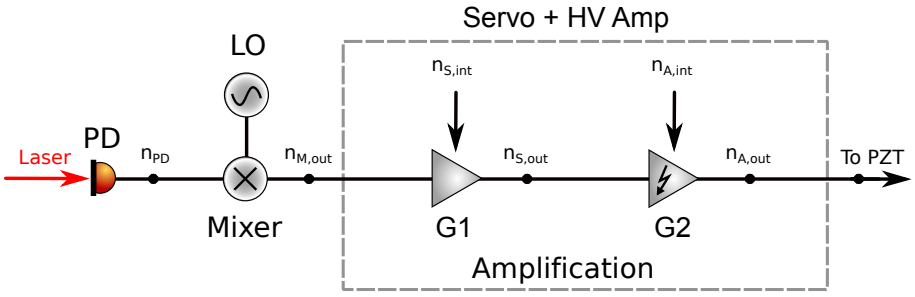

Figure 4.26: A part of the electrical loop of the Pound-Drever-Hall setup. The servo and the high-voltage amplifier supply tunable gains for amplifying the error signal.

A tunable amplifier usually consists of essentially a tunable attenuator followed by an amplifier with a fixed gain (see Figure 4.27). In other words, instead of been amplified directly, the signal is attenuated first. In this case, it is very important that the input noise of the amplifier should be smaller than the attenuated signal. For amplifiers with tunable gains, the input internal noise can be described by the

ratio of the output noise and its total gain:

$$n_{\text{int}} = \frac{n_{\text{out}}}{G}, \tag{4.19}$$

where the output noise n_{out} can be measured directly at its output port. In general it is desirable to design the loop so as to avoid using attenuators for as long as possible. We can achieve this by making sure that the tunable amplifier is operating most of the time at its maximum gain.

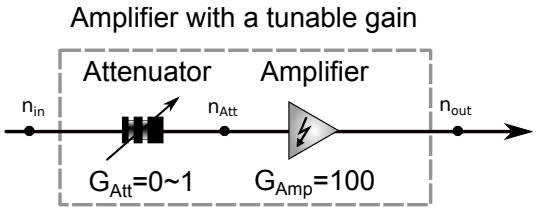

Figure 4.27: Configuration of an amplifier with a tunable gain, which can be regarded as two components: a tunable attenuator and an amplifier with a fixed gain. The final gain is $G_{\text{out}} = G_{\text{ATT}} G_{\text{Amp}}$.

The servo we use has a tunable gain from -40 dB to 20 dB and the high-voltage amplifier provides a voltage gain from 0 to 100. Their measured input internal noises are shown in Figure 4.25; they are both about $30\,\text{nV}_{\text{rms}}/\sqrt{\text{Hz}}$, which is about half of the photodetector's noise of $60\,\text{nV}_{\text{rms}}/\sqrt{\text{Hz}}$. In order to minimise the noise in the loop, the high-voltage amplifier operates close to its maximum gain of 100, and the servo should be operating with a gain above 14 dB.

Residual noise of the control loop

In Figure 4.14, we have shown the full loop of the Pound-Drever-Hall lock. A feedback signal is sent to the laser PZT to stabilise the laser frequency to the cavity length. The in-loop residual noise is usually measured at the error point e. The reason is that the error point is a null-detecting point where a good signal-to-noise ratio can be achieved easily and there is no risk of overloading the spectrum analyser used for the measurement. If the length equivalent noise n_{len} is injected at the virtual

adder box, the residual noise will be given by

$$n_{\text{in}} = \frac{n_{\text{err}}}{G_{\text{Cav}}} \quad \text{and} \quad n_{\text{in}} = \frac{1}{1 - G_{\text{OL}}} n_{\text{len}}, \tag{4.20}$$

where n_{err} is the noise measured at the error point when the loop is closed, n_{len} is the out-of-loop length equivalent noise and n_{in} is the in-loop residual noise.

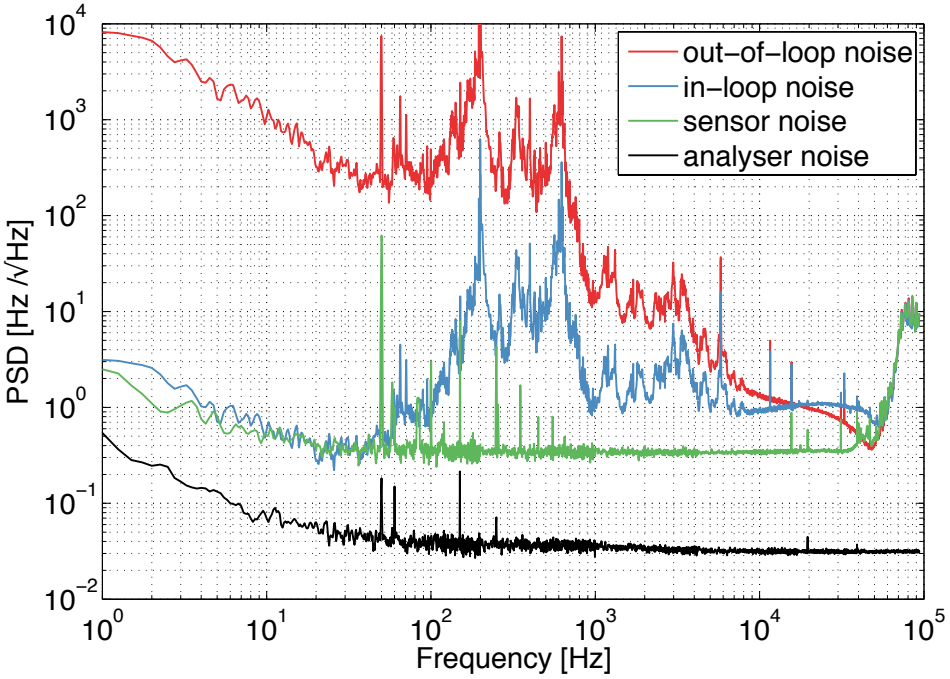

Figure 4.28: The residual noise and the free running noise of the system.

All length equivalent noises n_{len} can be converted to frequency noises n_f according to Equation 4.12. Figure 4.28 shows the measured frequency equivalent noises. We plot them as frequency noises because we want to compare them with the noise from our commercial laser, which is shown in Figure 4.8. From the comparison, we find that the noise in this system (the red curve) mainly comes from the laser frequency noise. Peaks between 100 Hz and 1 kHz are possibly due to mechanical resonances of mounts holding cavity mirrors. The in-loop noise below 100 Hz is strongly suppressed and limited by the sensor noise. The loop has a unity gain frequency between 10 kHz and 20 kHz where the in-loop noise and the open loop noise are cross one another. Above 50 kHz the noise floor is once again determined

by the sensor noise.

4.3 Frequency stabilisation of the probe laser

In the previous section, we described how the reference laser and the cavity have been stabilised relative to each other by the Pound-Drever-Hall technique. In this section, we are going to describe the stabilisation of the probe laser. These three devices (the cavity and the two lasers) will then all be locked together. Using the second laser, the probe laser, enables us to carry out a variety studies of the cavity, such as accurately measuring the free spectral range and the mode separation frequency, as well as mapping the higher order transverse modes.

The two commercial lasers have better noise performances than our 1 m cavity. It is therefore a natural idea to stabilise them all relative to one laser, in our case, the reference laser. This acts as a frequency reference for the probe laser, and as a length reference for the 1 m cavity. In this configuration, an external PZT is used to actuate microscopic positions of one mirror in the 1 m cavity to compensate its length fluctuations. The length noise of the cavity is then reduced to a level close to the laser frequency noise (especially at low frequencies). However, we find that there are two practical problems in locking our cavity to the reference laser. 1) The external PZTs we use all have resonant frequencies around 15 kHz, which is close to the unity gain frequency of the current Pound-Drever-Hall loop. Resonances near the unity gain frequency can become excited and potentially grow large enough to drive the cavity out of lock. In order to achieve a stable loop, the loop-gain should be reduced by a certain factor. 2) The cavity has a finesse of approximately 2000, and hence a narrow linewidth, leading to a small dynamic range. The length noise induced deviation can easily drive the operating point out of the dynamic range. In practice, this makes the cavity difficult to lock initially, and to maintain locked. To increase the dynamic range of the system, a higher gain is usually required. This will then increase the probability of exciting resonances, as described in 1).

Because of the problems above, we choose to actuate on the reference laser PZT to lock this to the cavity, as the resonant frequency of the integrated PZT in the laser is much higher (above 30 kHz) than the cavity PZTs. The frequency of the reference laser then follows the length fluctuations of the cavity. To stabilise the probe laser, a phase locking loop is introduced that stabilises the frequency difference between the reference laser and the probe laser so that the latter also follows the noise of the cavity. By doing this, we ensure that the probe laser remains 'relatively' stable with respect to the cavity. Unfortunately, we cannot use the phase locking loop directly because the cavity is free running and the noise introduced to the reference laser in the Pound-Drever-Hall loop is beyond the dynamic range of the phase locking loop. To enable the phase locking loop to work properly, we must first reduce the noise between the probe laser and the cavity to an acceptable level. This is achieved by splitting the Pound-Drever-Hall signal fed to the reference laser and sending it also to the probe laser. In the following sections, we will first introduce the split feedback loop for the probe laser, and then introduce the phase locking technique that stabilises the frequency difference between the two lasers.

4.3.1 Split feedback loop

The aim of the split feedback loop is to ensure that the two PZTs in the two different lasers produce the same change in frequency, given the same feedback signal. The gain of the integrated PZT in the probe laser is measured to be approximately 1.75 MHz/V according to the method introduced in Section 4.2.3. It is about 1.5 times larger than the gain of the PZT for the reference laser. So we use a tunable amplifier (attenuator) in the split feedback loop to the probe laser. Figure 4.29 shows a schematic of the control loops.

The two lasers are both aligned to the 1 m cavity but have orthogonal polarisations so that they don't interfere with one another. In the Pound-Drever-Hall loop stabilising the reference laser (s-polarise), the feedback signal is split after the servo and fed to the probe laser (p-polarised) via a tunable amplifier. In order to find the optimum

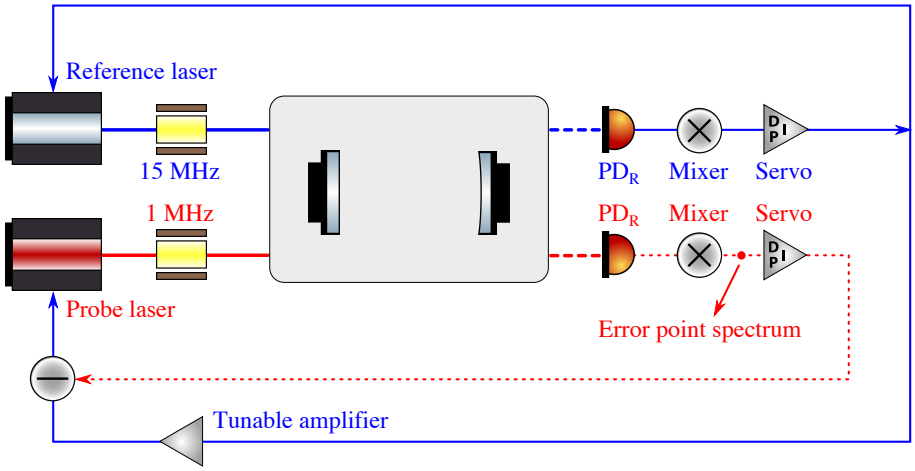

Figure 4.29: The split feedback loop used to stabilise the frequency of the probe laser. A split feedback signal from the loop of the reference laser is sent to the probe laser. A second Pound-Drever-Hall loop is set up for the probe laser to measure the residual perturbation between it and the cavity. Note that this figure doesn't present the correct arrangements for all optical components. These details can be found in Figure 4.4.

gain for the tunable amplifier, we set up another Pound-Drever-Hall loop which is able to directly lock the probe laser to the cavity. The feedback signal in this loop is subtracted from the split feedback signal from the reference laser loop. The residual noise between the probe laser and the cavity can be measured at the error point in the probe laser loop. It is monitored on a spectrum analyser while the gain of the amplifier is adjusted. The residual noise should minimised if the two split loops have exactly the same gain. Figure 4.30 shows the measured residual noise between the probe laser and the cavity. The red curve shows the calibrated out-of-loop frequency noise (the free running noise) between the probe laser and the cavity without any stabilisation, which has a similar shape to the noise shown in Figure 4.28. The reduction in noise between 100 Hz and 300 Hz is due to the mirror mounts being replaced by more stable ones, which did not exhibit such large mechanical resonances. The blue curve is the residual noise after the probe laser is locked to the cavity by closing the red dashed loop shown in Figure 4.29, while the reference laser loop is open. Peaks between 200 Hz and 600 Hz are mainly due to mechanical resonances of cavity mirror mounts. The green curve shows the residual noise after we lock the reference laser and feed the split signal to the probe laser with

the optimum gain. The split feedback loop actually acts as a feed-forward system where common-mode noise due, for instance, to resonances of mirror mounts, is reduced.

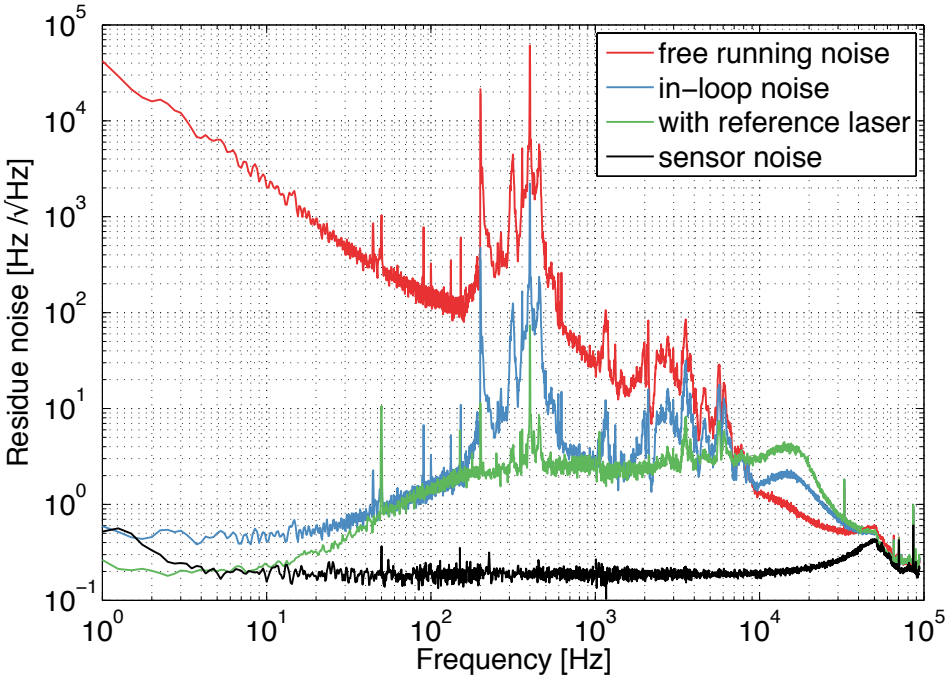

Figure 4.30: The residue noise between the probe laser and the cavity.

4.3.2 Offset phase lock of the two lasers

The split feedback loop reduces frequency fluctuations between the probe laser and the reference laser to a sufficiently low level that the phase lock between the two lasers can be implemented. Fluctuations are then further suppressed by the phase locking loop. Most importantly, we use an offset phase locking technique that enables us to tune the DC frequency difference between two lasers to a specified value. Figure 4.31 shows the schematic of the setup whereby the offset phase locking loop is applied.

The two laser beams are combined together at the central beam splitter. If we

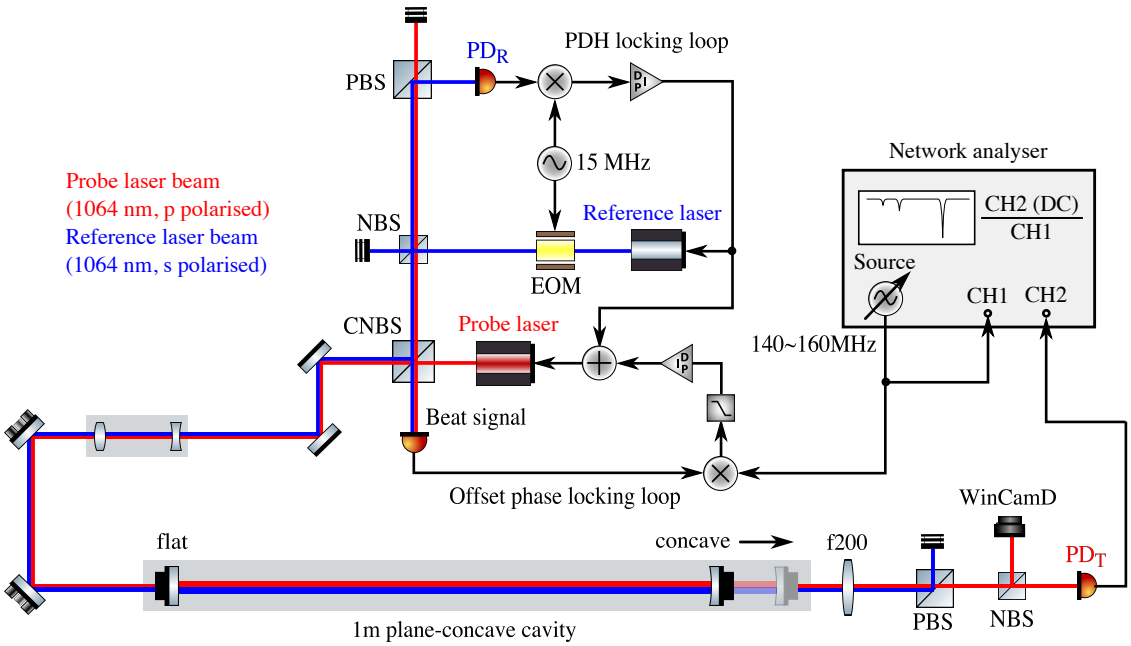

Figure 4.31: The schematic of the offset phase locking system.

assume that the reference laser produces a field

$$E_1 = E_0 e^{i(\omega_0 t + \varphi_0)}, \tag{4.21}$$

and the probe laser produces a filed

$$E_2 = A E_0 e^{i[(\omega_0 + \Delta\omega)t + (\varphi_0 + \Delta\varphi)]}, \tag{4.22}$$

where A is the ratio of amplitudes between the two fields, $\Delta\omega$ is the frequency difference between the two lasers and $\Delta\varphi$ is the phase difference at the combination point. The combined beam is just

$$E_c = E_1 + E_2 = E_0 e^{i(\omega_0 t + \varphi_0)} \left(1 + A e^{i(\Delta\omega t + \Delta\varphi)}\right). \tag{4.23}$$

The combined field is detected with a high speed photodetector whose output is the

power of the field

$$\begin{aligned} P_c = E_c E_c^* &= E_0^2 \left(2 + A e^{i(\Delta\omega t + \Delta\varphi)} + A e^{-i(\Delta\omega t + \Delta\varphi)}\right) \\ &= 2E_0^2 \left[1 + A\cos\left(\Delta\omega t + \Delta\varphi\right)\right]. \end{aligned} \tag{4.24}$$

The output signal is then demodulated at frequency ω_x, giving a signal

$$\begin{aligned} S_{\text{dem}} =& P_c \sin\left(\omega_x t + \varphi_x\right) \\ =& 2E_0^2 \left[1 + A\cos\left(\Delta\omega t + \Delta\varphi\right)\right] \sin\left(\omega_x t + \varphi_x\right) \\ =& 2E_0^2 \sin\left(\omega_x t + \varphi_x\right) + AE_0^2 \sin\left[\left(\Delta\omega + \omega_x\right) t + \left(\Delta\varphi + \varphi_x\right)\right] \\ & - AE_0^2 \sin\left[\left(\Delta\omega - \omega_x\right) t + \left(\Delta\varphi - \varphi_x\right)\right] \end{aligned} \tag{4.25}$$

where ω_x is the demodulation frequency and φ_x is the demodulation phase. If we tune the frequency of the probe laser so that the frequency difference between the two laser fields is close to the demodulation frequency, i.e., $\Delta\omega \approx \omega_x$, the third term in Equation 4.25 will become a very low frequency, or in the ideal case, a DC component, while the first two terms are high-frequency oscillating components, which can be removed by a low-pass filter ($f_p \ll \omega_x$). This leaves only the third term, giving the signal:

$$S_{\text{dem, DC}} = -AE_0^2 \sin\left[\left(\Delta\omega - \omega_x\right) t + \left(\Delta\varphi - \varphi_x\right)\right], \tag{4.26}$$

which gives the error signal of the phase locking loop. In this case, the frequency of the probe laser is held adjusted such that $\Delta\omega = \omega_x$. As the frequency difference is determined by a signal generator, this can be continuously adjusted while keeping one laser locked to the cavity.

The offset phase locking technique enables us to carry out a variety of measurements with the probe laser. For example, the reference laser can be kept locked to one resonance of the cavity, while we scan the frequency of the probe laser to find the next resonance point corresponding to the same mode. Hence, the free spectral range of the cavity can be accurately measured. We can also inject higher order

mode contents with the probe laser, and measure the mode separation frequency or observe their transmitted shapes. A camera is placed at the cavity's transmission port to observe the shape of the resonant mode. These measurements are described in more detail in the next chapter.

4.4 Alignment control

In gravitational wave detectors, longitudinal motions of arm cavity mirrors can be precisely measured and controlled by the Pound-Drever-Hall locking technique. Angular motions of cavity mirrors are generally harder to measure. These can cause misalignments in axes between optical cavities and incoming beams. The misalignment usually results in the fundamental mode coupled to higher order modes. This can cause problems in the interferometer control as well as reducing the optical contrast detected by the photodetector, decreasing the interferometer's sensitivity [116]. Thus angular motions of all mirrors must be controlled in the interferometer.

In the Birmingham tabletop setup, we have implemented an alignment control system for the 1 m cavity based on the wavefront sensing technique proposed by Anderson [117, 118, 119], in which transverse modes are used for detecting misalignments. This alignment control system produces an error signal directly proportional to the magnitude of misalignments of the cavity. We use this system because it enables the cavity to be aligned more accurately to the probe laser when pushed to the near unstable region than would be possible by, for instance, simply measuring the offset of the reflected or transmitted beams with a camera. Most importantly, it ensures that the alignment of the cavity is kept the same when its configuration is changed to alter the stability.

4.4.1 Misalignments of a hemispherical cavity

A cavity is aligned when the optical axis of its eigenmodes exactly overlaps with the optical axis of the incoming beam. Misalignments can be described by the *translation* and *tilt angle* between the two optical axes. In a hemispherical cavity the translation Δx and tilt angle θ are determined by the tilt angle of the input mirror and the end mirror, α and β [118] (see Table 4.6). Tilt of the plane input mirror will introduce both translation and tilt angle to the cavity's optical axis while the tilt concave end mirror only introduces translation.

Table 4.6: Tilts of plane-concave cavity mirrors coupled to cavity axis misalignments.

	IM(plane) tilt α	EM(concave) tilt β
Translation Δx	$(R_C - L)\sin\alpha$	$R_C \sin\beta$
Tilt angle θ	α	0

4.4.2 Influence of misalignments to transverse modes

The transverse profile of the electromagnetic field of a laser beam can be written using the orthogonal set of so-called *Hermite-Gaussian modes*:

$$\begin{aligned} u_{nm}(x,y,z) =& u_n(x,z)\cdot u_m(y,z) \\ =& (2^{n+m-1}n!m!\pi)^{-1/2}\frac{1}{w(z)}\exp\left[i(n+m+1)\Psi(z)\right] \\ & \cdot H_n(\frac{\sqrt{2}x}{w(z)})H_m(\frac{\sqrt{2}y}{w(z)})\exp\left[-i\frac{k(x^2+y^2)}{2R_C(z)}-\frac{x^2+y^2}{w^2(z)}\right], \end{aligned} \tag{4.27}$$

with

$$u_n(x,z) = (\frac{2}{\pi})^{1/4}\left[\frac{\exp\left[i(2n+1)\Psi(z)\right]}{2^n n! w(z)}\right]^{1/2} H_n(\frac{\sqrt{2}x}{w(z)})\exp\left[-i\frac{kx^2}{2R_C(z)}-\frac{x^2}{w^2(z)}\right], \tag{4.28}$$

where $H_n(x)$ is the Hermite polynomial of order n. At beam waist, we have $z = 0$, $R_c(0) \to \infty$ and Gouy phase $\Psi(0) = 0$, so $n = 0$ and $n = 1$ give expressions of the

fundamental mode and the first order mode respectively,

$$u_0(x) = (\frac{2}{\pi w_0^2})^{1/4} \exp\left(-\frac{x^2}{w_0^2}\right), \tag{4.29}$$

and

$$u_1(x) = (\frac{2}{\pi w_0^2})^{1/4} \frac{2x}{w_0} \exp\left(-\frac{x^2}{w_0^2}\right). \tag{4.30}$$

Effect of cavity axis translation

When there is a translation Δx (assuming $\Delta x \ll w_0$) between the incident beam axis and the cavity axis, we can write the mode leaking from the cavity as

$$\begin{aligned} u_0(x-\Delta x) &= (\frac{2}{\pi w_0^2})^{1/4} \exp\left[-\frac{(x-\Delta x)^2}{w_0^2}\right] \\ &\approx (\frac{2}{\pi w_0^2})^{1/4} \exp\left(-\frac{x^2}{w_0^2} + \frac{2x\Delta x}{w_0^2}\right) \quad .] \\ &= (\frac{2}{\pi w_0^2})^{1/4} \exp\left(\frac{2x\Delta x}{w_0^2}\right) \exp\left(-\frac{x^2}{w_0^2}\right). \end{aligned} \tag{4.31}$$

By using Taylor expansion, we have

$$\exp\left(\frac{2x\Delta x}{w_0^2}\right) = 1 + \frac{2x\Delta x}{w_0^2} + \frac{1}{2}\left(\frac{2x\Delta x}{w_0^2}\right)^2 + \cdots . \tag{4.32}$$

In the region where $x \leq w_0$, $2x\Delta x/w_0^2 \ll 1$, we have

$$\begin{aligned} u_0(x-\Delta x) &\approx (\frac{2}{\pi w_0^2})^{1/4} \left(1 + \frac{2x\Delta x}{w_0^2}\right) \exp\left(-\frac{x^2}{w_0^2}\right) \\ &= u_0(x) + \frac{\Delta x}{w_0} u_1(x) \end{aligned} \tag{4.33}$$

The translation of optical axis introduces the first order mode and the coupling factor is proportional to the beam translation.

In the region where $x > w_0$, we have $x \gg \Delta x$ and $u_0(x-\Delta x) \approx u_0(x)$. The beam profile doesn't change.

The second term in Equation 4.32 represents the second order mode which is very

small, so we can write the field as

$$u_0(x - \Delta x) = u_0(x) + \frac{\Delta x}{w_0} u_1(x) + o\left(u_2(x)\right) + \cdots . \tag{4.34}$$

Figure 4.32 shows a schematic of the principle whereby beam translation couples the fundamental mode to the first order mode. Blue curves represent the beam directly reflected by the flat input mirror. Pink curves represent the anti-resonant beam reflected by the cavity. There is a phase difference of 180° between the two beams. When their amplitudes are added together, they form the profile of the first order mode.

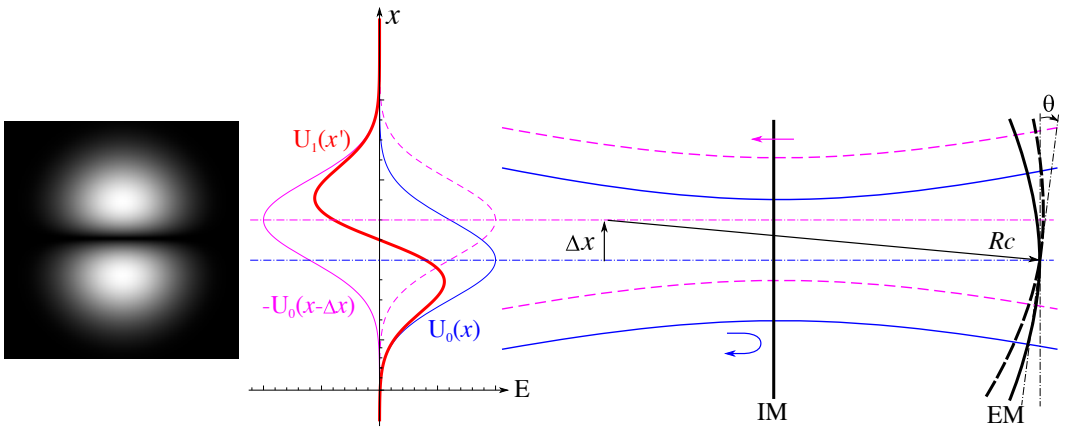

Figure 4.32: Schematic of the principle by which the fundamental mode is coupled to the first order mode by translation of the cavity axis.

Effect of cavity axis tilt

Near the centre of the beam profile, a small tilt in the axis of a Gaussian beam can be seen as an additional, transverse position-dependent phase added to the original beam (see the left plot in Figure 4.33). For a small tilt angle θ, the phase difference between the tilt plane and the original plane is $\varphi = 2\pi x \sin\theta/\lambda$. So the tilted beam

can be written as

$$\begin{aligned} u(x)_{\text{tilt}} &= u_0(x)\exp(i\varphi) = u_0(x)\exp\left(\frac{i2\pi x\sin\theta}{\lambda}\right) \\ &= u_0(x)\left[\cos\left(\frac{2\pi x\sin\theta}{\lambda}\right) + i\sin\left(\frac{2\pi x\sin\theta}{\lambda}\right)\right] \\ &\approx u_0(x)\left(1 + \frac{i\pi w_0\theta}{\lambda}\frac{2x}{w_0}\right) \\ &= u_0(x) + \frac{i\pi w_0\theta}{\lambda}u_1(x) \\ &= u_0(x) + i\frac{\theta}{\theta_{\text{div}}}u_1(x), \end{aligned} \tag{4.35}$$

where we define $\theta_{\text{div}} = \lambda/(\pi w_0)$ to be the divergent angle of a Gaussian beam.

From Equation 4.35, we can see that the tilt of cavity axis also couples the fundamental mode to the first order mode. However, the resultant first order mode has a phase shift of 90° relative to the original beam. The right-hand plot in Figure 4.33 shows the complex amplitude of the original beam and of the tilted beam. If the amplitude of the original fundamental beam is purely real, the resulting tilted beam has the profile of the first order mode and is mainly imaginary, with a phase shift of close to 90°.

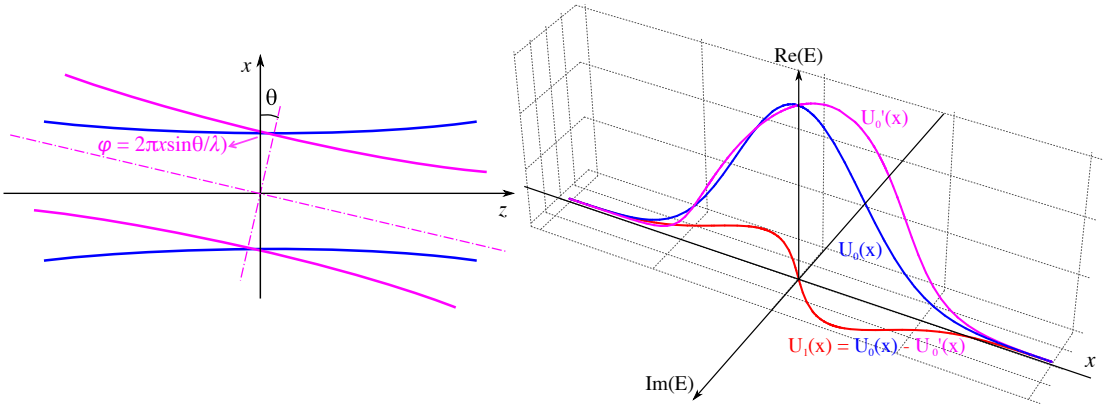

Figure 4.33: Principle by which the fundamental mode couples to the first order mode due to cavity axis tilt.

Table 4.7 gives a summary of the coupling coefficients. We use a complex coupling coefficient which is

$$C = \frac{\Delta x}{w_0} + i\frac{\theta}{\theta_{\text{div}}}. \tag{4.36}$$

Table 4.7: Mode coupling coefficient from the fundamental mode to the first order mode due to cavity axis misalignments.

	coupling coefficient	phase
Translation Δx	$\Delta x/w_0$	$0°$
Tilt θ	$i\pi w_0\theta/\lambda$	$90°$

4.4.3 Creating error signal for the alignment system

As with the Pound-Drever-Hall laser frequency stabilisation technique, the alignment control system also uses a modulation and demodulation scheme to create a phase-sensitive error signal. The incident beam from the probe laser is modulated at 1 MHz. The beat signal caused by interference between the fundamental mode and the first order mode reflected by the cavity, contains the information giving both the magnitude and direction of misalignments. This is detected by the photodetector.

The incoming beam from the laser can be written as

$$E_{\text{in}} = E_0 u_0 \exp(i\omega_0 t). \tag{4.37}$$

The phase modulation generates two sidebands around the carrier. The incoming light field can be written as

$$E_{\text{in}} = E_0 u_0 \exp(i\omega_0 t)\left[1 + i\frac{m}{2}\exp(-i\omega_{\text{m}} t) + i\frac{m}{2}\exp(i\omega_{\text{m}} t)\right], \tag{4.38}$$

where ω_m is the modulation frequency. This alignment system works only when the cavity length is stabilised to the laser frequency and vice versa. In this case, the carrier frequency ω_0 is the only resonant term inside the cavity. If it is an over-coupled cavity, the reflected beam at the carrier frequency will have a phase shift of 180° compared to the anti-resonant beam. Describing the cavity misalignment by the complex coupling coefficient, C, introduced above, the total reflected field is

found to be

$$\begin{aligned} E_{\mathrm{R}} =& E_0 u_0 \exp(i\omega_0 t)\left[-1 + i\frac{m}{2}\exp(-i\omega_{\mathrm{m}}t) + i\frac{m}{2}\exp(i\omega_{\mathrm{m}}t)\right] \\ &+ E_0 C u_1 \exp(i\Psi)\exp(i\omega_0 t) \\ =& E_0 u_0 \left[a_0\exp(i\omega_0 t) + a_1\exp(i(\omega_0-\omega_{\mathrm{m}}t)) + a_2\exp(i(\omega_0+\omega_{\mathrm{m}}t)) + a_3\exp(i\omega_0 t)\right], \end{aligned} \tag{4.39}$$

where

$$\begin{aligned} a_0 &= -1, \\ a_1 &= a_2 = i\frac{m}{2}, \\ a_3 &= \frac{2x}{w_0}Ce^{i\Psi}, \end{aligned} \tag{4.40}$$

and Ψ is the Gouy phase between the fundamental mode and the first order mode at the detection port. In Equation 4.39, the first term is the component of the resonant carrier beam reflected by the cavity, which has a phase shift of 180°. The second and third terms correspond to upper and lower sidebands which are anti-resonant and reflected by the cavity. The fourth term is the component of the beam introduced by misalignments.

The total reflected field is detected using a photodiode. The light field on this photodiode can be written as

$$S_{\mathrm{PD}} = \int_{-\infty}^{+\infty} E_{\mathrm{R}} E_{\mathrm{R}}^* \mathrm{d}x = \int_{-\infty}^{+\infty} E_0^2 u_0^2 \sum_{i=0}^{3}\sum_{j=0}^{3} a_i a_j^* \exp(i(\omega_i-\omega_j)t)\mathrm{d}x \tag{4.41}$$

Then the signal is demodulated at frequency ω_{dem} with a mixer, to give a signal:

$$S'_{\mathrm{PD}} = \int_{-\infty}^{+\infty} E_0^2 u_0^2 \sum_{i=0}^{3}\sum_{j=0}^{3} a_i a_j^* \exp(i(\omega_i-\omega_j)t)\mathrm{d}x \cdot \cos(\omega_{\mathrm{dem}}t + \varphi_{\mathrm{dem}}), \tag{4.42}$$

where ω_{dem} is the demodulation frequency and φ_{dem} is the demodulation phase. A low-pass filter is applied as we are only interested in the DC component, which is

given by:

$$S'_{\text{PD, DC}} = \int_{-\infty}^{+\infty} E_0^2 u_0^2 \sum_{i=0}^{3}\sum_{j=0}^{3} \text{Re}(a_i a_j^* e^{-i\varphi_{\text{dem}}}) \text{d}x, \quad \text{where} \quad \omega_i - \omega j = \omega_{\text{dem}}. \tag{4.43}$$

If the demodulation frequency is equal to the modulation frequency, i.e. $\omega_{\text{dem}} = \omega_{\text{m}}$, we have

$$S'_{\text{PD, DC}} = \int_{-\infty}^{+\infty} E_0^2 u_0^2 \text{Re}\left[(a_0 a_1^* + a_2 a_0^* + a_3 a_1^* + a_2 a_3^*) e^{-i\varphi_{\text{dem}}}\right] \text{d}x. \tag{4.44}$$

In order to remove the contribution of the carrier filed, we use a *split photodetector* in order to extract the component of the light containing the first order mode. The split photodiode output signal is connected to a differential output circuit, giving a signal proportional to the difference in the light intensity on its two split detectors. Similarly, to detect misalignments in pitch and yaw directions we use a *quadrant photodiode* (QPD). If we consider a split diode whose two detectors are split in x direction (split by y axis), and suppose that the beam is incident symmetrically on the split photodiode, the output signal is

$$\begin{aligned} S_{\text{QPD}} &= \int_{-\infty}^{0} EE^* \text{d}x - \int_{0}^{+\infty} EE^* \text{d}x \\ &= \begin{cases} 0, & a_i a_j \text{ is even}, \\ -2\displaystyle\int_0^{+\infty} E_0^2 u_0^2 \sum_{i=0}^{3}\sum_{j=0}^{3} \text{Re}(a_i a_j^* e^{-i\varphi_{\text{dem}}}) \text{d}x, & a_i a_j \text{ is odd}, \end{cases} \end{aligned} \tag{4.45}$$

This means the $a_i a_j^*$ in Equation 4.41 can only contribute to the output signal when it is an odd function. As a_0, a_1 and a_2 are all even functions, only terms containing

a_3 in Equation 4.44 will remain:

$$\begin{aligned}
S'_{\text{QPD, DC}} &= -2\int_0^{+\infty} E_0^2 u_0^2 \text{Re}\left[(a_3 a_1^* + a_2 a_3^*) e^{-i\varphi_{\text{dem}}}\right] \text{d}x \\
&= 2E_0^2 \int_0^{\infty} \text{Re}\left(im\frac{x}{w_0} u_0^2 \left[Ce^{i\Psi} - (Ce^{i\Psi})^*\right] e^{-i\varphi_{\text{dem}}}\right) \text{d}x \\
&= 2E_0^2 \frac{m}{w_0} \text{Re}\left\{i\left[Ce^{i\Psi} - (Ce^{i\Psi})^*\right] e^{-i\varphi_{\text{dem}}}\right\} \int_0^{\infty} x \exp\left(-\frac{2x^2}{w_0^2}\right) \text{d}x \\
&= \frac{1}{2} E_0^2 m w_0 \text{Re}\left\{i\left[Ce^{i\Psi} - (Ce^{i\Psi})^*\right] e^{-i\varphi_{\text{dem}}}\right\} \\
&= -E_0^2 m w_0 \text{Re}\{[\text{Re}(C)\sin\Psi + \text{Im}(C)\cos\Psi](\cos\varphi_{\text{dem}} - i\sin\varphi_{\text{dem}})\} \\
&= -E_0^2 m w_0 \left(\frac{\Delta x}{w_0}\sin\Psi + \frac{\theta}{\theta_{\text{div}}}\cos\Psi\right)\cos\varphi_{\text{dem}}.
\end{aligned} \tag{4.46}$$

The demodulation phase φ_{dem} is adjusted to match with the modulation phase, so that $\cos\varphi_{\text{dem}} = 1$. The magnitude of the demodulated signal is proportional to the a linear combination of the of translation and tilt of the cavity axis relative to the incoming beam.

4.4.4 QPD telescope design

From Equation 4.46, we see that we cannot separate the translation from the tilt signal using just one QPD. In general, therefore, two QPDs must be used, such that the accumulated Gouy phase of the beam on one QPD is different from that on the other one. This can be achieved by applying a telescope before each QPD. The Gouy phase difference is usually chosen as 90°, in order to optimally separate the two signals.

Figure 4.4 shows the layout of the QPD telescopes in our setup. The beam reflected by the cavity is picked off after propagating back through the mode matching lens group. This makes the alignment control system independent to the mode matching system; that is, the configuration of the cavity or the mode matching lens group should be independent of the profiles of the reflected beam incident on two QPDs.

Figure 4.34 and Figure 4.35 show the telescope parameters used to provide the 90° Gouy phase shift between the two QPDs. The accumulated phase is calculated starting from position of the waist of the reflected beam from the cavity (marked as two w_0 planes in Figure 4.4). We denote the accumulated Gouy phase at QPD1 as written as Ψ. The Gouy phase at QPD2 then should be $(\Psi + 90°)$. Then outputs out the two QPDs are

$$\begin{cases} S'_{\text{QPD1, DC}} = -E_0^2 m w_0 \left(\dfrac{\Delta x}{w_0} \sin\Psi + \dfrac{\theta}{\theta_{\text{div}}} \cos\Psi \right) \\ S'_{\text{QPD2, DC}} = -E_0^2 m w_0 \left(\dfrac{\Delta x}{w_0} \cos\Psi - \dfrac{\theta}{\theta_{\text{div}}} \sin\Psi \right) \end{cases} \tag{4.47}$$

We can now keep the cavity aligned such that both Δx and θ are zero, by adjusting the alignment to make sure that outputs from the two QPDs are both zero.

$$\begin{cases} -E_0^2 m w_0 \left(\dfrac{\Delta x}{w_0} \sin\Psi + \dfrac{\theta}{\theta_{\text{div}}} \cos\Psi \right) = 0 \\ -E_0^2 m w_0 \left(\dfrac{\Delta x}{w_0} \cos\Psi - \dfrac{\theta}{\theta_{\text{div}}} \sin\Psi \right) = 0 \end{cases} \Rightarrow \begin{cases} \Delta x = 0 \\ \theta = 0 \end{cases} \tag{4.48}$$

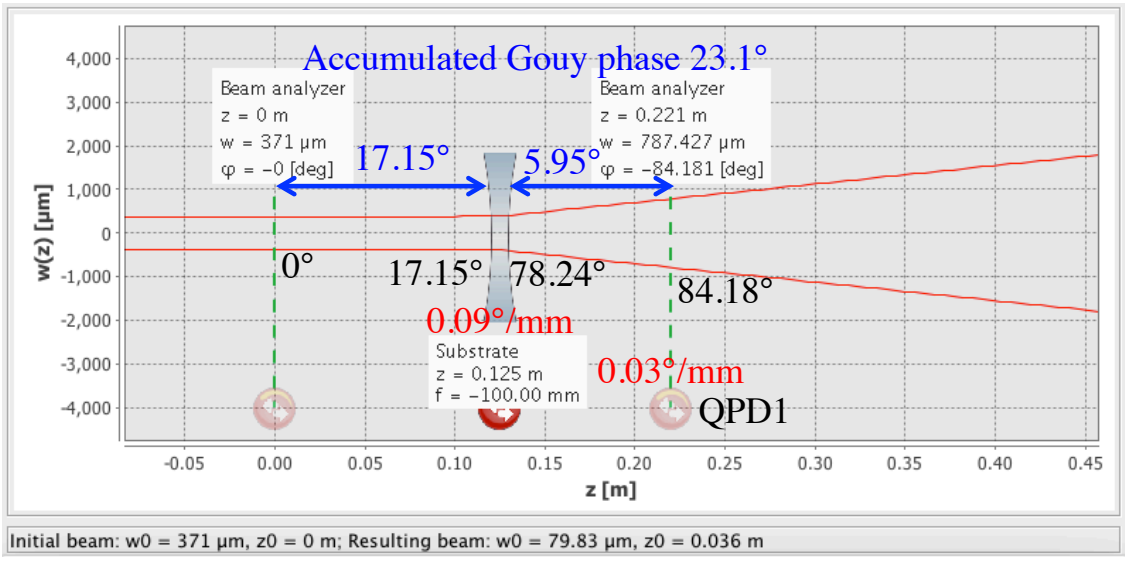

Figure 4.34: The telescope for QPD1.

By observing error signals from the two QPDs on an oscilloscope, it can be ensured that the probe laser is always aligned to the cavity after we have moved the telescope

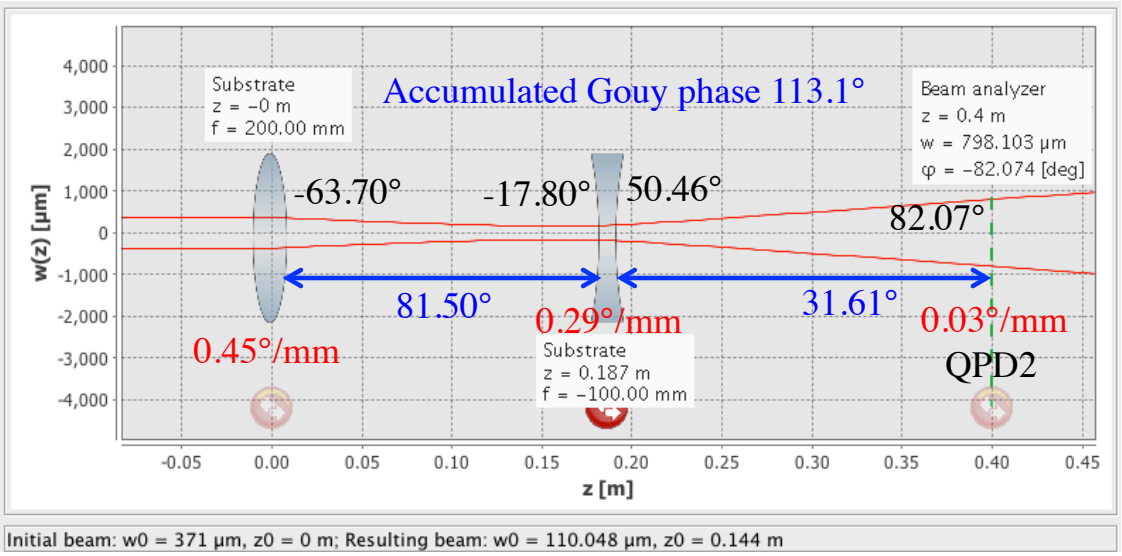

Figure 4.35: The telescope for QPD2.

to adjust the cavity's stability.

4.4.5 Closed the loop: automatic alignment system

The error signals for misalignment, described in the previous section, can be used in 'open loop' mode for one-off alignment operation. It can also be fed back into an automated alignment system, if the angular degrees of freedom of steering mirrors are electronically controlled. This automatic alignment system can help us reduce fluctuations in the angular alignment of the cavity mirrors relative to the incoming beam. It should be noted, however, that this readout mechanism only works when the beam from the probe laser is resonant or close resonant in the cavity.

Here we feed the signal to two steering mirrors before the cavity to control the alignment of the incoming beam. An alternative would be to instead feed back to the cavity mirrors, but this would introduce additional noise into the cavity. Two two-axis PZT actuators are used to control the degrees of freedom of the two steering mirrors. Each actuator has two inputs, Ax and Ay, which can change the tilt angle of the steering mirror in the yaw and pitch direction, respectively. Altering the yaw of the steering mirror will cause a change in the QPD's output differential signal

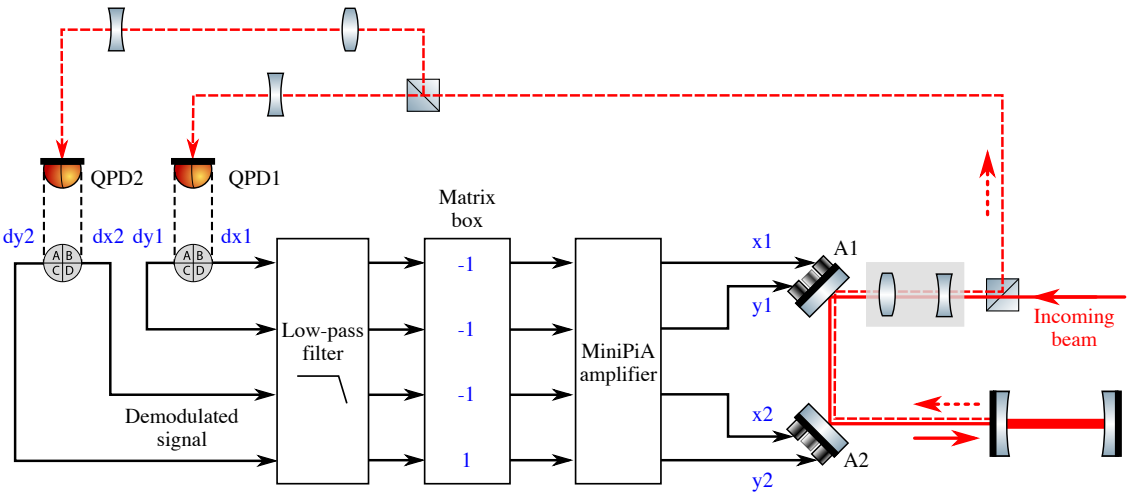

Figure 4.36: Schematic of the auto-alignment system.

dx, while the pitch of the mirror corresponds to the output dy. Outputs of the two QPDs are negatively fed back to the two actuators through an electronic servo system comprising some filters and ampliersas shown in Figure 4.36.

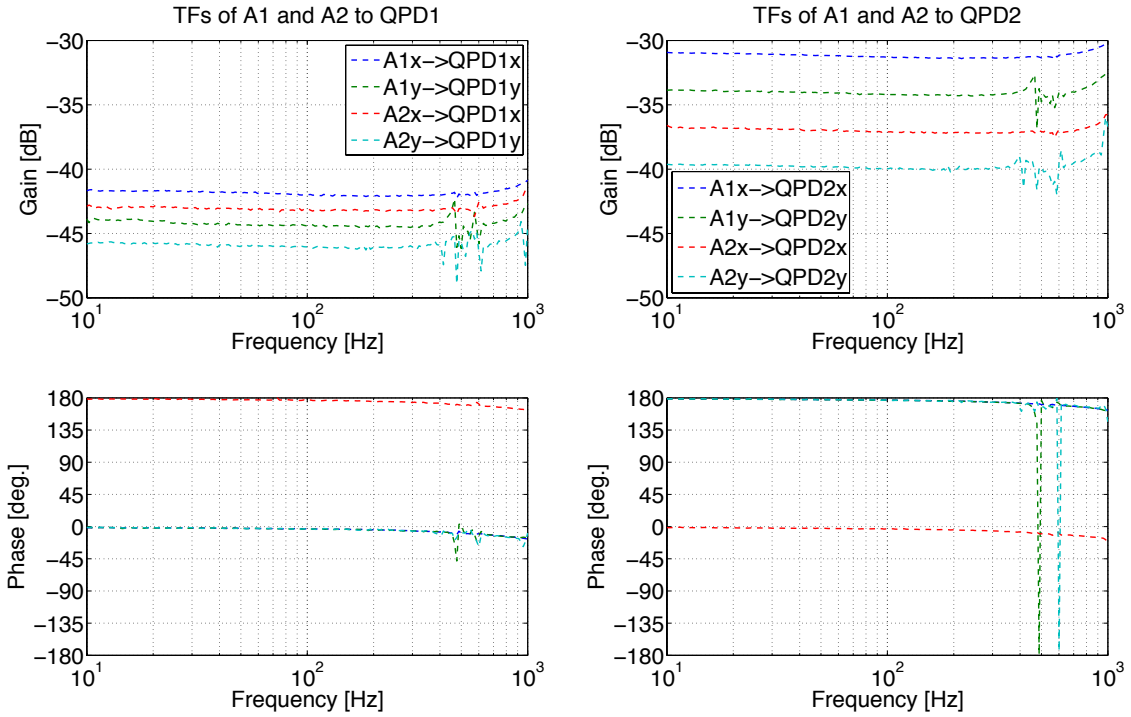

Figure 4.37: Transfer functions measured for actuators and QPDs.

Figure 4.37 shows the measured open loop transfer functions of the actuators associated with the two QPDs. The test signal is injected to one of the four input ports

of the two actuators and at each time outputs of the two QPDs are measured correspondingly. We can see the Actuator 1 (A1) creates a larger gain than A2 because it is further away from the cavity. QPD2 has a larger sensing gain than QPD1, which is determined by the Gouy phase difference between the actuators and the QPDs (supposing electronic gains of the two QPDs are the same). In our setup, the two actuators both change the translation and tilt of the incoming beam with respect to the cavity axis because their Gouy phases are neither 0 or 90°. There must be an actuator acting as the main one and the other one is associate. Usually, the loop which has a larger gain is used as the main actuating loop.

Currently, the alignment system is mainly used in the open loop where its error signals help us align the cavity accurately. But with the auto-alignment system, in the future we want to study the the alignment noise coupling and the potential control problems when the cavity is pushed to the near-unstable region.

4.5 Conclusion

This Chapter mainly describes the setting up and characterisation of the table-top experiment to investigate technical hurdles of NUCs. The setup comprises an approximately 1 m long plane-concave cavity, whose length can be incrementally changed to explore the boundary of the stability region. The cavity is built on an optical bench with careful mode matchings, and accurately controlled with a length stabilisation system. The offset phase locking scheme which controls the frequency difference between two lasers enables precise measurements to be carried out in the near-unstable region. An alignment system is used to keep the mirrors aligned when we change the cavity stability. Experimental work has been carried out to make these systems robust and reliable, and to optimise the performance of these precise control systems.

Chapter 5

Exploring near-instability

In this chapter, we investigate behaviour of the 1 m tabletop cavity when pushing its stability to extreme conditions. The two main purposes of this experiment are to find out how cavity eigenmodes behave in a practical setup and to determine how far we can push the cavity towards stability edge before the cavity becomes no longer practically usable, due to either optical losses, or cross-talk between control signals.

As introduced in Section 1.7, thermal compensation of near-unstable recycling cavities in Advanced Virgo is very difficult. Mode couplings between imperfect mirror surfaces can be quite chaotic given a small deformation. A study of mode pattern changes in NUCs would help quickly distinguish if the cavity is stable or unstable. More specifically, a method of accurately quantifying cavity g-factors can give very solid guidelines for the TCS to control the cavity stability, thus help the interferometer operate at its maximum gain.

For future detectors, finding the practical boundary of NUCs can provide insights into how far the cavity parameters can be pushed towards geometrical instability, as well as difficulties that need to be overcome in order to achieve optimal operation. A good knowledge of mode degeneracies in NUCs due to mirror imperfections can also help design mirror specifications.

The tabletop experiment performed here is also aimed at providing guidelines for the future prototype experiments that will be carried out in the near future. Results from this chapter have been summarised in a paper and will be submitted for publication.

5.1 Measuring mode separation frequency

With all the control and measurement subsystems set up correctly, the 1 m plane-concave cavity is initially operated in a relatively stable region with a g-factor around 0.044, as shown in Table 4.1. We then incrementally approach a near-unstable configuration with $g_c = 0.0001$ or further. This approach towards the boundary of stability is carried out by changing the cavity length, as replacing cavity mirrors with others with the same reflectivity but different ROCs would be very costly. Figure 5.1 shows a picture of the practical setup including all the subsystems.

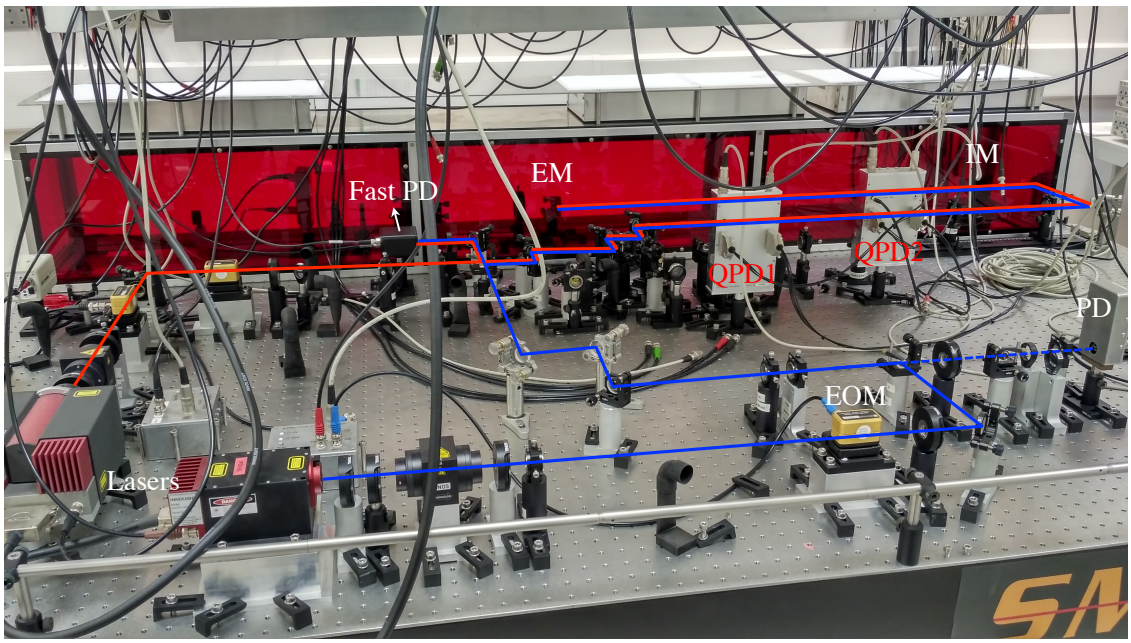

Figure 5.1: Photo of the tabletop setup. Two commercial Mephisto lasers are in the bottom left whose beam paths are labelled in red and blue for the probe laser and the reference laser respectively. The cavity is contained in a box (the red box in the figure) which reduces air flow between the two cavity mirrors and makes the frequency stabilisation control loops more stable.

In order to gradually change the cavity length, the end mirror of the cavity is mounted on a linear translation stage (M-460A) from Newport with a differential micrometer (DM-13) which enables us to control the position with a precision up to 0.5 μm. Figure 5.2 shows a picture of the end mirror, the translation stage and devices at the transmission port. A two-inch lens with a focal length of +200 mm is placed after the end mirror to focus the strongly diverging transmitted beam, delivering the field to a camera and a photodetector.

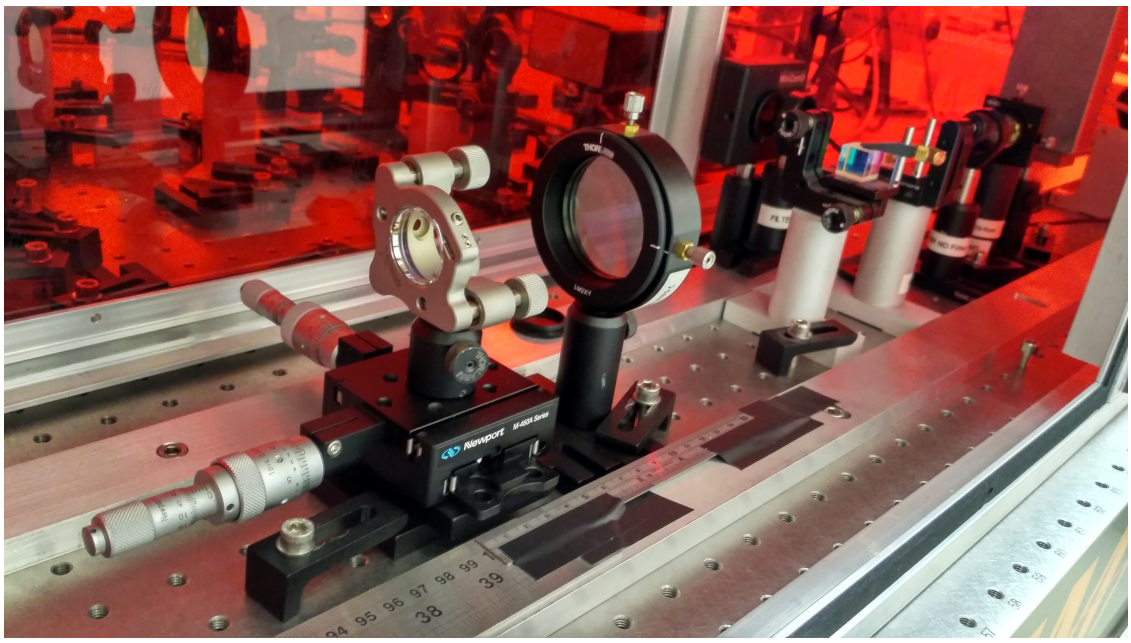

Figure 5.2: Photo of the end mirror and components at the transmission port. The end mirror is placed on a linear translation stage which allows us to control the cavity length with a precision up to 0.5 μm. The transmitted beam is focused by a two-inch lens, then split and delivered to a photodetector and a camera.

By using the translation stage, it is easy to change the cavity length, however it is hard to know the absolute cavity length precisely. There must be a way to accurately measure the cavity length so that we can know the stability of the cavity. As, when we push the cavity towards the edge of stability, higher-order modes bunch together, the mode separation frequency gives a lot of information about the cavity configuration. From Equation 3.12, Equation 3.13 and Equation 4.4, we can derive

the mode separation frequency of a plane-concave cavity

$$\mathrm{MSF_{PCC}} = \frac{\mathrm{FSR}}{\pi} \arctan \frac{L}{z_R}, \tag{5.1}$$

where $z_R = \pi\omega_0^2/\lambda$ is the Rayleigh range. In a general cavity, the relationship between the beam waist radius and the g-factor is

$$\omega_0^2 = \frac{L\lambda}{\pi} \sqrt{\frac{g_1 g_2 \left(1 - g_1 g_2\right)}{\left(g_1 + g_2 - 2 g_1 g_2\right)^2}}. \tag{5.2}$$

For our plane-concave cavity where the ROC of the input mirror is infinite, we have $g_1 = 1$ and $g_2 = g$, so the beam waist radius and the Rayleigh range can be written as

$$\omega_0^2 = \frac{L\lambda}{\pi} \sqrt{\frac{g}{1-g}} \quad \text{and} \quad z_R = L\sqrt{\frac{g}{1-g}}. \tag{5.3}$$

The mode separation frequency becomes

$$\mathrm{MSF_{PCC}} = \frac{\mathrm{FSR}}{\pi} \arctan \sqrt{\frac{g}{1-g}}, \tag{5.4}$$

Alternatively, we can write the g-factor as a function of the mode separation frequency

$$\begin{aligned} g &= \left[1 + \tan^2\left(\frac{\mathrm{MSF_{PCC}}}{\mathrm{FSR}}\pi\right)\right]^{-1} \\ &= \frac{1}{2}\left[1 + \cos\left(\frac{2\mathrm{MSF_{PCC}}}{\mathrm{FSR}}\pi\right)\right] = \cos^2\left(\frac{\mathrm{MSF_{PCC}}}{\mathrm{FSR}}\pi\right), \end{aligned} \tag{5.5}$$

and the cavity length is

$$L = R_c\left(1 - g\right) = R_c \sin^2\left(\frac{\mathrm{MSF_{PCC}}}{\mathrm{FSR}}\pi\right), \tag{5.6}$$

where $R_c = 1\,\mathrm{m}$ is the ROC of the end mirror.

Note that $\mathrm{MSF_{PCC}}$ is the mode separation frequency between two modes in adjacent orders, for example between the first order mode and the fundamental mode. As

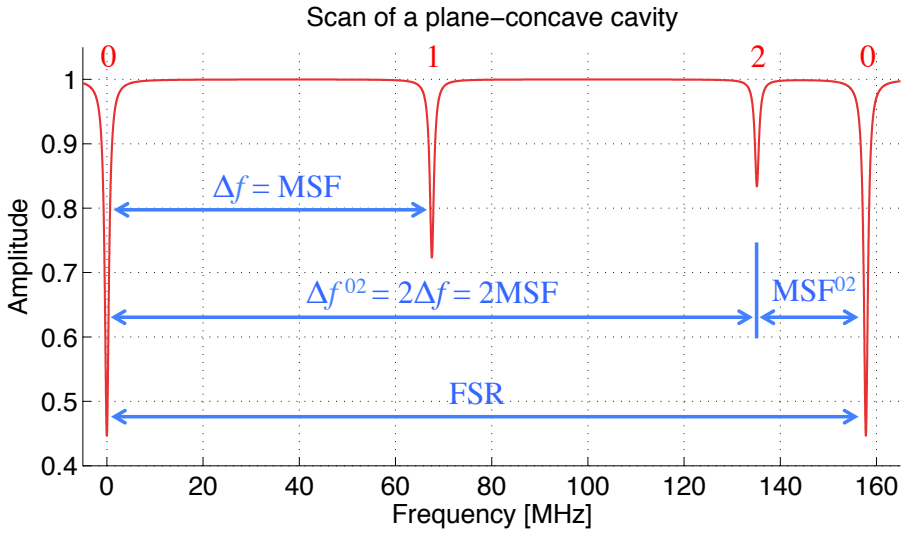

Figure 5.3: Resonant frequencies of the first order mode and the second order mode in a near-stable plane-concave cavity. The mode separation frequency (MSF) can be measured and used to extract information of the cavity stability. The MSF between the second order mode and the fundamental mode $\mathrm{MSF}^{02}_{\mathrm{PCC}}$ is larger than half of the FSR. What we usually observe (e.g. from the oscilloscope) is the shorter distance between the second order mode and the 'next' resonant fundamental mode.

the first order mode is used as a reference for misalignment, and is eliminated when the cavity is well aligned, we measure the separation frequency between the second order mode and the fundamental mode $\mathrm{MSF}^{02}_{\mathrm{PCC}}$. We care about the second order mode because in the near-unstable plane-concave cavity the second order mode is close to the resonance of the fundamental mode, which can cause problems, while the first order mode is far away and well anti-resonant.

As the separation frequency between the second order mode and the fundamental mode is larger than half of the FSR, what we usually observe is the shorter distance between the second order mode and the 'next' resonant fundamental mode $\mathrm{MSF}^{02}_{\mathrm{PCC}}$ (see Figure 5.3). The original mode separation frequency can be expressed as

$$\mathrm{MSF}_{\mathrm{PCC}} = \frac{1}{2}\left(\mathrm{FSR} - \mathrm{MSF}^{02}_{\mathrm{PCC}}\right), \tag{5.7}$$

The g-factor of the plane-concave cavity can then be derived from the measured

mode separation frequency

$$g = \cos^2\left[\frac{\pi}{2}\left(1 - \frac{\mathrm{MSF}^{02}_{\mathrm{PCC}}}{\mathrm{FSR}}\right)\right] = \frac{1}{2}\left[1 - \cos\left(\frac{\mathrm{MSF}^{02}_{\mathrm{PCC}}}{\mathrm{FSR}}\pi\right)\right], \tag{5.8}$$

and the cavity length is

$$L = \frac{R_c}{2}\left[1 + \cos\left(\frac{\mathrm{MSF}^{02}_{\mathrm{PCC}}}{\mathrm{FSR}}\pi\right)\right]. \tag{5.9}$$

Figure 5.4 shows the g-factor as a function of $\mathrm{MSF}^{02}_{\mathrm{PCC}}$. In the region where $g < 0.01$, the mode separation frequency between the second order mode and the fundamental mode $\mathrm{MSF}^{02}_{\mathrm{PCC}} < 10\,\mathrm{MHz}$, while in the region where $g < 0.001$, $\mathrm{MSF}^{02}_{\mathrm{PCC}} < 3\,\mathrm{MHz}$. The linewidth of our cavity is about 36 kHz.

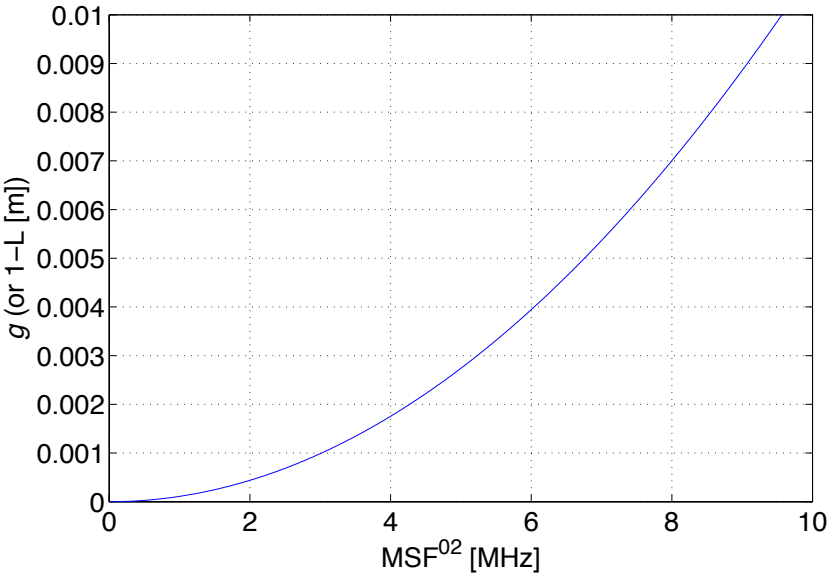

Figure 5.4: A plot showing the g-factor or $1 - L$ (supposing $R_c = 1\,\mathrm{m}$) as a function of $\mathrm{MSF}^{02}_{\mathrm{PCC}}$. In the region where $g < 0.001$, the mode separation frequency between the second order mode and the fundamental mode $\mathrm{MSF}^{02}_{\mathrm{PCC}} < 3\,\mathrm{MHz}$.

5.2 Higher-order mode splitting

Using the current setup, we are able to push the cavity to the region where $g < 0.01$ and beyond. Resonances of the cavity are measured by scanning frequency of the

probe laser. In this stability region, we observed that higher-order modes (HOMs) are in Hermite-Gaussian (HG) shape, and HG modes of the same order are clearly separated from each other. For example, the HG02 mode and the HG20 mode are separated (see Figure 5.5). Normally, resonances of HOMs in the same order should overlap with each other because they experience the same Gouy phase delay from the fundamental mode. This separation is usually produced by the imperfect cavity mirror figure, for example, if the 'spherical' mirror actually has and ellipsoidal surface rather than a perfectly spherical surface.

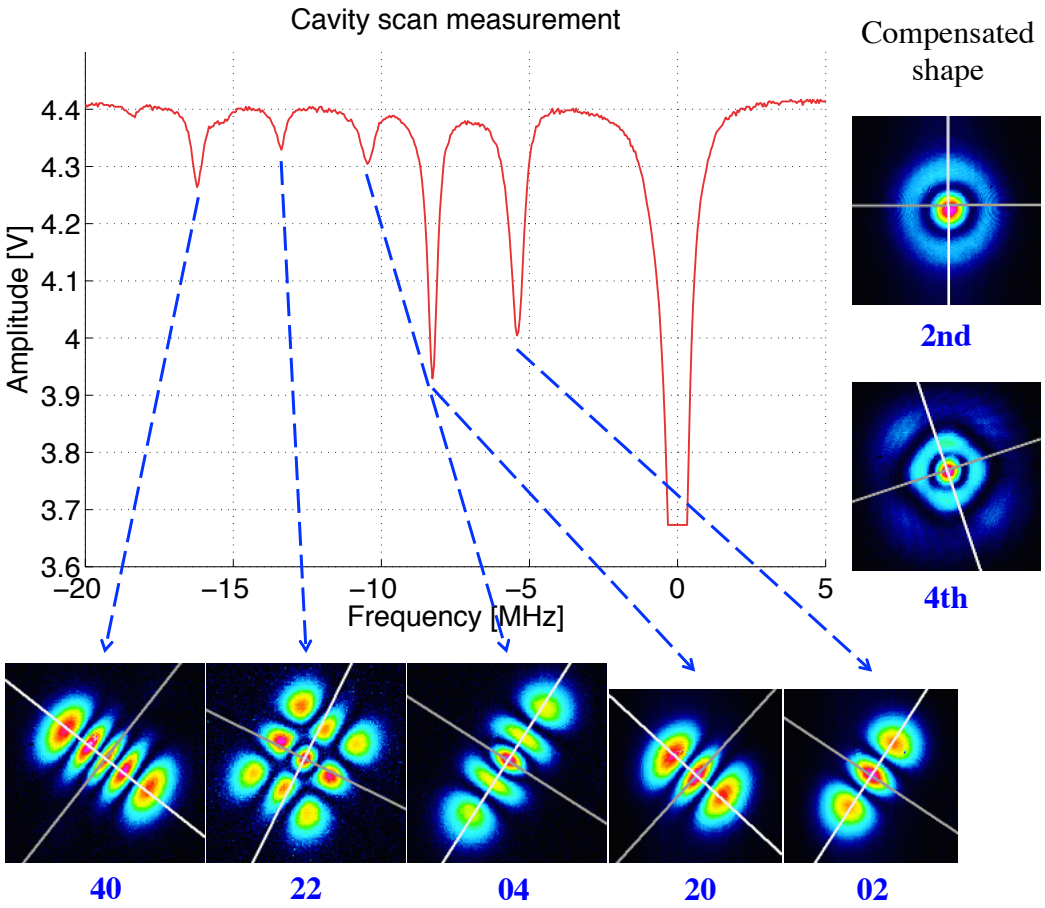

Figure 5.5: A cavity scan measurement showing resonant frequencies of HOMs. HOMs in the same order are observed to be separated from each other in frequency, which is due to the ellipsoidal surface of the end mirror. Shapes of split HOMs are shown in the bottom, from which we can tell they are Hermite-Gauss modes. The separation can be reduced by increasing the stress of the screw holding the end mirror, thus compensating the surface figure error. Compensated shapes of the second order mode and the fourth order mode are shown in the right. These are much closer to the circularly symmetric Laguerre-Gauss modes.

It was observed that these modes were at an angle of 45° from the horizontal. A possible explanation for this was that it could be related to the position of the screw in the mirror mount holding the mirror, as this would produce some stress in the mirror which could deform it in this direction. We therefore tried loosening the screw. It was found that this actually increased the separation. The separation could be reduced by tightening this screw instead of loosening, which suggests that the surface of the end mirror itself was intrinsically ellipsoidal along this axis. As a further check, it was found that rotating the end mirror by about 45° caused these modes to also rotate by 45°, so that they were almost aligned along the horizontal and vertical axes. Figure 5.5 also shows compensated shapes of the second order mode and the fourth order mode after we tighten the screw to reduce the mirror figure deformation. Split resonant peaks in the same order accordingly overlapped with each other (not shown in the figure). Note that the HG11 mode is also a second order mode. It was observed with a small intensity whose resonant frequency is between that of the HG02 and HG20 modes. Its shape is not shown here but can be found in Figure 5.9. The sum of HG02, HG11 and HG 20 modes is a second order Laguerre-Gaussian (LG) mode which is circularly symmetric. Similarly, HG13 and HG 31 modes are also in the fourth order. As their amplitudes are too small, the summed fourth order mode is not purely circular.

This kind of mode separation, caused by mirror imperfections, is usually negligible in a stable cavity, but can be significant in a near-unstable cavity. Mirror imperfections and surface deformations become the dominant factors in determining mode behaviour when the cavity is close to the boundary of stability. In the next section, we will describe the behaviour of the cavity as we move closer to the edge of stability.

5.3 Quantifying the stability

In this section, we would like to investigate behaviour of the frequency, beam profile, and transmission characteristics of the resonant modes when the cavity is gradually

pushed towards the stability edge. We then present a method of quantifying the cavity stability using these measurements.

As introduced in Section 5.1, the MSF can be measured to extract information of the cavity stability. In order to accurately quantify the stability, we measure a series of mode separation frequencies as the cavity length is incrementally increased. The reference laser is locked to a fundamental mode of the cavity via Pound-Drever-Hall technique. The probe laser is locked to the reference laser through the offset phase locking scheme (introduced in Section 4.3.2). As shown in Figure 4.31, the frequency difference between the probe laser and the reference laser is equal to the output frequency of the tunable oscillator in the offset phase locking loop. The source of a network analyser, which can produce a swept sin signal, is used as the tunable oscillator. We want to sweep the probe laser frequency around the cavity's resonance and map resonant frequencies for the fundamental mode and second order modes. Unfortunately, in the phase locking loop, we can't set the oscillator's frequency to zero, i.e., the frequency of the probe laser cannot be the same as that of the reference laser. Instead, the initial frequency of the probe laser is set to be one FSR (of the 1 m cavity, about 150 MHz) away from the reference laser.

Figure 5.6 shows a series of measured mode resonances including second order modes and the fundamental mode. The scanning rate of the probe laser is slow so that the phase locking loop stays locked. The number of points should be sufficient to acquire a high resolution. In this measurement, the total scanning time is set to be 90 seconds with a resolution set to give 800 points. The maximum scanning range used is 2.5 MHz, resulting in a scanning step of 3.125 kHz. The DC output signal of the photodetector detecting the power of the transmitted beam is sent to the network analyser, which records the transmitted power as a function of the sweeping frequency.

The cavity length is changed from $999.0 - 1.2$ mm (L1) to $999.0 + 1.4$ mm (L18) according to readings of the translation stage of the end mirror. Each time when we change the cavity length, the cavity inevitably becomes slightly misaligned, because

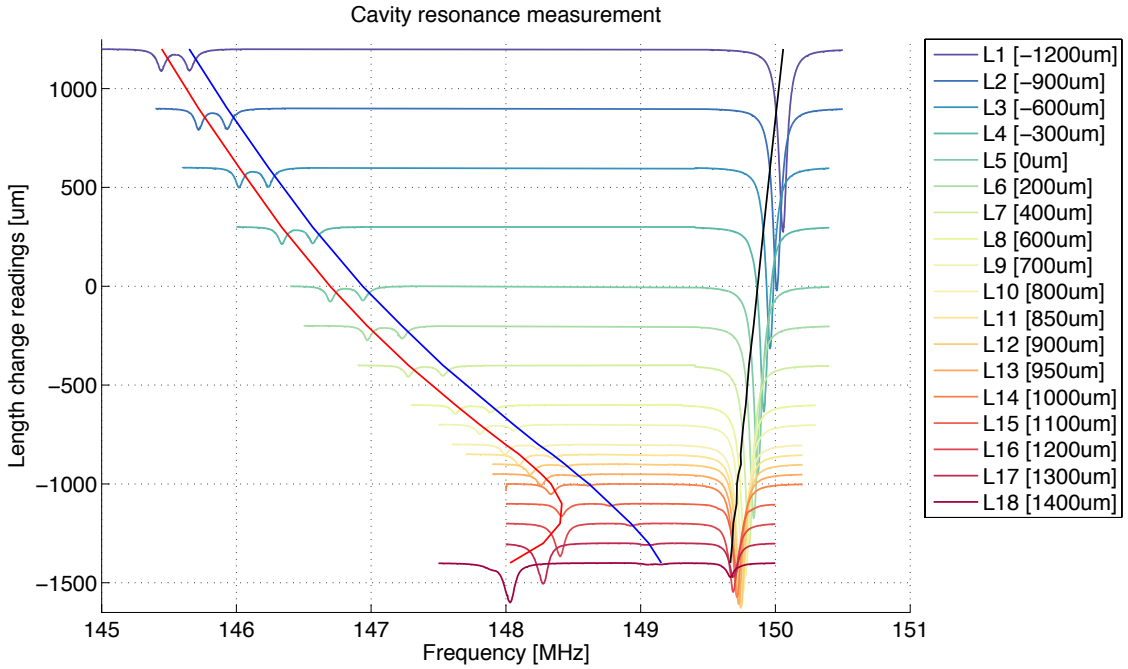

Figure 5.6: Resonances measured by scanning the frequency of the probe laser when pushing the cavity to near-unstable region. We track resonant frequencies of the fundamental mode, and HG02 and HG20 modes, which are plotted in black, blue and red respectively. L5 is the position where the translation stage gives a reference reading of 999.0 mm. Legends from L1 to L18 display relative length changes from this value. The y-axis represents the cavity length deviation from L5 for each measurement. Peaks on the right are resonant frequencies of the fundamental mode, which give a very good measurement of the free spectral range of the cavity. The two peaks on the left at first represent resonances of the separated HG20 and HG02 modes. Mode separation frequencies between second order modes and the fundamental mode become smaller and smaller. But beyond a certain point, it seems that second order modes begin to move back away from the fundamental mode. We believe that what we tracked are no longer the pure second order modes; indeed, the measured beam profiles appear to have an increasing fraction of higher order mode content. It could be that the cavity has in these cases become unstable, but these modes are near-resonant in the cavity.

the longitudinal motion of the end mirror controlled by the translation stage does not exactly overlap with the cavity axis. We re-align the probe laser to the cavity by looking at error signals in the alignment system and minimising the amplitude of the first order mode. From L1 to L9, the amplitude of the first order mode can be minimised almost to zero. After L10, however, the residual first order mode increases significantly and can no longer be eliminated, no matter how the cavity is aligned.

This is thought to be due to the large beam size suffering from clipping loss. The reflected beam seen by the alignment system is no longer axially symmetric, thus the difference signal between the two halves of the beam cannot be zero. The mode matching suffers a similar but more severe problem. From L1 to L18, amplitudes of the two second order modes (HG02 and HG20) can never both be reduced to zero at the same time. This is caused by the ellipsoidal surface of the end mirror. In this measurement, as we only care about the frequency, rather than the amplitude of the resonant mode, the mode matching lens group is just put at a designated location which gives the minimum stability ($g = 0.00004$ shown in Figure 4.6), and is not moved through out the measurement. This means we will have a varying amount of HG02 and HG20 content in the cavity input beam during the experiment.

In Figure 5.6, the peaks on the right are resonances of the fundamental mode, which tell us the free spectral range of the cavity. The FSR$= c/(2L)$ changes almost linearly as a function of L, as expected, when L changes by a small amount. The two peaks on the left at first represent resonances of the, now separated, HG20 and HG02 modes. The frequency differences between second order modes and the fundamental mode get smaller and smaller as the cavity length increases. There is, however, a point either very close to the edge of stability, or when the cavity has become unstable, where the modes we track change direction, and begin to move back away from the fundamental mode. Images of the transmitted beam shows that in this case these modes are no longer the same second order modes (in fact, no longer even Gaussian modes, if the cavity is unstable).

From the measured resonant frequencies, we can fit their behaviour as a function of cavity length or g-factor. According to Equation 5.6 we know the relationship between the cavity length L and the frequency difference Δf. Note that the resonant frequency of second order modes we measured here read directly from the network analyser is Δf^{02} instead of MSF^{02} (see Figure 5.3). As $\Delta f^{02} = 2\Delta f$, the equation becomes

$$L_0 + \Delta L = \frac{R_c}{2}\left[1 - \cos\left(\frac{\Delta f^{02}}{\mathrm{FSR}}\pi\right)\right], \tag{5.10}$$

where Δf^{02} and FSR are both values measured by the network analyser. ΔL is the relative length change recorded by the translation stage of the end mirror. L_0 is the original absolute cavity length, which is left as a free parameter and extracted by fitting the resulting data. In our fitting model, we treat the input mirror as having a perfectly flat surface. The end mirror has a concave surface with a ROC of around 1 m. According to our measurements, however, the HG20 and HG02 mode see different deviations from this value in the horizontal and vertical directions; this may be due to mirror surface imperfections. The frequency behaviours of these two modes are fitted independently to Equation 5.10, where L_0 and R_c are both fitted parameters. The g-factor then can be calculated from $g = 1 - L/R_c$. Results are shown in Figure 5.7. Only the fully coloured points are used in the fit.

By fitting the frequencies of HG20 and HG02 modes separately, we get two sets of results for L_0 and R_c. The difference in the cavity length L_0 seen by the two second order modes is negligible (about 6 μm). However, the L_0 derived from the free spectral range ($L_0 = c/(2\,\mathrm{FSR})$) according to resonances of the fundamental mode gives a different value (about 300 μm larger). This could be due to the imperfect surface of the input mirror. The ROCs for HG20 and HG02 modes in the fitting results differ by about 160 μm. The data agrees well with the predicted Gaussian behaviour up to a certain point, which appears to be very close to the edge of stability.

It is found that the HG02 mode reaches the edge of stability before the HG20 mode does, indicating that the ROC in the vertical direction is smaller than that in the horizontal direction. Figure 5.8 gives the frequency difference of these two modes as a function of cavity g-factor. The curve in solid line shows the simulation. The model used supposes the input mirror is perfectly flat. The end mirror has an ellipsoidal surface with a 160 μm difference in ROCs along the horizontal and vertical directions based on our fitting results. The difference in resonant frequencies of the two modes is small when the cavity is stable, but becomes significantly larger as the cavity approaches instability, as one mode moves towards the fundamental mode more quickly than the other. The measured data of frequency difference between the

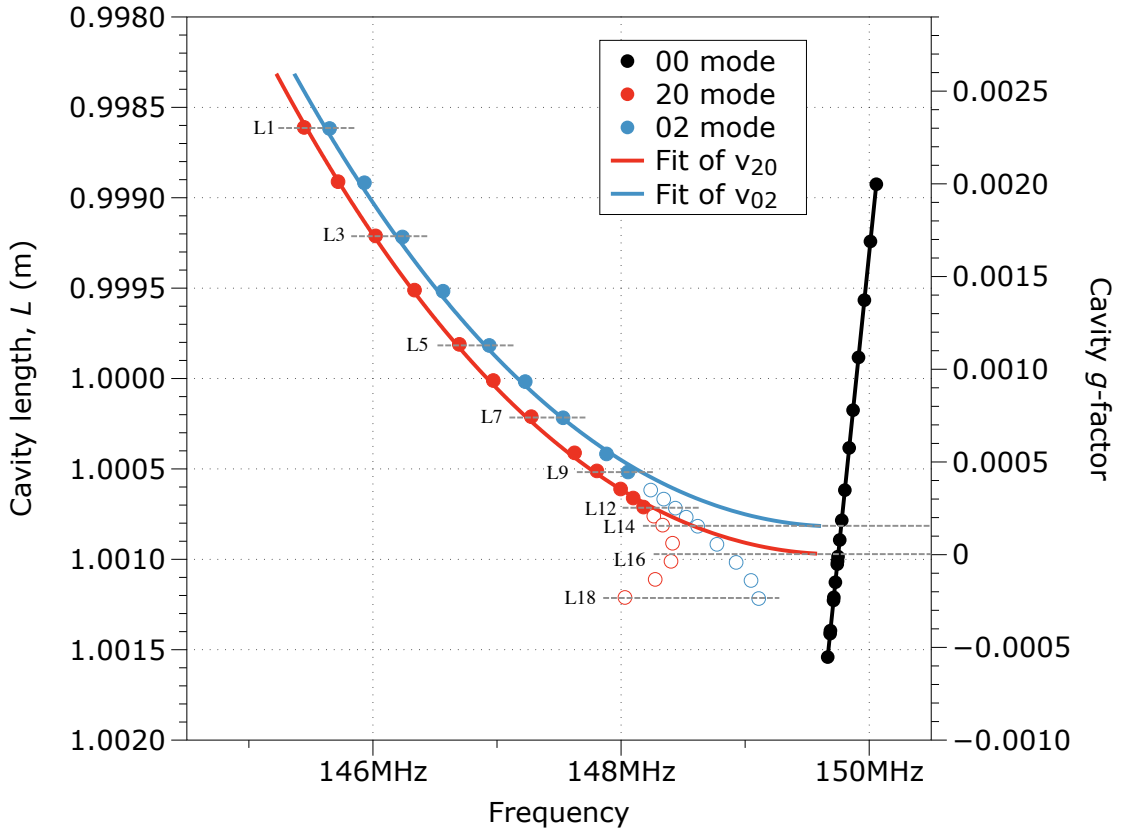

Figure 5.7: Fitting results of measured resonant frequencies for the HG00, HG02 and HG20 modes. The resonance of the fundamental mode, which represents FSR of the cavity, changes almost linearly as expected. The cavity length seen by the fundamental mode is calculated from the equation FSR$= c/(2L)$. The individual fitting for HG20 and HG02 modes gives two sets of values for the cavity length L and the ROC of the end mirror. Only solid dots are used for the fitting. Cavity lengths seen by the two second order modes are almost the same (with a difference of 6 μm), but approximately 300 μm smaller than the length seen by the fundamental mode. The fitting result also indicates that the HG02 mode reaches the edge of stability before the HG20 mode does. The ROC seen by the HG02 mode is about 160 μm smaller than the HG20 mode. The measured resonances of the HG02 and HG20 modes start to deviate from the fitting after L9 and L12, respectively. The fitting suggests they reach the edge of stability at L14 and L16. From the points where they start to deviate to the points where they reach their stability edge, the total cavity length changes for them are both about 300 μm. Values of the cavity g-factor on the right-hand y-axis are calculated based on the HG20 mode.

two modes is plotted as dots in the figure. Solid dots represent data from L1 to L9 where behaviours of second order modes match our fittings (see Figure 5.7). Beyond this, the measured data doesn't match the simulation very well. This indicates that mode couplings are complicated in the near-unstable region. The ellipsoidal surface

of the end mirror that we modelled is not the only type of aberration that would cause the separation of the HG02 and HG20 modes. A more accurate model of small aberrations in the mirror surface is necessary to better predict behaviour of transverse modes.

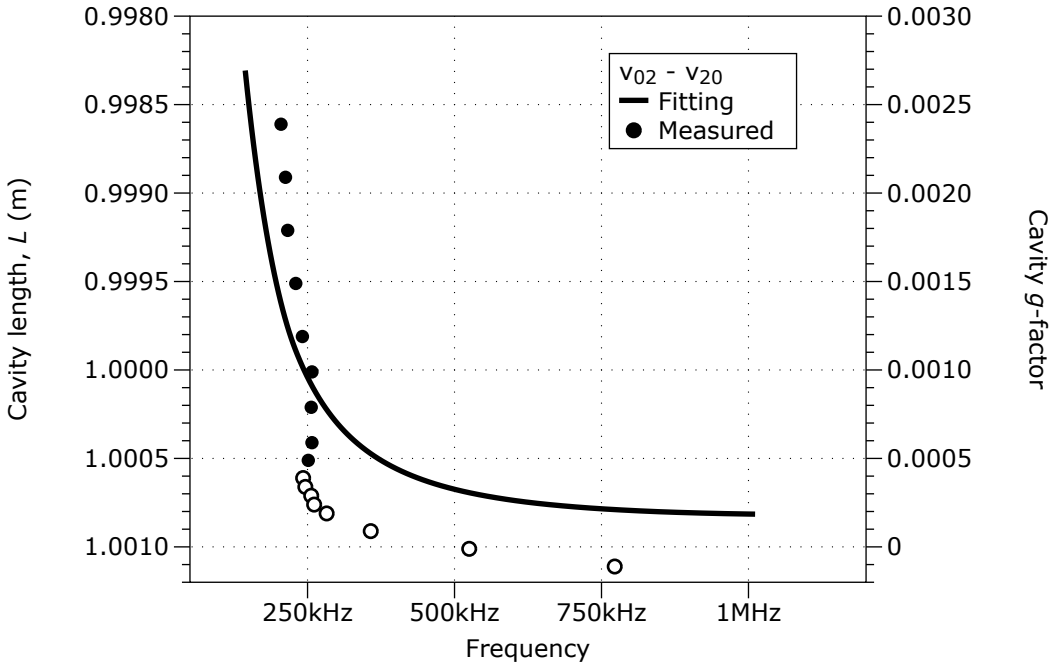

Figure 5.8: Frequency difference between the HG02 mode and the HG20 mode as a function of cavity g-factor. The curve in solid line shows the simulation with a simple model only taking into account the ellipsoidal surface of the end mirror. Measured data is shown as dots. Solid dots represent data measured from L1 to L9 in which the behaviour of second order modes can be predicted according to our fitting. Hollow dots represent data measured after L9 where the modes we tracked are no longer pure second order modes. The mismatch between the curve and solid dots in this figure indicates that the ellipsoidal surface of the end mirror that we modelled is not the only cause of the separation of the HG02 and HG20 modes.

During each scanning measurement for a given cavity length, the shapes of resonant modes are recorded by a CCD camera (WinCamD) at the transmission port of the cavity. Figure 5.9 shows the shapes of these transverse modes.

Based on our fitted results in Figure 5.7, the HG02 mode starts to deviate from the fitting after L9. From L10 to L13, the resonance of the HG02 mode is moving quickly towards the fundamental mode; they then start to overlap with each other. By looking at the shape of the HG02 mode we know that the resonance we tracked

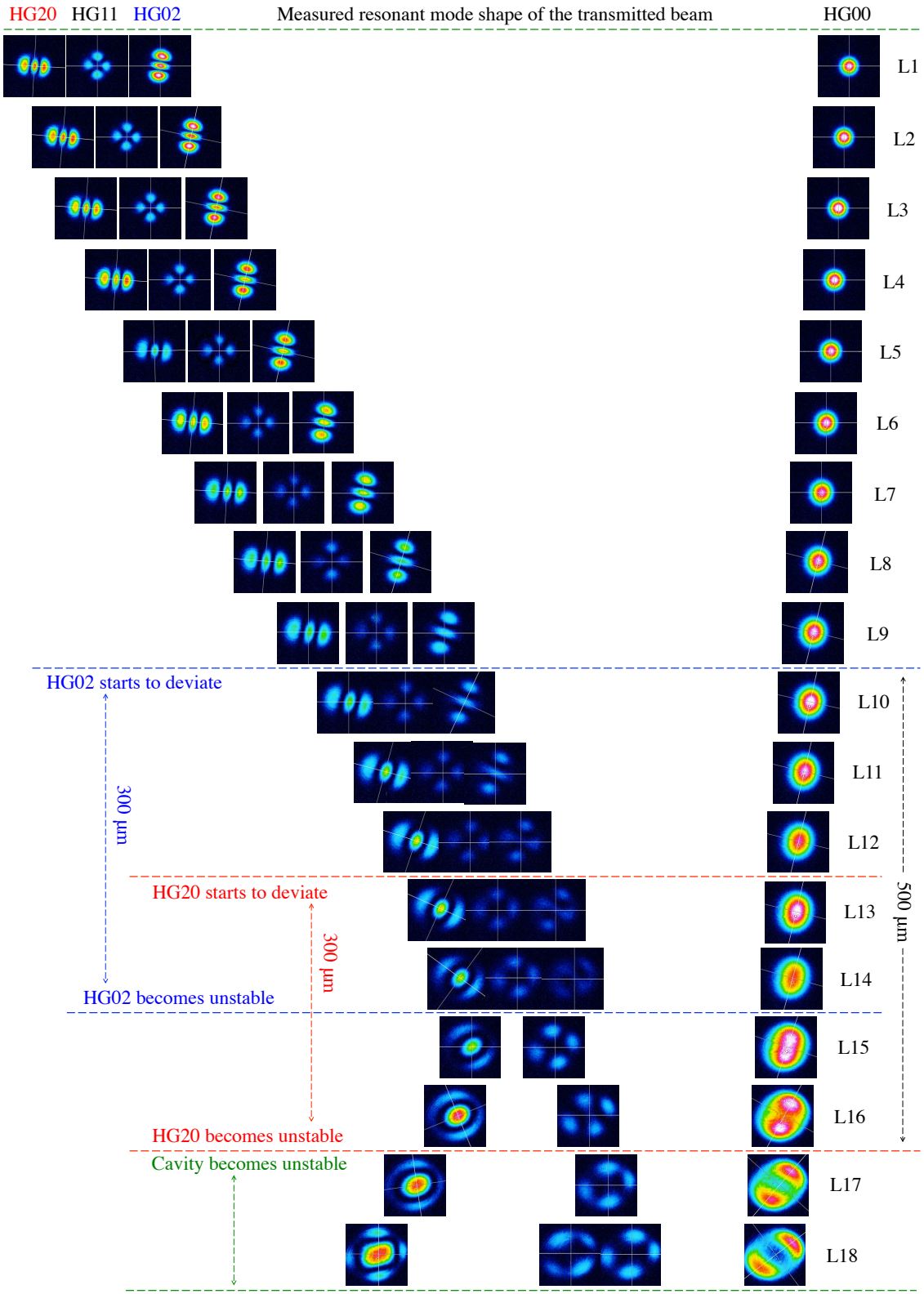

Figure 5.9: Observed resonant mode shapes of the transmitted beam in each cavity length.

is no longer the resonance of the HG02 mode. The shape of the fundamental mode starts to split into two spots. This is due to the overlap between the HG02 mode and the fundamental mode. The HG02 mode should finally arrive at the edge of its stability at L14 and completely overlap with the fundamental mode. The sum of the amplitudes of these two modes results in a beam with two spots. An explanation of this mechanism is shown in Figure 5.10.

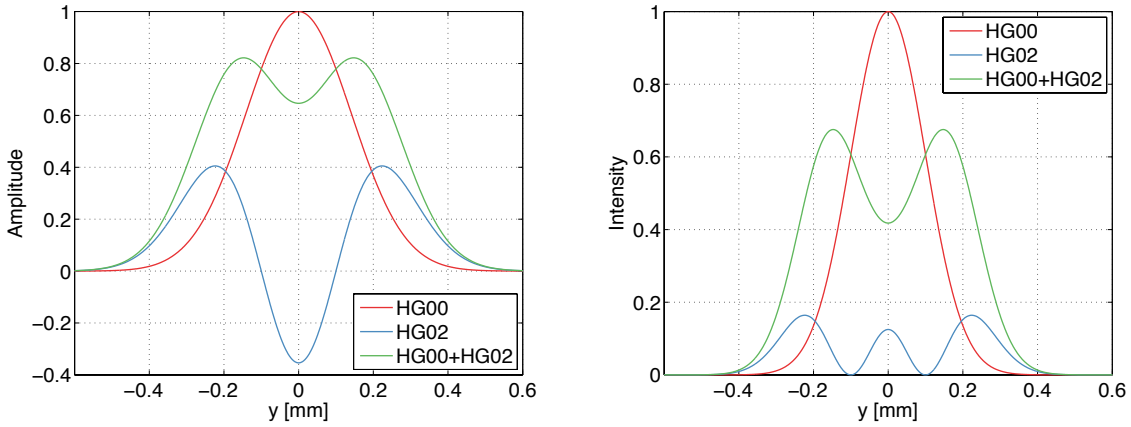

Figure 5.10: The overlap between the fundamental mode (HG00) and the HG02 mode. The left plot shows amplitudes of the fundamental mode, the HG02 mode and their sum. The right plot shows the intensity of each mode. The resultant beam has two intensity peaks which correspond to the two split spots we observed. These plots are simulations.

From L9 (where the HG02 mode starts to deviate from the fitting) to L14 (where the HG02 mode reaches its stability edge), the total cavity length change is about 300 μm. After L14, the cavity becomes unstable for the HG02 mode, but still stable for the HG20 mode. L16 should be the stability edge for the HG20 mode. From L12 to L16, the HG20 mode starts to deviate from the fitting and finally reaches the edge. During this approach, the overall cavity length change is also about 300 μm.

After L16, the cavity is totally unstable, in which the optical loss becomes significant and results in non-Gaussian beams. Even so, a reasonably clear error signal for the Pound-Drever-Hall scheme can still be extracted, and the cavity length can be stabilised. Error signals for some cavity stabilities are shown in Figure 5.11. The slope at 0 MHz corresponding to the error signal of the fundamental mode is still

quite clean even when the cavity is slightly unstable. Slopes at ±1 MHz represent the 1 MHz phase modulation sidebands. Error signals of the HG20 mode, the HG02 mode and their ±1 MHz sidebands can also be seen on the left. They all move towards the error signal of the fundamental mode when we push the cavity to the edge of stability. It is useful to point out that when the second order mode starts to overlap with the fundamental mode, there will be an offset introduced to the error signal of the fundamental mode. The reference laser is no longer locked to a pure fundamental mode. However, the resonance of the fundamental mode measured by the probe laser suffers from the same offset. The frequency difference between the probe laser and the reference laser still gives a very accurate measurement for the FSR of the cavity. The Pound-Drever-Hall error signal of the 'fundamental mode' finally starts to degenerate dramatically when we pushed the cavity 400 μm further beyond the stability edge.

Using Equation 3.16 and Equation 5.8, we can calculate the separation factor of the plane-concave cavity to be

$$S_{PCC}^{02} = \frac{\mathscr{F}}{\pi} \arccos\left(1 - 2g\right). \tag{5.11}$$

Figure 5.12 shows the mode separation factor between the second order mode and the fundamental mode as a function of cavity g-factor in a plane-concave cavity.

With our tabletop setup, the break-down point (where the second order mode behaviour deviates from predictions of our fitting) happens at around $g = 0.0003$, corresponding to a separation factor of 23. This value is much higher than expected. At such a point, the resonance of the fundamental mode is still far away from resonances of second order modes. It means that in our cavity with a high finesse, the mode bunching is not the critical problem that causes deviations from the mode behaviour predicted by our model. The main factor that determines the mode behaviour in this extreme near-unstable condition is instead thought to be mirror imperfections.

It is worth pointing out that with better mode matching and thermal compensation

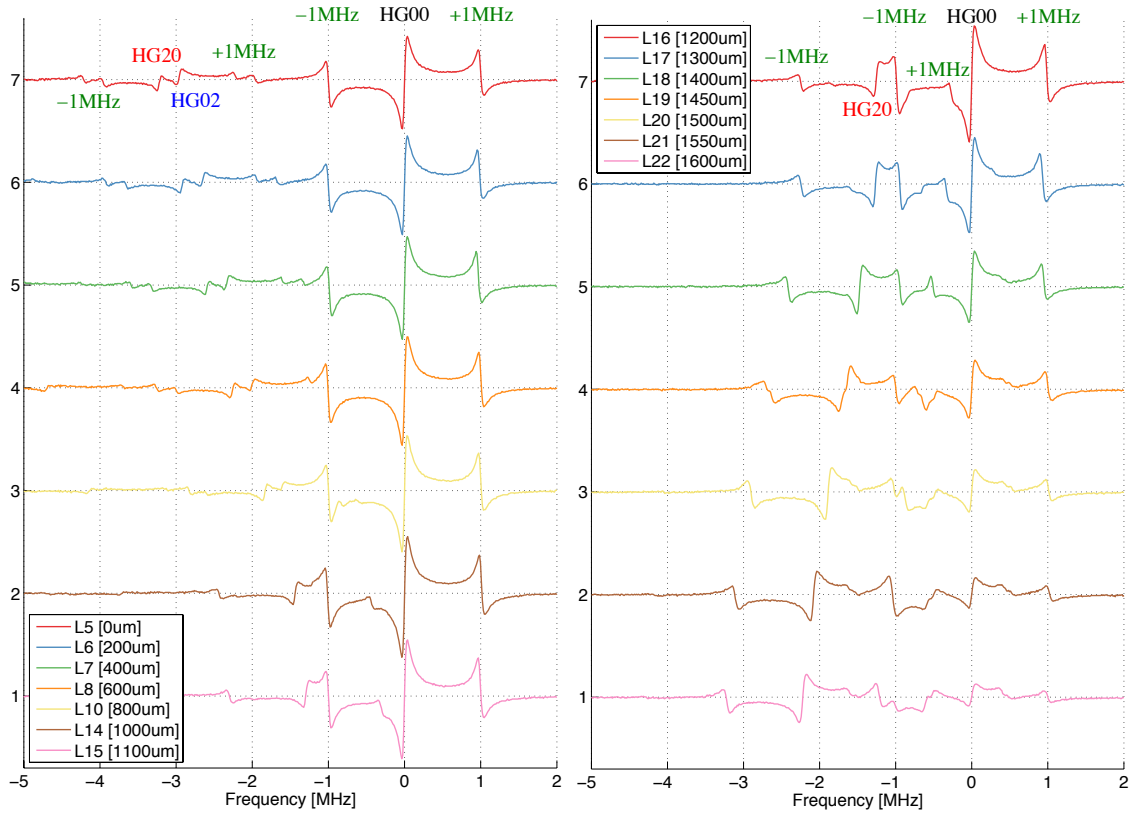

Figure 5.11: Measured error signals when pushing the cavity to the near-unstable region. The slope at 0 MHz corresponds to the error signal generated from the fundamental mode. Slopes at ±1 MHz represent the 1 MHz phase modulation sidebands. Error signals of the HG20 mode, the HG02 mode and their ±1 MHz phase modulation sidebands can be also observed. They move towards the error signal of the fundamental mode when we push the cavity to the edge of stability. The Pound-Drever-Hall error signal starts to degenerate when we push the cavity about 400 μm further beyond the stability edge. At this point the optical loss is so great that the error signal is not strong enough to keep the laser locked to the cavity.

systems, it may be possible to push the cavity further and operate it at an extremely near-unstable condition. But it is very difficult and the difficulty increases dramatically when getting increasingly close to the edge. As we mentioned, the separation between the HG02 and HG20 modes increases significantly in NUCs. The surface deformation of the mirror doesn't allow us to achieve a good mode matching in which the two second order modes are minimised at the same time. Thermal compensation schemes can only realistically be applied to compensate large-scale deformations of the mirrors. For practical mirrors, local aberrations of the surface can contribute to much more complicated mode couplings between HOMs in higher orders. These

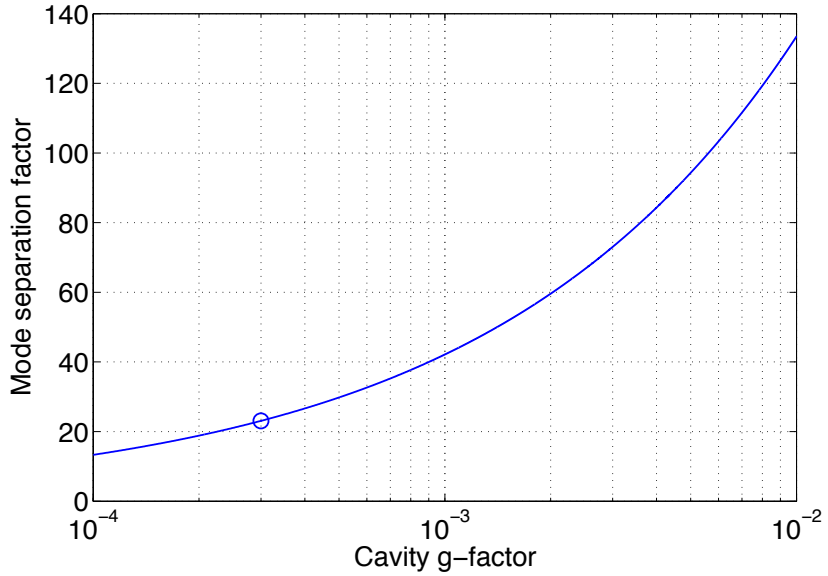

Figure 5.12: The mode separation factor as a function of g-factor of our 1 m plane-concave cavity. The measured second order modes start to deviate from our fitting results at the point of $g = 0.0003$. This point is marked as a circle in the plot. At this point, the cavity has a mode separation factor of 23, so the fundamental mode is still well separated from second order modes.

couplings become larger and more chaotic and unpredictable in a near-unstable cavity, where a good mode matching or a compensation solution may be impossible. It can be imagined that for future gravitational wave detectors, to enable a cavity to perform at its near-unstable condition, much higher requirements are necessary on mirror surface qualities, length stabilisation systems and precise thermal compensation systems. Mirror surface imperfections are probably the critical factor that ultimately limits the maximum achievable stability.

5.4 Conclusion

In this chapter, we investigated the behaviour of the NUC with a tabletop experiment we built in the interferometry lab in Birmingham. This involved a 1 m cavity which was pushed to the edge of stability by incrementally increasing the its length. We measured a series of frequencies and shapes of resonant transverse modes, including the fundamental mode, and the separate HG02 and HG20 modes. The

measured resonant frequencies were compared with our fitting results, by which the stability of the cavity is quantified. Frequency behaviours of the two second order modes suggest the ellipsoidal surface of the end mirror has a 160 μm difference in ROCs along the horizontal and vertical directions. The measured HG02 and HG20 modes both start to deviate from the predicted trend at a cavity length 300 μm before reaching the stability edge. The corresponding break-down g-factor is 0.0003. At this point, the mode separation factor is 23, where the fundamental mode is still well isolated from second order modes. The main factor that limits the maximum achievable stability is the mirror imperfection.

Chapter 6

Summary and future work

6.1 Summary and conclusions

In this thesis, I have mainly focused on applications of near-unstable cavities (NUCs) to laser precise interferometry, and on aspects of their behaviour most relevant to this. Advanced gravitational wave detectors use a combination of high laser power and coupled cavities to significantly enhance their sensitivity. Motivations for using NUCs have been discussed in detail in Section 3.1. They are used in one current advanced gravitational wave detector (Advanced Virgo). This is due to the greater simplicity and fewer components required for an NUC system. It has also been proposed that NUCs could be used in future detectors to give a reliable reduction in coating thermal noise.

NUCs are very sensitive to changes in the ROC of the end mirrors. For interferometers in gravitational wave detectors, which use high power laser beams, small ROC changes due to the thermal effects caused by laser heating of the mirrors, particularly by scattered light incident on non-reflective components of the mirror support, can alter the geometric stability of NUCs, and even drive them out of the stable region. In Chapter 2, we developed a thermal model for predicting the thermal status of the cavity mirror after the cavity is locked and the high laser power

rings up inside the cavity. This model allows mechanical mode frequencies of the mirrors to be used as very accurate thermometers. We have provided an estimate of coating absorption for the Advanced LIGO Livingston detector. The scattered light incident on the ring heater is also estimated. An extra component is introduced into the model to account for radiative contributions from objects in the vicinity of the test mass. By taking into account the thermal radiation between the mirror, objects surrounding the it, and the daily fluctuating ambient temperature, the model can estimate the mirror temperature over time scales of tens of hours. This model has then been tested on a data set from December. The accuracy of the model is currently limited by the number of long periods in which the cavity detector was kept in lock, starting from its initial ambient thermal status. We are also limited by the performance of the ambient temperature sensor. We expect to improve the model further when more precise and reliable ambient temperature sensors become available. The thermal model developed in this thesis can help the thermal compensation system to maintain the cavity stability if NUCs are going to be used as arm cavities for future gravitational wave interferometers. My contribution to this work has been part of a collaboration between the Birmingham and the LIGO Livingston Observatory. Results presented have been published in [1].

Another important experiment carried out as part of this Ph.D. is to design and build a table-top experiment to investigate the optical characteristics of NUCs. NUCs are close to the geometric stability boundary thus can easily move into the unstable regime through small cavity length changes or mirror surface distortions. The Gaussian input beams can also be scattered into higher-order modes through interacting with imperfect mirrors in the near-unstable region. This can translate into high optical loss, as these modes clip or become anti-resonant in the cavity. Another difficulty in using NUCs is Gaussian mode degeneracy, in which multiple modes become resonant in the cavity. These issues have an adverse impact on the detector sensitivity and controllability. During my Ph.D., I designed and built a precise experiment to investigate some of these technical hurdles of NUCs. This comprised an approximately 1 m long cavity, whose length could be incrementally

changed to explore the boundary of the stability region. This cavity is built on an optical bench and accurately controlled with a length stabilisation system and an alignment system. Experimental work was carried out to make these systems robust and reliable, and to optimise the performance of these precise control systems. Once all of these subsystems were set up correctly, the 1 m cavity was pushed to the edge of stability. Measurements were carried out, with the main focus being on mode behaviour when the cavity was near-unstable. The of frequency and shapes of resonant transverse modes were measured for a series of cavity configurations with different values of stability The measured resonant frequencies were compared with the predictions of a model. By fitting these results, we can accurately quantify the cavity stability. It was found that there appeared to be a 'break-down point' at about $g_c = 0.0003$ where mode behaviours started to deviate significantly from our predictions. For a tabletop cavity, the main factor that determines mode behaviour and limits the maximum achievable stability, is the mirror imperfection. This experimental demonstration help to improve out understanding of the behaviour of NUCs, and gives a practical measurement of on how close we can go towards cavity instability before the cavity eigenmodes become too severely affected by mirror figure imperfections. The work I performed provides a support for the design of future ground-based detectors, as well as guidelines for the prototype experiment that will be carried out soon.

6.2 Future work

The analysis in Chapter 5 allows us to precisely quantify the stability of an optical cavity and to potentially characterise mirror surface imperfections. In the future we plan to extended our study to investigate the effect of the cavity finesse on the eigenmode behaviour of an NUC. We also plan to study behaviour of a greater number of higher-order modes, by using input beams in these modes.

In our tabletop demonstration, we pushed the cavity to a break-down stability of $g =$

0.0003 and a mode separation factor around 23. As we used a high finesse cavity, at the break-down point, resonances of second order modes are still far away from that of the fundamental mode. Mirror imperfections are the main factor that determined the break-down point. It might be expected that, for a lower finesse cavity, a smaller mode separation factor could be reached before the effects of mirror figure errors became dominant. In a follow-on investigation, we would like to reduce the finesse of the cavity so that the different effects of the finesse and mirror imperfections can be investigated.

From these experimental results, we find that NUCs are very sensitive to mirror imperfections. For example, the frequency separation for HOMs of the same order is too small to be observed when the cavity is stable. In the near-unstable region, however, the separation becomes thousands of times greater, and thus can be measured easily. In other words, by quantifying behaviours of HOMs in NUCs, we can infer surface imperfections of the mirror. In the tabletop experiment, we only measure the frequency and shape of the second order mode. In the future, we would like to use more HOMs like 4th and 6th order modes. This is a promising technique that could be used for very precisely characterising mirror aberrations.

Bibliography

[1] H Wang, C Blair, M Dovale Álvarez, et al. Thermal modelling of Advanced LIGO test masses. *Classical and Quantum Gravity*, 34(11):115001, 2017. v, 19, 21, 148

[2] B. P. Abbott, R. Abbott, T. D. Abbott, et al. Observation of gravitational waves from a binary black hole merger. *Phys. Rev. Lett.*, 116:061102, Feb 2016. 1

[3] J Aasi, B P Abbott, R Abbott, et al. Advanced ligo. *Classical and Quantum Gravity*, 32(7):074001, 2015. 1, 3, 22, 58

[4] BP Abbott, R Abbott, TD Abbott, et al. GW151226: Observation of gravitational waves from a 22-solar-mass binary black hole coalescence. *Physical Review Letters*, 116(24):241103, 2016. 1

[5] LIGO Scientific, BP Abbott, R Abbott, et al. GW170104: Observation of a 50-Solar-Mass Binary Black Hole Coalescence at Redshift 0.2. *Physical Review Letters*, 118(22):221101, 2017. 1

[6] Peter R Saulson. *Fundamentals of interferometric gravitational wave detectors*. World scientific, 2017. 2

[7] Bangalore Suryanarayana Sathyaprakash and Bernard F Schutz. Physics, astrophysics and cosmology with gravitational waves. *Living Reviews in Relativity*, 12(1):2, 2009. 2, 3

[8] Pia Astone. Resonant mass detectors: present status. *Classical and Quantum Gravity*, 19(7):1227, 2002. 3

[9] BP Abbott, R Abbott, R Adhikari, et al. LIGO: the laser interferometer gravitational-wave observatory. *Reports on Progress in Physics*, 72(7):076901, 2009. 3

[10] T. Accadia et al. Virgo: a laser interferometer to detect gravitational waves. *JINST*, 7(03):P03012, 2012. 3, 24

[11] Benno Willke, Peter Aufmuth, Carsten Aulbert, et al. The GEO 600 gravitational wave detector. *Classical and Quantum Gravity*, 19(7):1377, 2002. 3

[12] Ryutaro Takahashi, TAMA collaboration, et al. Status of TAMA300. *Classical and Quantum Gravity*, 21(5):S403, 2004. 3

[13] F Acernese, M Agathos, K Agatsuma, et al. Advanced Virgo: a second-generation interferometric gravitational wave detector. *Classical and Quantum Gravity*, 32(2):024001, 2015. 4, 17, 24, 45, 58

[14] Hartmut Grote, LIGO Scientific Collaboration, et al. The GEO 600 status. *Classical and Quantum Gravity*, 27(8):084003, 2010. 4

[15] Kentaro Somiya. Detector configuration of KAGRA–the Japanese cryogenic gravitational-wave detector. *Classical and Quantum Gravity*, 29(12):124007, 2012. 4

[16] Yoichi Aso, Yuta Michimura, Kentaro Somiya, et al. Interferometer design of the KAGRA gravitational wave detector. *Physical Review D*, 88(4):043007, 2013. 4

[17] CS Unnikrishnan. IndIGO and LIGO-India: scope and plans for gravitational wave research and precision metrology in India. *International Journal of Modern Physics D*, 22(01):1341010, 2013. 4

[18] Matthew Abernathy, F Acernese, P Ajith, et al. Einstein gravitational wave Telescope conceptual design study. *available from European Gravitational Observatory, document number ET-0106C-10*, 2011. Accessed on 31/07/2017: http://www.et-gw.eu/index.php/etdsdocument. 4, 11, 58

[19] M Punturo, M Abernathy, F Acernese, et al. The Einstein Telescope: a third-generation gravitational wave observatory. *Classical and Quantum Gravity*, 27(19):194002, 2010. 4

[20] B Sathyaprakash, M Abernathy, F Acernese, et al. Scientific objectives of einstein telescope. *Classical and Quantum Gravity*, 29(12):124013, 2012. 4

[21] LIGO Scientific Collaboration. Instrument science white paper. *LIGO Document*, T1600119, 2016. https://dcc.ligo.org/LIGO-T1600119/public. 4, 12, 13

[22] Jun Mizuno. *Comparison of optical configurations for laser-interferoemtric gravitational-wave detectors*. PhD thesis, University of Hannover, 1995. 5

[23] Peter Aufmuth and Karsten Danzmann. Gravitational wave detectors. *New Journal of Physics*, 7(1):202, 2005. 8

[24] Gravitational Wave Interferometer Noise Calculator (GWINC). Accessed on 31/07/2017: https://awiki.ligo-wa.caltech.edu/aLIGO/GWINC. 9

[25] Ting Hong, Huan Yang, Eric K Gustafson, Rana X Adhikari, and Yanbei Chen. Brownian thermal noise in multilayer coated mirrors. *Physical Review D*, 87(8):082001, 2013. 10

[26] Gregory M Harry, Andri M Gretarsson, Peter R Saulson, et al. Thermal noise in interferometric gravitational wave detectors due to dielectric optical coatings. *Classical and Quantum Gravity*, 19(5):897, 2002. 10

[27] B Barr, A Bell, C Bell, et al. LIGO 3 Strawman Design, Team Red. *LIGO Internal Document LIGO-T1200042*, 2012. Accessed on 31/07/2017: https://dcc.ligo.org/public/0086/T1200046/001/. 11, 13

[28] Rand Dannenberg. Advanced LIGO End Test Mass Coating Specification. *LIGO Document*, E0900068, 2014. Available to LVC members: https://dcc.ligo.org/LIGO-E0900068. 11

[29] Akira E Villar, Eric D Black, Riccardo DeSalvo, et al. Measurement of thermal noise in multilayer coatings with optimized layer thickness. *Physical Review D*, 81(12):122001, 2010. 12

[30] Alexander Bunkowski, Oliver Burmeister, Daniel Friedrich, Karsten Danzmann, and Roman Schnabel. High reflectivity grating waveguide coatings for 1064 nm. *Classical and Quantum Gravity*, 23(24):7297, 2006. 12

[31] Daniel Friedrich, Bryan W Barr, Frank Brückner, et al. Waveguide grating mirror in a fully suspended 10 meter Fabry-Perot cavity. *Optics express*, 19(16):14955–14963, 2011. 12

[32] Daniel Heinert, Stefanie Kroker, Daniel Friedrich, et al. Calculation of thermal noise in grating reflectors. *Physical Review D*, 88(4):042001, 2013. 12

[33] F Ya Khalili. Reducing the mirrors coating noise in laser gravitational-wave antennae by means of double mirrors. *Physics Letters A*, 334(1):67–72, 2005. 12, 152

[34] Alexey G Gurkovsky, Daniel Heinert, Stefan Hild, et al. Reducing thermal noise in future gravitational wave detectors by employing Khalili etalons. *Physics Letters A*, 375(46):4147–4157, 2011. 12

[35] Gregory M Harry, Matthew R Abernathy, Andres E Becerra-Toledo, et al. Titania-doped tantala/silica coatings for gravitational-wave detection. *Classical and Quantum Gravity*, 24(2):405, 2006. 12

[36] Raffaele Flaminio, Janyce Franc, Christine Michel, et al. A study of coating mechanical and optical losses in view of reducing mirror thermal noise in gravitational wave detectors. *Classical and Quantum Gravity*, 27(8):084030, 2010. 12

[37] Jessica Steinlechner, Iain W Martin, Jim Hough, et al. Thermal noise reduction and absorption optimization via multimaterial coatings. *Physical Review D*, 91(4):042001, 2015. 12

[38] William Yam, Slawek Gras, and Matthew Evans. Multimaterial coatings with reduced thermal noise. *Physical Review D*, 91(4):042002, 2015. 12

[39] Mihai Bondarescu. *Topics in general relativity*. PhD thesis, 2007. 12

[40] Mihai Bondarescu and Kip S Thorne. New family of light beams and mirror shapes for future LIGO interferometers. *Physical Review D*, 74(8):082003, 2006. 12

[41] Mihai Bondarescu, Oleg Kogan, and Yanbei Chen. Optimal light beams and mirror shapes for future LIGO interferometers. *Physical Review D*, 78(8):082002, 2008. 12

[42] Simon Chelkowski, Stefan Hild, and Andreas Freise. Prospects of higher-order Laguerre-Gauss modes in future gravitational wave detectors. *Physical Review D*, 79(12):122002, 2009. 12

[43] Paul Fulda, Keiko Kokeyama, Simon Chelkowski, and Andreas Freise. Experimental demonstration of higher-order Laguerre-Gauss mode interferometry. *Physical Review D*, 82(1):012002, 2010. 12

[44] Paul Fulda. *Precision Interferometry in a new shape: Higher-order Laguerre-Gauss modes for graviational wave detection*. PhD thesis, University of Birmingham, 2012. 12

[45] Charlotte Bond, Paul Fulda, Ludovico Carbone, Keiko Kokeyama, and Andreas Freise. Higher order Laguerre-Gauss mode degeneracy in realistic, high finesse cavities. *Physical Review D*, 84(10):102002, 2011. 12

[46] Stefan Hild. Future interferometers. *LIGO Document*, G1000715, 2010. Available to LVC members: https://dcc.ligo.org/LIGO-G1000715. 13

[47] Anthony E Siegman. *Lasers university science books*, volume 37. 1986. Available from Google Books. 14

[48] Ryan Lawrence, Michael Zucker, Peter Fritschel, Phil Marfuta, and David Shoemaker. Adaptive thermal compensation of test masses in advanced LIGO. *Classical and Quantum Gravity*, 19(7):1803, 2002. 15

[49] T Accadia, F Acernese, F Antonucci, et al. A thermal compensation system for the gravitational wave detector Virgo. In *Twelfth Marcel Grossmann Meeting on General Relativity*, pages 1652–1656, 2012. 15

[50] Jean-Yves Vinet. On special optical modes and thermal issues in advanced gravitational wave interferometric detectors. *Living Reviews in Relativity*, 12(5), 2009. 16

[51] A Rocchi, E Coccia, V Fafone, et al. Thermal effects and their compensation in Advanced Virgo. *Journal of Physics: Conference Series*, 363(1):012016, 2012. 16, 17, 22

[52] Aidan F Brooks, Benjamin Abbott, Muzammil A Arain, et al. Overview of advanced ligo adaptive optics. *Applied Optics*, 55(29):8256–8265, 2016. 16, 23, 33

[53] Aidan F Brooks, David Hosken, Jesper Munch, et al. Direct measurement of absorption-induced wavefront distortion in high optical power systems. *Applied optics*, 48(2):355–364, 2009. 16

[54] Keisuke Goda, David Ottaway, Blair Connelly, et al. Frequency-resolving spatiotemporal wave-front sensor. *Optics letters*, 29(13):1452–1454, 2004. 16

[55] Kazuhiro Agatsuma, Martin van Beuzekom, Laura van der Schaaf, and Jo van den Brand. Phase camera experiment for advanced virgo. *Nuclear Instruments and Methods in Physics Research Section A: Accelerators, Spectrometers, Detectors and Associated Equipment*, 824:598–599, 2016. 16, 44

[56] Charlotte Bond, Daniel Brown, Andreas Freise, and Kenneth A Strain. Interferometer techniques for gravitational-wave detection. *Living reviews in relativity*, 19(1):1, 2016. 16, 50, 51

[57] Muzammil A Arain et al. Thermal compensation in stable recycling cavity. In *LSC March meeting, Louisiana, USA*, 2006. https://dcc.ligo.org/LIGO-G060155/public. 17

[58] M.A. Arain and G. Mueller. Design of the advanced ligo recycling cavities. *Optics Express*, Vol. 16, Issue 14:10018–10032, 2008. 17

[59] A. M. Gretarsson, E. D'Ambrosio, V. Frolov, B. O'Reilly, and P. K. Fritschel. Effects of mode degeneracy in the LIGO Livingston Observatory recycling cavity. *Journal of the Optical Society of America B Optical Physics*, 24:2821–+, 2007. 18

[60] Kazuhiro Agatsuma, David Rabeling, Martin van Beuzekom, and Jo van den Brand. Phase camera development for gravitational wave detectors. *PoS*, page 228, 2014. 18, 44

[61] Gregory M Harry, LIGO Scientific Collaboration, et al. Advanced ligo: the next generation of gravitational wave detectors. *Classical and Quantum Gravity*, 27(8):084006, 2010. 21

[62] W. Winkler, K. Danzmann, A. Rüdiger, and R. Schilling. Heating by optical absorption and the performance of interferometric gravitational-wave detectors. *Phys. Rev. A*, 44:7022–7036, Dec 1991. 22

[63] K.A. Strain, K. Danzmann, J. Mizuno, et al. Thermal lensing in recycling interferometric gravitational wave detectors. *Physics Letters A*, 194(1):124 – 132, 1994. 22

[64] J. Degallaix, C. Zhao, L. Ju, and D. Blair. Thermal lensing compensation for AIGO high optical power test facility. *Classical and Quantum Gravity*, 21(5):S903, March 2004. 22

[65] C. Zhao, J. Degallaix, L. Ju, et al. Compensation of strong thermal lensing in high-optical-power cavities. *Physical Review Letters*, 2006. 22

[66] VB Braginsky, SE Strigin, and S Pr Vyatchanin. Parametric oscillatory instability in fabry–perot interferometer. *Physics Letters A*, 287(5):331–338, 2001. 22

[67] Matthew Evans, Slawek Gras, Peter Fritschel, et al. Observation of parametric instability in advanced ligo. *Phys. Rev. Lett.*, 114(16):161102, Apr 2015. 22

[68] Carl Blair, Slawek Gras, Richard Abbott, et al. First demonstration of electrostatic damping of parametric instability at advanced ligo. *Physical Review Letters*, 118(15):151102, 2017. 22, 25

[69] Patrice Hello and Jean-Yves Vinet. Analytical models of transient thermoelastic deformations of mirrors heated by high power cw laser beams. *J. Phys. France*, 51:2243–2261, 1990. 22

[70] LIGO Optics. Accessed on 31/07/2017: https://galaxy.ligo.caltech.edu/optics/. 23

[71] GariLynn Billingsley and Liyuan Zhang. The reality of mirrors. *LIGO Document*, G1200565, 2012. https://dcc.ligo.org/LIGO-G1200565/public. 23

[72] Carl Blair and Aidan F Brooks. Personal communication. 2016. Available to LVC members: https://alog.ligo-la.caltech.edu/aLOG/index.php?callRep=19289. 23

[73] R. Day, V. Fafone, J. Marque, et al. Virgo input mirrors thermal effects characterization. VIR-0191A-10, 2010. https://tds.virgo-gw.eu/?content=3&r=7500. 24

[74] B Caron, A Dominjon, C Drezen, et al. The Virgo interferometer. *Classical and Quantum Gravity*, 14(6):1461, 1997. 24

[75] C. Chree. Longitudinal vibrations of a circular bar. *Quarterly Journal of Mathematics*, 21(83/84):287–288, 1886. 24

[76] H Lamb. On Waves in an Elastic Plate. *Proccedings of the Royal Society of London*, 93:114–128, 1917. 24

[77] S.E. Strigin, D.G. Blair, S. Gras, and S.P. Vyatchanin. Numerical calculations of elastic modes frequencies for parametric oscillatory instability in Advanced LIGO interferometer. *Physics Letters A*, 372(35):5727–5731, aug 2008. 24

[78] S A M Spinner. Elastic Moduli of Glasses at Elevated Temperatures by a Dynamic Method. *Journal of the American Ceramic Society*, 39(3):113–118, 1956. 24

[79] S. Spinner and G. W. Cleek. Temperature dependence of young's modulus of vitreous Germania and Silica. *Journal of Applied Physics*, 31(8):1407–1410, 1960. 24

[80] Mechanical properties of fused quartz. https://www.momentive.com/WorkArea/DownloadAsset.aspx?id=24696. 24

[81] Carl Blair. Three mode parametric instability and their control for advanced gravitational wave detectors. *Science China Physics, Mechanics and Astronomy*, 58(1):014201, 2015. 25

[82] Joshua Ramette, Marie Kasprzack, Aidan Brooks, et al. Analytical model for ring heater thermal compensation in the advanced laser interferometer gravitational-wave observatory. *Applied optics*, 55(10):2619–2625, 2016. 33, 44

[83] Phil Willems and Virginio Sannibale. Measurement of the dependence of the youngs modulus of fused silica on temperature. *LIGO Document*, T000188, 2000. https://dcc.ligo.org/LIGO-T000188/public. 33

[84] David Bergström, J Powell, and AFH Kaplan. The absorption of light by rough metal surfaces–a three-dimensional ray-tracing analysis. *Journal of Applied Physics*, 103(10):103515, 2008. 37

[85] Hiro Yamamoto. Mirror scattering loss analysis by integrating sphere measurement. *LIGO Document*, G1600396, 2016. https://dcc.ligo.org/LIGO-G1600396/public. 37

[86] Anthony E Siegman. Unstable optical resonators for laser applications. *Proceedings of the IEEE*, 53(3):277–287, 1965. 43

[87] AE Siegman. Unstable optical resonators. *Applied optics*, 13(2):353–367, 1974. 43

[88] A Siegman and Raymond Arrathoon. Modes in unstable optical resonators and lens waveguides. *IEEE Journal of Quantum electronics*, 3(4):156–163, 1967. 43

[89] GP Karman, GS McDonald, GHC New, and JP Woerdman. Laser optics: Fractal modes in unstable resonators. *Nature*, 402(6758):138, 1999. 43

[90] P Bertet, S Osnaghi, A Rauschenbeutel, et al. A complementarity experiment with an interferometer at the quantum–classical boundary. *Nature*, 411(6834):166–170, 2001. 44

[91] Kadir Durak, Chi Huan Nguyen, Victor Leong, Stanislav Straupe, and Christian Kurtsiefer. Diffraction-limited fabry-perot cavity in the near concentric regime. *New Journal of Physics*, 16(10):103002, 2014. 44

[92] Patrice Hello and Jean-Yves Vinet. Simulation of thermal effects in interferometric gravitational-wave detectors. *Physics Letters A*, 178(5-6):351–356, 1993. 44

[93] P Hello. Compensation for thermal effects in mirrors of gravitational wave interferometers. *The European Physical Journal D-Atomic, Molecular, Optical and Plasma Physics*, 15(3):373–383, 2001. 44

[94] Aidan F Brooks, Thu-Lan Kelly, Peter J Veitch, and Jesper Munch. Ultrasensitive wavefront measurement using a hartmann sensor. *Optics express*, 15(16):10370–10375, 2007. 44

[95] Stefan Hild. Ligo-3 overview. *LIGO Document*, G1300577, 2013. 45

[96] Stefan Hild. Future interferometers. *LIGO Document*, G1000715, 2010. 45

[97] The Virgo Collaboration. Advanced Virgo Technical Design Report. *Virgo Internal Document*, VIR-0128A-12, 2012. https://tds.virgo-gw.eu/?content=3&r=9317. 46

[98] Stefan Hild. Design choices for the core optics of advanced detectors. *LIGO Document*, G0900444, 2009. 47

[99] Daniel Brown, Charlotte Bond, Mengyao Wang, Ludovico Carbone, and Andreas Freise. Modelling mirror surface distortion effects in low-loss, near-unstable fabry-perot cavities. *LIGO Document*, G1300687, 2013. 56

[100] Stefan Hild, Simon Chelkowski, and Andreas Freise. Pushing towards the et sensitivity using'conventional'technology. *arXiv preprint arXiv:0810.0604*, 2008. 58

[101] Christian Gräf, Stefan Hild, Harald Lück, et al. Optical layout for a 10 m Fabry-Perot Michelson interferometer with tunable stability. *Classical and quantum gravity*, 29(7):075003, 2012. 58, 62, 151

[102] J. A. Sidles and D. Sigg. Optical torques in suspended Fabry Perot interferometers. *Physics Letters A*, 354:167–172, May 2006. 59

[103] Lisa Barsotti and Matt Evans. Modeling of alignment sensing and control for enhanced ligo. Technical report, LIGO-T080186-01-I (Laser Interferometer Gravitational-Wave Observatory, 2008), 2008. 59

[104] Lisa Barsotti and Matt Evans. Modeling of alignment sensing and control for advanced ligo. *LIGO-T0900511*, 2009. 59

[105] S. Goßler, A. Bertolini, M. Born, et al. The AEI 10 m prototype interferometer. *Classical and Quantum Gravity*, 27(8):084023, April 2010. 61, 152

[106] T Westphal, G Bergmann, A Bertolini, et al. Design of the 10 m AEI prototype facility for interferometry studies. *Applied Physics B*, 106(3):551–557, 2012. 61

[107] K Dahl, T Alig, G Bergmann, et al. Status of the AEI 10 m prototype. *Classical and Quantum Gravity*, 29(14):145005, 2012. 61, 152

[108] Just another mode matching tool (JamMt). Accessed on 06/11/2017: http://www.sr.bham.ac.uk/dokuwiki/doku.php?id=geosim:jammt. 71

[109] R. W. P. Drever, J. L. Hall, F. V. Kowalski, et al. Laser phase and frequency stabilization using an optical resonator. *Applied Physics B: Lasers and Optics*, 31:97–105, June 1983. 73, 159

[110] E. D. Black. An introduction to Pound-Drever-Hall laser frequency stabilization. *American Journal of Physics*, 69:79–87, January 2001. 73, 159

[111] Thomas J. Kane and Robert L. Byer. Monolithic, unidirectional single-mode nd:yag ring laser. *Opt. Lett.*, 10(2):65, 1985. 75

[112] P Kwee and B Willke. Automatic laser beam characterization of monolithic nd:yag nonplanar ring lasers. *Appl. Opt.*, 47:6022–6032, 2008. 75, 76

[113] Altechna Company. Accessed on 31/07/2017: http://www.altechna.com/product_details.php?id=255. 78

[114] Newport Corporation. Accessed on 31/07/2017: https://www.newport.com/p/4004. 80

[115] Andreas Freise. *The Next Generation of Interferometry: Multi-Frequency Optical Modelling, Control Concepts and Implementation*. PhD thesis, Universität Hannover, 2003. 90, 92

[116] Yaron Hefetz and Nergis Mavalvala. Sensitivity of the ligo interferometer to mirror misalignment and method for automatic alignment. *MG7, Stanford Univ*, 1994. 113

[117] Dana Z. Anderson. Alignment of resonant optical cavities. *Appl. Opt.*, 23(17):2944–2949, Sep 1984. 113

[118] Euan Morrison, Brian J Meers, David I Robertson, and Henry Ward. Automatic alignment of optical interferometers. *Applied Optics*, 33(22):5041–5049, 1994. 113, 114

[119] Euan Morrison, Brian J Meers, David I Robertson, and Henry Ward. Experimental demonstration of an automatic alignment system for optical interferometers. *Applied optics*, 33(22):5037–5040, 1994. 113

[120] Christian Graef. Optical design aspects of the AEI 10m Prototype Interferometer. *LIGO Document*, G1100726, 2011. Available to LVC members: https://dcc.ligo.org/LIGO-G1100726. 152